Unclassified

Security Classification

DOCUMENT CONTROL DATA - R & D

(Security classification of title, body of abstract and indexing annotation must be entered when the overall report is classified)

1. ORIGINATING ACTIVITY (Corporate author)

University of Colorado
Boulder, Colorado

2a. REPORT SECURITY CLASSIFICATION

Unclassified

2b. GROUP

None

3. REPORT TITLE

The Monochromatic Sun in the Extreme Ultraviolet

4. DESCRIPTIVE NOTES (Type of report and inclusive dates)

Research Report

5. AUTHOR(S) (First name, middle initial, last name)

William J. Boardman

6. REPORT DATE	7a. TOTAL NO. OF PAGES	7b. NO. OF REFS
	194	90

8a. CONTRACT OR GRANT NO.	9a. ORIGINATOR'S REPORT NUMBER(S)
N00014-67-C-0290	Research Report
b. PROJECT NO	
c.	9b. OTHER REPORT NO(S) (Any other numbers that may be assigned this report)
d.	

10. DISTRIBUTION STATEMENT

Distribution of this document is unlimited

11. SUPPLEMENTARY NOTES	12. SPONSORING MILITARY ACTIVITY
None	Head, Geography Branch Earth Sciences Division, Office of Naval Research, Washington, D.C.

13. ABSTRACT

A set of spectroheliograms of the sun taken during an Aerobee rocket flight made on April 28, 1966, by the U.S. Naval Research Laboratory is the primary source of observational data. The wavelength range covered was approximately 170-600A. A coronal enhancement at the east limb was sufficiently intense, and free from contamination by other features and background continuum to permit a photometric study of its brightness profile in several of the more intense lines.

A study of the maximum brightnesses of the enhancement in several lines of widely varying temperatures gave a measure of the ability of the enhancement to emit radiation as a function of temperature. This ability was found to increase with increasing temperature between temperatures of 500,000 and 5,000,000 degrees, and to decrease rapidly at higher temperatures.

The brightness profiles of the enhancement in the various lines, under a geometrical assumption of cylindrical symmetry about an axis, yielded information on the temperature and density structure of the enhancement. A hot core in the enhancement of temperatures up to 5,000,000 degrees was found to exist, with a cooler envelope surrounding it. Electron densities of up to 2 billion per cubic centimeter were found to occur. The temperature and density structure was then compared to, and found to be consistent with, K-coronameter white-light and 9.1 centimeter radio observations of the same day.

Finally, a comparison of the measured emission scale heights with the scale heights predicted by hydrostatic equilibrium yielded information of the magnetic field structure governing the different temperature regimes. At one million degrees, the field appears to be nearly vertical, whereas hotter regions tend to be confined by a field of loop-type structure.

DD FORM 1473

Unclassified

Security Classification

14. KEY WORDS	LINK A		LINK B		LINK C	
	ROLE	WT	ROLE	WT	ROLE	WT
Solar Extreme Ultra-violet Solar XUV Spectroheliograms Coronal Active Region						

THE MONOCHROMATIC SUN IN THE EXTREME UNTRAVIOLET

William J. Boardman IV

A study carried out under the auspices of the
Office of Naval Research, Geography Branch,
under
Contract No. N00014-67-C-0290
Identification No. NR 046-740/12-7-66

TABLE OF CONTENTS

PART ONE -- OBSERVATIONAL ASPECTS AND METHODS OF DATA ACQUISITION

CHAPTER I

INTRODUCTION

The study of solar radiation with the idea of interpreting it in terms of structural models of the sun was almost completely restricted to the visible region of the electromagnetic spectrum until the end of the second world war. Since that time, two new branches of solar astronomy have developed, namely, radio astronomy, and ultraviolet and X-ray astronomy. The former enjoys the availability of an atmospheric window in the centimeter-meter wavelength range which fortunately corresponds to an "optical" depth range that covers a large portion of the solar atmosphere. Consequently, the science has matured to the point where regular, systematic observations are carried out at a number of observing stations throughout the world.

Two major limitations on radio coronal observations are the limited angular resolution of telescopes of manageable size, and the fact that the energies corresponding to radio wavelengths are so far removed from the excitation and ionization energies prevalent at coronal temperatures that little information on the chemical composition or the atomic processes that occur in the corona is obtainable. What we see at radio wavelengths is chiefly radiation from free-free electron-ion interactions. Although the amount of

such radiation produced by a sample of gas varies as the square of the average ionic charge, the shape of the free-free spectrum is independent of the structure of the ion.

Ultraviolet and X-ray astronomy, on the other hand, involves the study of radiation produced under conditions that approximate the optimum under which such radiations are produced. As a result, the ionization and excitation transitions which occur will produce observable radiation in this region of the spectrum which is characteristic of the chemical as well as the thermal structure of the gas. Also, in the ultraviolet and X-ray regions we are seeing the corona in the most intense part of its energy spectrum. This region of the spectrum plays a major role in determining as well as reflecting coronal structure.

Unfortunately, these shorter wavelengths are completely excluded from ground observations by the earth's atmospheric absorption. The only possibility for these observations, therefore, rests with rocket probes, satellites, and orbiting observatories. In each case, experiments must be pre-programmed and equipment designed for the specific observations planned, often with a considerable restriction on performance imposed by space and weight limitations and the complexities of a pointing control. Although the space probe experiments allow observations over an extended period of time, they share the common limitation of not enjoying the advantage of a variety of equipment plus an on-the-spot experimenter.

Line spectra of the sun in wavelengths short of the visible have been recorded both on special photographic emulsions deposited

by centrifuge techniques, and by photometric recording in flight with telemetered data transmission. The former method has been employed by the Rocket Spectroscopy Branch of the Naval Research Laboratory (NRL) beginning with a low resolution spectrum obtained with a V-2 rocket on October 10, 1946 (Baum et. al. 1946). Since then both normal and grazing incidence spectra of higher quality have been obtained at increasingly short wavelengths, with normal incidence being most valuable down to about 500A (Tousey 1964). A disadvantage of the use of photography in recording the solar extreme ultraviolet radiation is the fact that the film is also quite sensitive to radiation at longer wavelengths which make up by far the largest portion of the total solar radiation. The presence of instrumental light scatter produces a serious fogging of the emulsion unless measures are taken to eliminate this light before it enters the spectrograph. This has been accomplished by the NRL group with the use of a thin aluminum film which absorbs essentially all radiation longward of about 850A. A description of the transmission properties of such a filter is given in the next chapter.

The photoelectric recording techniques used by the Air Force Cambridge Research Laboratory (AFCRL) have the advantage of continuous monitoring during a flight but suffer from the loss of the fainter lines in the background noise. Also, the larger noise fluctuations may easily be misinterpreted as faint lines. The elimination of stray long-wavelength radiation becomes unnecessary with photomultiplier tubes, however, since their sensitivity to such radiation is much less than that of the photographic emulsions. A further

advantage of photoelectric recording techniques is that they yield reliable line intensities in absolute units much more readily than does photographic film.

Such observations as reported on by Hall, Damon and Hinteregger (1963), Hinteregger, Hall and Schweizer (1964), and Hall, Schweizer and Hinteregger (1965) have contributed significantly to our understanding of the absorption characteristics of the upper atmosphere, and reports by Neupert and associates (1964, 1965) of the grazing incidence spectra obtained by the first Orbiting Solar Observatory (OSO-1) furnished the first direct observational evidence of the variation of the extreme ultraviolet flux with solar activity. The OSO-1 observations indicated a more sensitive variation in flux with solar activity for the lines arising from the hotter ions; this was interpreted as indicating a greater degree of localization of hotter coronal material within active regions. Such an interpretation has since been confirmed by the recording of spectroheliograms (actually slitless solar spectra) by the NRL group (Purcell, Packer and Tousey 1959; Garrett, Purcell and Tousey 1964, Tousey, 1967a).

The spectroheliograms used in the present investigation represent a great improvement in quality of resolution over previous ones to the extent that the chromospheric network is easily visible in some of the cooler ions, notably He II Lyman-alpha. This improved resolution increases the possibility of identification of some fainter lines, and improves the ability to detect and evaluate differences in appearance of the active regions in lines emitted from ions of different temperatures.

CHAPTER II

DESCRIPTION OF THE EXPERIMENT

A. General Remarks

On April 28, 1966 a spectroheliograph was flown in an Aerobee 150 rocket with a biaxial pointing control developed by the University of Colorado. Time of launch was 23:34:51.08 UT, and the rocket achieved its maximum altitude of 187.7 km 232.2 seconds after launch. The general design of the spectroheliograph is similar to that flown during earlier flights (Tousey 1963) and consists of an aluminum filter mounted on a wire mesh to filter out wavelengths $\lesssim$ 830A, a concave platinum-coated grating operating at near-normal incidence, and photographic film produced by centrifuging a low-gelatin-content emulsion onto its support.

A series of pictures of the spectroheliograms taken during the flight is shown in Figure II-1. The spectroheliograms are also reproduced in two review articles, one by Tousey (1967a) and the other by Goldberg (1967). The quality is excellent, the angular resolution of the solar disk being approximately 10" of arc (Tousey 1967b, Goldberg 1967).

B. Aluminum Filter

A summary of the data available on the transmission of aluminum films is given by Tousey (1963) and is shown here in Figure II-2.

Although all three experimental results agree, insofar as they overlap, that there is a sharp peak at 171A followed by a steep dropoff to shorter wavelengths, and that the transmission decreases from 500A toward longer wavelengths, the quantitative agreement is very poor. The varying amount of aluminum oxide coating the surfaces of the different samples may explain why the transmission curve of Tomboulian and Bedo (1955) is about a factor of two higher than that of Astoin and Vodar (1953).

More difficult to explain is the markedly steeper slope at the long wavelength end of Walker, Rustgi, and Weissler's (1959) curve than that of Astoin and Vodar. Also present in the former but absent in the latter is a discontinuity in slope at around 630A. Experimental data obtained at the Naval Research Laboratory (Snider 1967) record a transmission of 11.2% at 584A and 32.8% at 304A. This indicates that the filter used in flight has a transmission curve somewhat steeper than that of Astoin and Vodar, but below that of Walker et. al.

The following criteria were used in the present analysis to construct a curve that would be consistent with the earlier experimental curves and pass through the two measured points of calibration of the transmission of the filter used in the flight. (1). The transmission curve should approach zero at 830 to 850A. Since a smooth curve fit of the two calibration points with this cutoff point is possible, and this curve shows a simple monotonic decrease with increasing wavelength as does that of Astoin and Vodar, the portion of the adopted curve longer than about 300A can be considered

as being known to within a few percent. (2). Shortwards of 300A, a reliable extrapolation from the calibration points would be impossible, so a compromise between Astoin and Vodar's and Tomboulian and Bedo's curves was adopted. This was done rather subjectively, but any departures of the adopted curve of a factor larger than about 1.5 from its assumed value would produce a curve differing significantly in shape from the experimental curves.

C. The Grating

The grating employed in the spectroheliograph was a Bausch and Lomb Catalog #35-62-27-80 platinum coated grating, with a concave radius of 998.8 mm, a ruling of 2400 lines mm^{-1}, and a blaze angle of $2^{o}05'$. The result of the blaze is a maximum intensity of the first order image at around 300A at near-normal incidence, apart from the variability of reflectivity of the platinum surface with wavelength. The half-intensity points of the grating's diffraction efficiency curve lie at approximately one-half and twice the wavelength of maximum intensity, i.e., at about 150A and 600A (Purcell 1967).

In addition to the variation of efficiency with wavelength that results from diffraction alone, we must consider variations in the reflectivity of the platinum coating with wavelength. The solid curve in Figure II-3 shows the reflectivity of a smooth, platinum-coated parabolic mirror obtained experimentally at NRL by Purcell (1967).

The efficiency of the grating used in the spectroheliograph was measured at 304A and 584A at NRL and found to have values in

the first order of 1.1% and 5.6% at these two wavelengths, respectively. At 304A, the reflectivity of the grating is 0.5 that of the smooth mirror, and at 584A the ratio is down to nearly one-fourth, in agreement with what is expected from the ruling of the grating. At the short wavelength end of the calibration, the extrapolated value of the reflectivity at 150A based on Purcell's data should also differ from the grating's efficiency by a factor of about four. We thus have three well-separated points at 150A, 304A, and 584A for which the grating's reflectivity is fairly well known, and through which we can draw a reflectivity curve for the grating that is consistent with Purcell's curve for the mirror. The dashed curve in Figure II-3 shows the adopted values of the grating's efficiency.

D. The Film

The main problem in the design of films for work in the far ultraviolet is one of overcoming the high absorption of the gelatin in these wavelengths. Kodak-Pathe of Paris, by a centrifuging technique, has produced emulsions consisting of a single layer of grains on the outside of the supporting medium (Tousey 1963), thus eliminating this absorption. Successive modifications of this type of emulsion have been manufactured under the designations SC-4, SC-5, and SC-7. A modification of the last of these, SC-7t., which possesses a thinner emulsion was employed in the rocket spectroheliograph.

No absolute intensity standards were available for the film emulsion used. I therefore sought to produce a calibration curve

in terms of arbitrary units of film exposure, by an analysis of four spectroheliograms with exposure times ranging from 0.6 to 10.7 seconds. At four arbitrary points along the continuum, at the He II 304A disk image, and at a limb feature in Fe XVI at 335A and 361A, and Mg IX at 368A, I compared the film densities of the four different exposures. The film density, D, is defined in the usual manner:

$$D = \log_{10} \frac{I_o}{I} \qquad (1)$$

where I_o and I are the intensities of a standard beam having passed through clear film and film of density D, respectively. When plotted against log E, with E the exposure (intensity x time), the characteristic curve of the film results, whose shape is independent of the units measuring the exposure, E. Eight plots of the characteristic curve at the eight different wavelengths resulted, all with nearly the same shape. A well-defined composite curve resulted when the separate curves were shifted horizontally (along the exposure axis) to minimize scatter. Figure II-4 shows this composite curve with the points obtained by measurement from the film. Included are some points produced in the laboratory whose significance will now be discussed.

The method of calibration given above gives good values of the slope of the characteristic curve of the film (often called the "gamma" of the film) when the variations in exposure are produced by changes in exposure time. If the same variations in exposure are produced by changes in the intensity, rather than time,

a different set of curves may result. This effect is the failure of the reciprocity law of film emulsions, and can occur when one compares exposures of widely differing lengths. Since we must consider the relative brightnesses of the various points of th spectroheliograms as unknown at this point, a reciprocity check necessitates a comparison of a graded series of exposures whose variations in film density are produced by variations in beam intensity with a constant exposure time. Such a series of exposures at 5 and 30 seconds at 304A were recorded at NRL by Snider (1967) through filters of various transmissivities. Table II-1 shows the exposures, defined in the usual manner but in arbitrary units, and the corresponding film densities. It is evident that reciprocity failure becomes considerable between exposure times differing by a factor of six. Both exposure times taken separately, however, produce a characteristic curve similar to the ones obtained from the graded exposure time sequences with a gamma of about 0.5, and are included in the construction of the curve in Figure II-4.

All photometric work in this investigation uses two spectroheliograms of exposure times 10.7 seconds and 28.9 seconds corresponding to wavelength regions of 171 - 400A and 400 - 630A respectively. Unfortunately, there is no useful overlopping of the two wavelength regions to provide a direct measurement of reciprocity failure from the plates used in the analysis. The reciprocity failure of the film will, however, be less marked between these exposures, which differ by a factor of 2.7 as compared with a factor of six in the laboratory exposures.

Consider a film emulsion in which the reciprocity law is obeyed, that is, the blackening of the film depends only on the total amount of energy received by the film per unit area. If E is the degree of exposure of the film; I, the intensity of the beam; and t, the duration of the exposure, then

$$E = It \tag{2}$$

If the reciprocity law does not hold, we may define an effective exposure, E', of the film that relates to the film density by

$$\gamma \log E' + \text{constant} = D \tag{3}$$

and assume, after Schwartzschild (1900) that the effective exposure obeys the following relation:

$$E' = It^p \tag{4}$$

where p is an unknown constant. From (3) and (4) we may eliminate E', and consider the case where I is the same, but t varies. This results in the expression

$$p(\log t_2 - \log t_1) = \frac{D_2 - D_1}{\gamma} \tag{5}$$

where γ is the "gamma" of the film. For the film used in the laboratory calibrations, $\gamma = 0.5$, and $\log t_2 - \log t_1 = .778$. Therefore, a value of p is specified for each pair of exposures given in Table II-1 by the following formula:

$$p = 2.57(D_2 - D_1) \qquad (6)$$

The values of p so obtained are tabulated in the far right column of Table II-1. If we adopt a value of p = 0.30. then the reciprocity failure of the film will lead to an error in the relative exposures of the two spectroheliograms of a factor of $2.7^{-0.7}$ or 0.5. This is a small enough error that it may be included in the empirical correction procedure described in the next section.

E. Overall Instrumental Efficiency

So far, no allowance has been made for any possible variation in the sensitivity of the film with wavelength. Since the intensities of the 304A and 584A lines produced in the laboratory were not available on an absolute scale, an indirect method of checking the instrumental efficiency to detect a possible variation in wavelength response of the film had to be used. Since the emission from the lines of the lower-temperature ions comes more or less uniformly from the entire disk, it is possible to compare the relative surface brightnesses of these lines as recorded on the film with the line energy fluxes outside the earth's atmosphere measured by Hall, Damon, and Hinteregger (1963). Table II-2 shows a comparison of the surface brightness of the solar disk in the lines He I 584A, O IV 554A, and [illegible] II 304A with the corresponding fluxes measured by the AFCRL group. I obtained the relative surface brightnesses by photometry from the spectroheliograms, using the efficiency curves of the aluminum filter and platinum grating to convert film densities to intensities. The absolute values of the brightnesses followed

from the assumption that the 304A He II line, whose photometry was the most reliable, had a flux to surface brightness ratio equal to $(R_\odot/1A.U.)^2$, or 2.15×10^{-5}, the flux being based on the AFCRL observations. The data show unmistakably a strong increase in sensitivity of the spectroheliograph with decreasing wavelength that is probably due to a combination of (a) wavelength variation in film sensitivity, (b) reciprocity failure between the exposures of different lengths and possibly variations in the degree of reciprocity failure with wavelength, and (c) variations with wavelength of the fraction of solar radiation absorbed by the terrestrial atmosphere above the apparatus. The total variation appears to be nearly linear and can be represented approximately by the expression

$$X = 1.90 - 0.03\lambda(A) \qquad (7)$$

We then adopt for the total efficiency curve of the apparatus

$$Eff = TRX \qquad (8)$$

where Eff is the total efficiency, T is the transmission of the aluminum filter, and R is the reflectivity of the grating. Since eq. (8) is unknown to within a multiplicative constant, the efficiency units are arbitrary. The absolute brightnesses of the coronal features, which will be needed later, will be found by another comparison of the measured intensities of the solar disk by Widdop et. al. with the photographic density on the spectroheliogram, this time from the corrected efficiency function given by (8).

A plot of the efficiency variation with wavelength as given by eq. (8) is shown in Figure II-5.

Table II-1

He II 304A Laboratory Film Calibrations

E_1	D_1	E_2	D_2	P
5	.13	30	.30	.44
10	.23	60	.32	.23
25	.34	150	.48	.36
50	.65	300	.74	.22
100	.78	600	.90	.31
250	1.02	1500	1.16	.36
500	1.24	3000	1.28	

5 second exposures 30 second exposures

Table II-2

Emission from the Sun in Some Low-Temperature Ions

Line	E(erg cm^{-2} sec^{-1}) from entire disk at 1 AU	E/E_{554}	I(erg $cm^{-2}sec^{-1}$) from spectroheliograms	I/I_{554}
He I 584A	.055	5.5	2.94×10^{2}	2.2
O IV 554A	.01	1.0	1.34×10^{2}	1.0
HeII 304A	.25	25	1.16×10^{4}	86

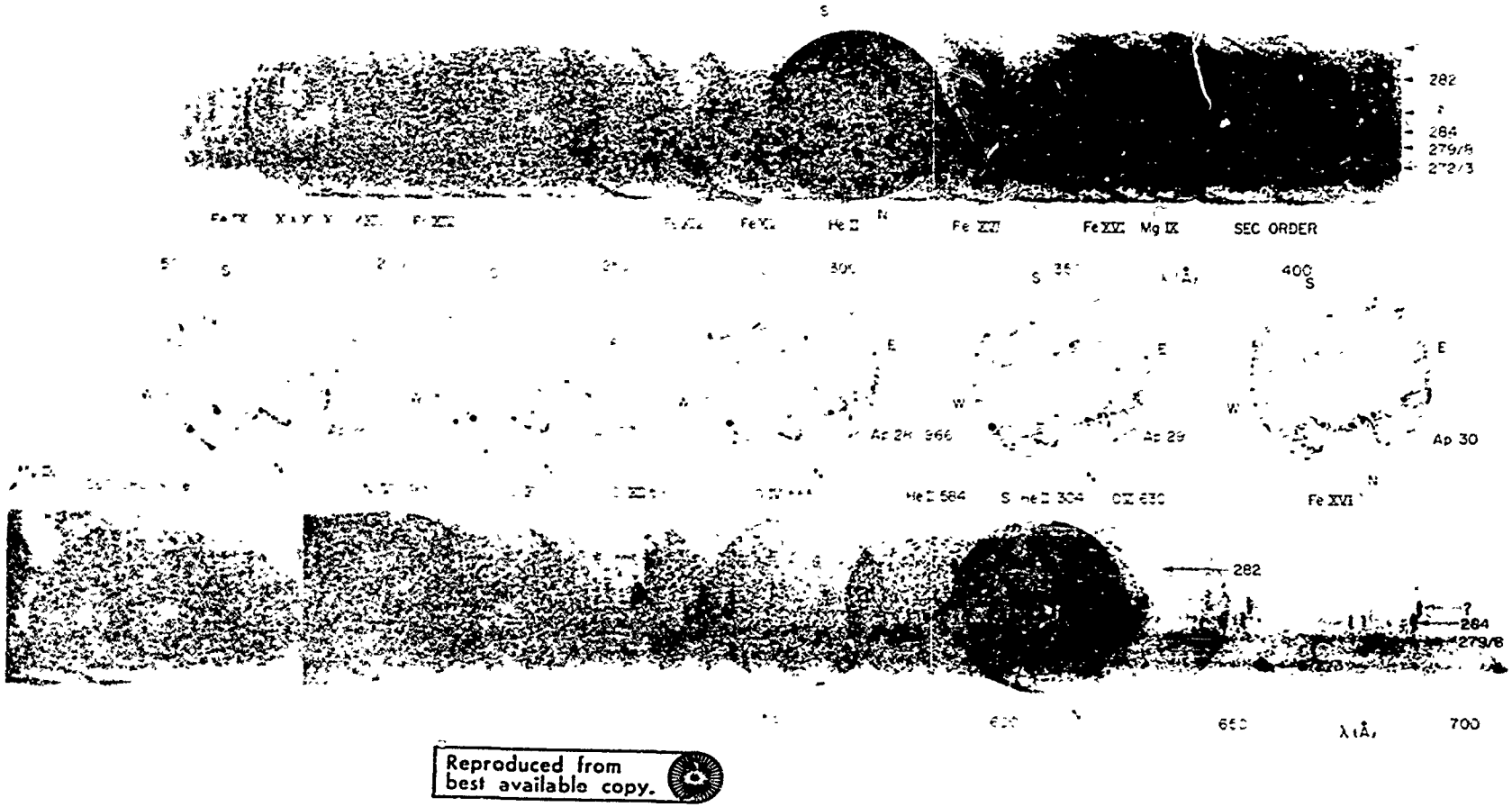

Figure II-1. The spectroheliograms recorded during the NRL flight of an Aerobee rocket on April 28, 1966. U. S. Naval Research Laboratory Photograph.

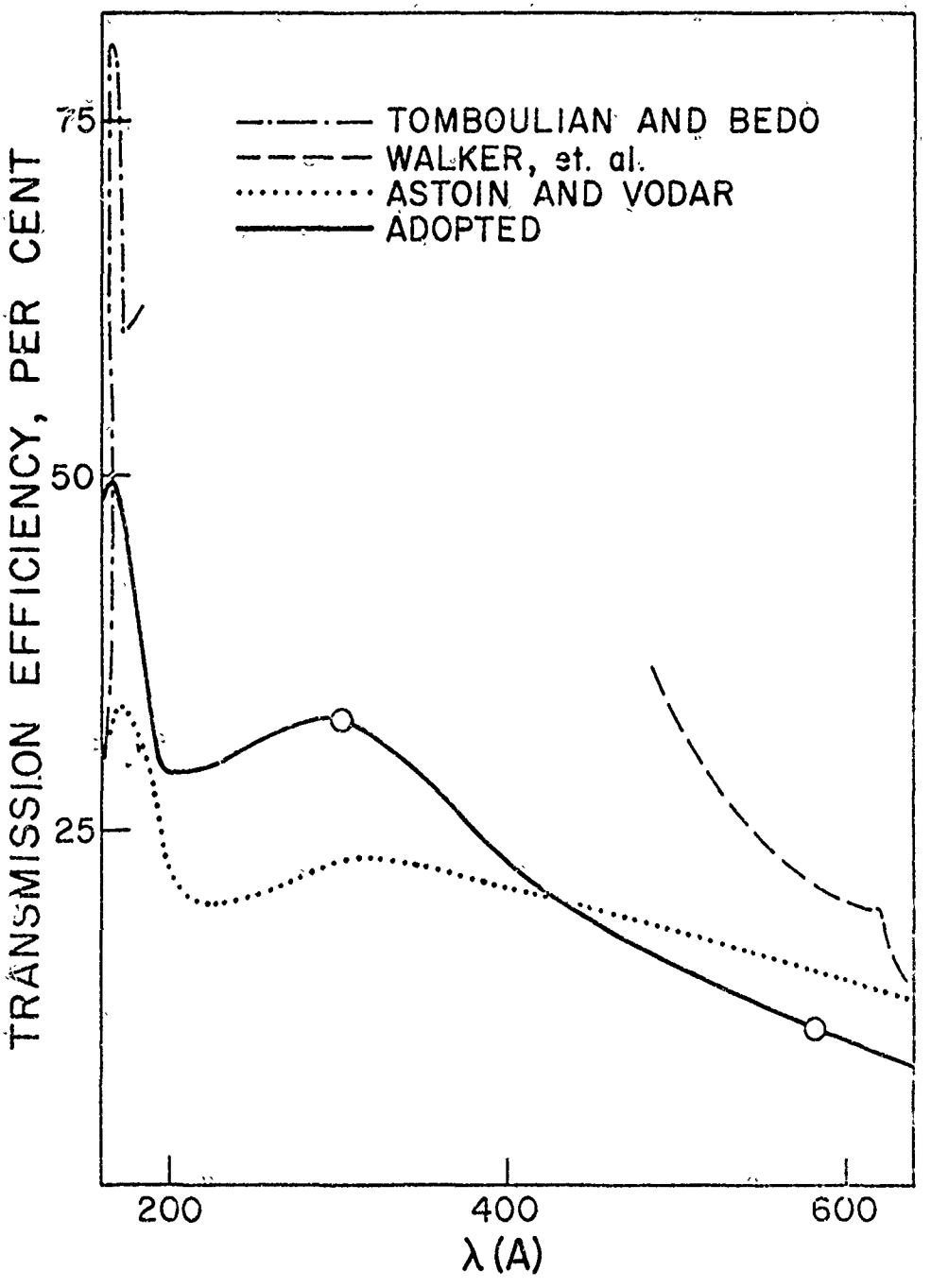

Figure II-2. The percentages of radiation transmitted by aluminum filters of thicknesses 1150A for the case of Walker, Rustgi, and Weissler; 1000A for the others. The two points obtained at 304A and 584A from laboratory measurements of the filter used in flight are circled. After Tousey (1963), except for the adopted curve.

Figure II-3. The reflectivity of an off-axis parabolic mirror with a platinum coating (Purcell 1967). The lower curve represents the adopted efficiency curve for the grating, and shows two points obtained from laboratory measurements.

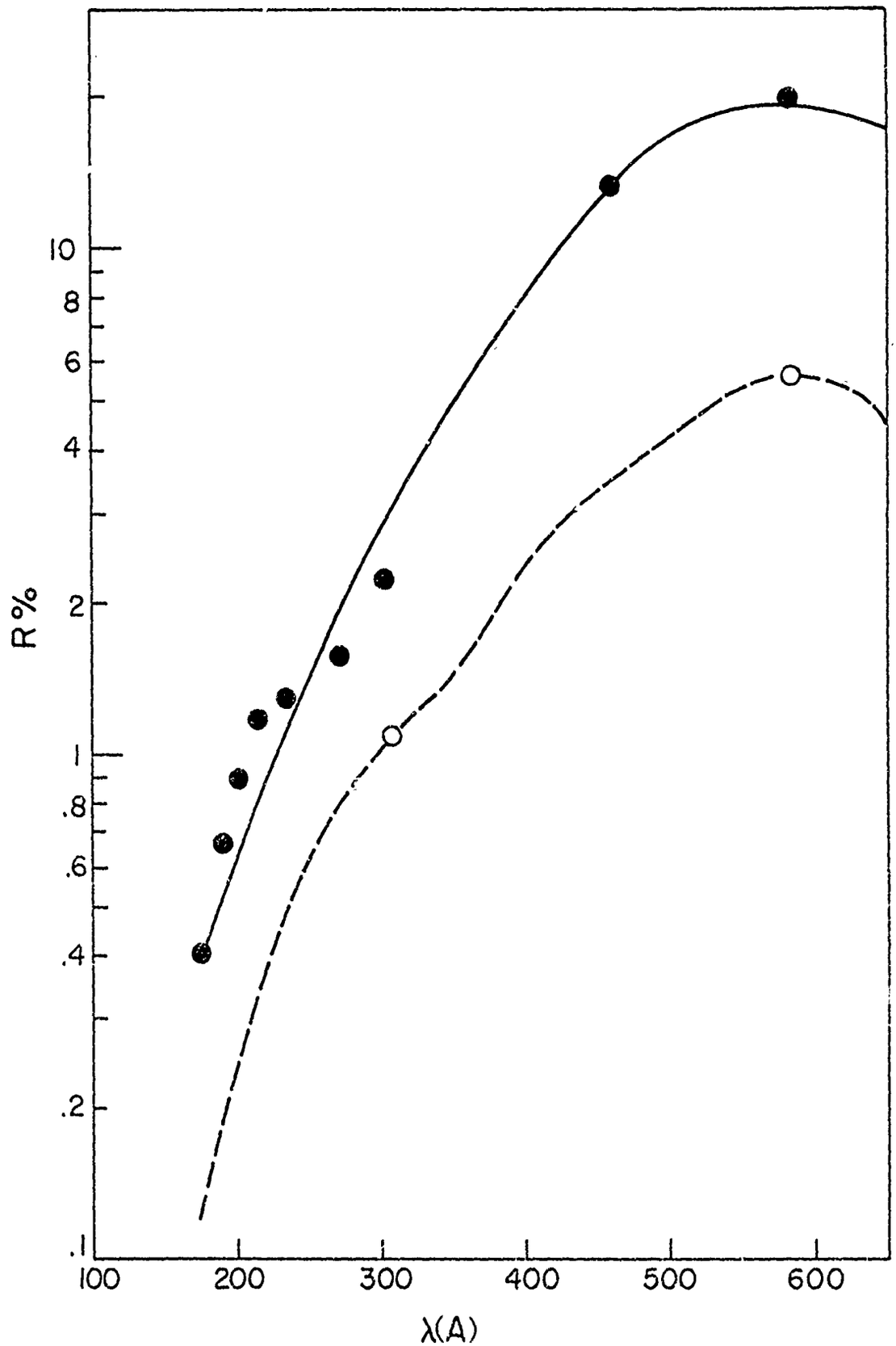

Figure II-3

Figure II-4. The characteristic curve of the Shumann-type emuslion used in flight. The quantity E represents the exposure, intensity times time, in arbitrary units.

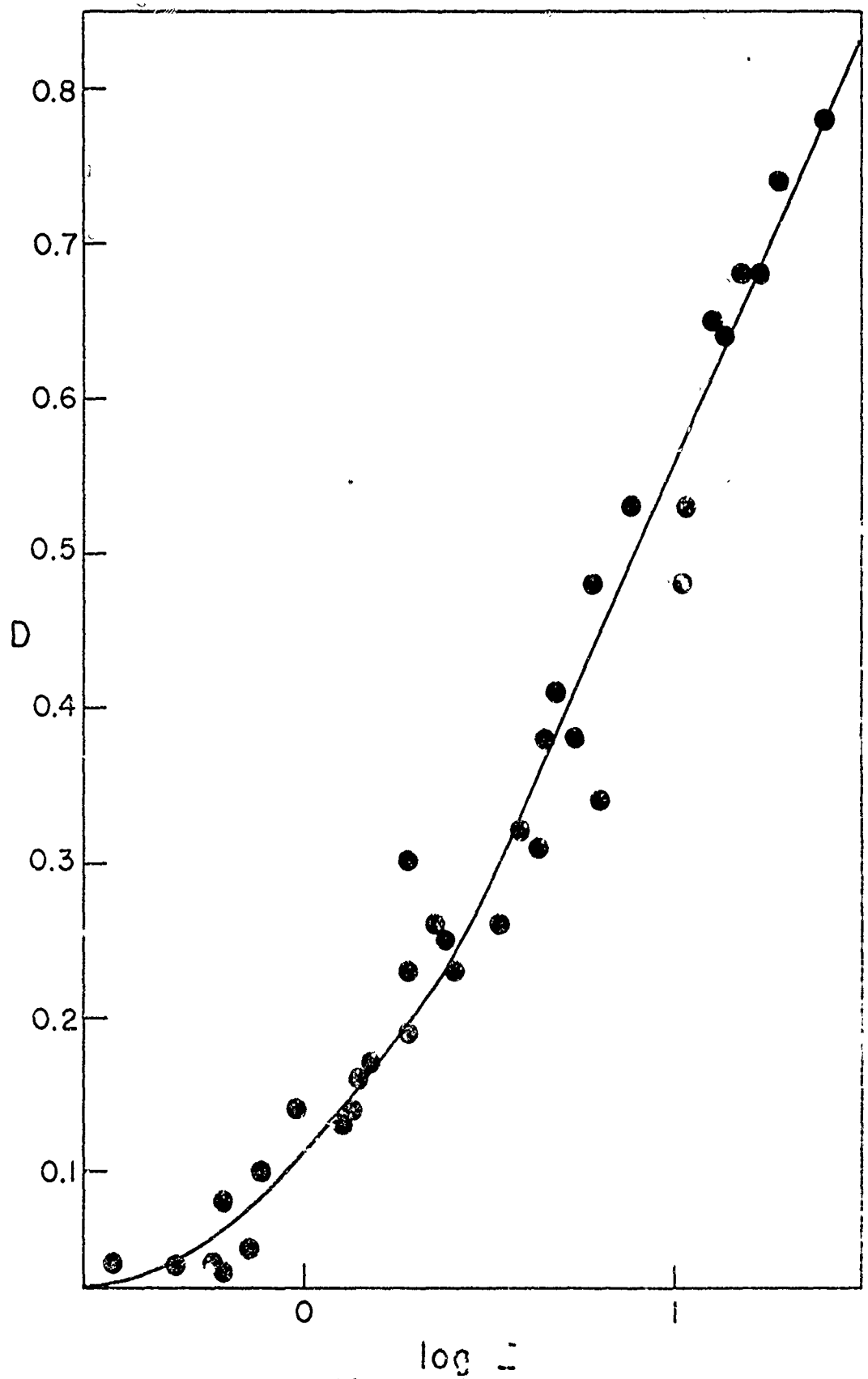

Figure II-4

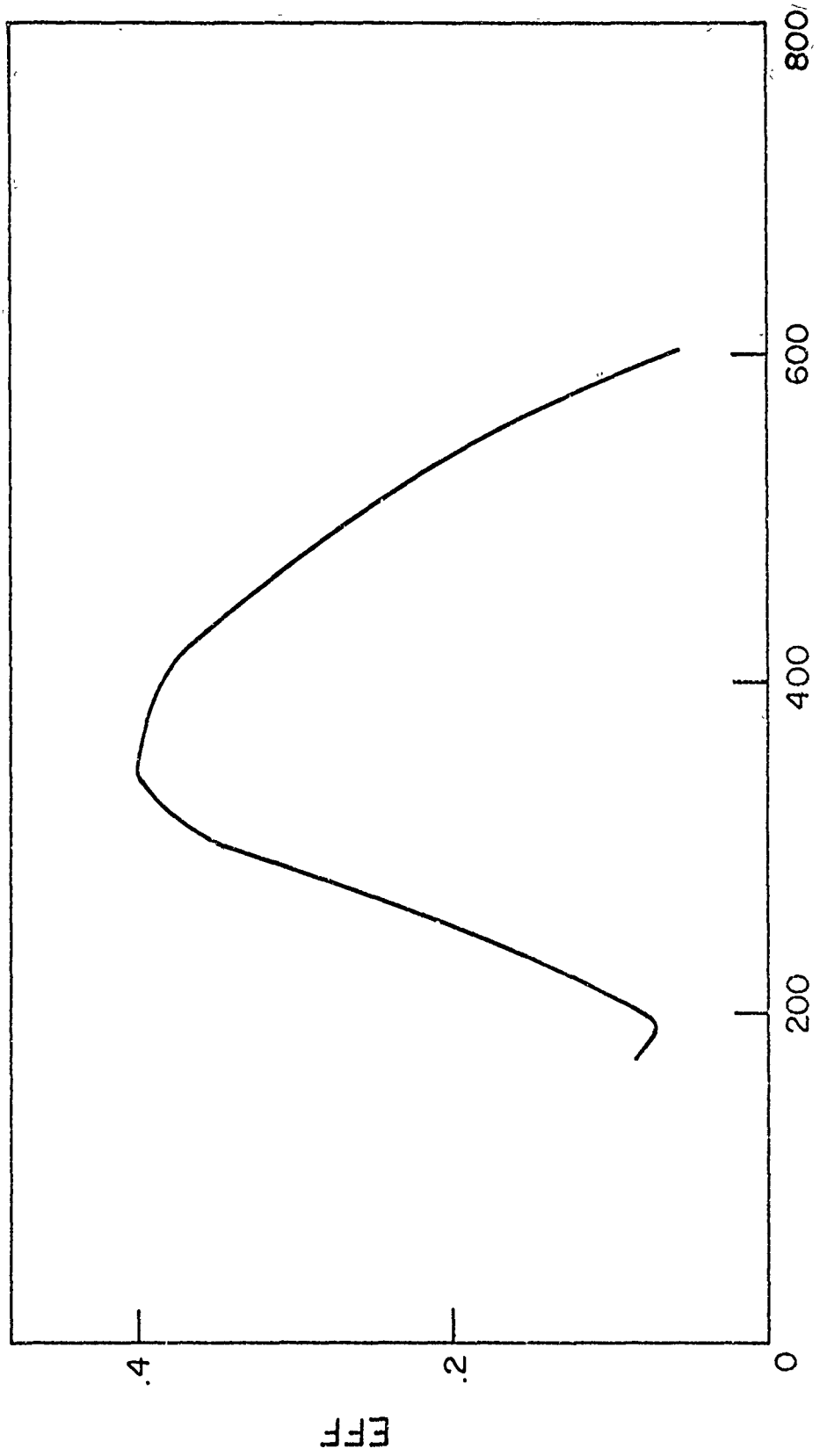

Figure II-5. The overall efficiency of the spectrometer, in arbitrary units.

CHAPTER III

APPEARANCE OF THE SUN ON APRIL 28, 1966

A. The Visible Disk

The solar disk on April 28, 1966 exhibited a considerable amount of activity in the northern hemisphere as indicated by the Fraunhofer Institut map for that date (Figure II-1). The active regions shown on the map that give rise to noticeable enhancement of the EUV radiation are:

(1) A large region near the west limb of the sun with a spot group of class D7 (Zurich classification). The region is centered at 19°N, 58°W.

(2) An extended region encompassing two small spots of class A1, centered at 29°N, 22°E; and 30°N, 34°E.

(3) A moderate-sized region surrounding a class J1 sunspot. Position: 22°N, 67°E.

(4) A coronal enhancement at the east limb which appears to be associated with an active region that lies just behind the limb. The first suggestion of its appearance in Ca-K is a very slight brightening of the limb on April 29 at 13:25 UT, or 13^h50^m after the spectroheliograms were recorded. The feature is centered around 17°N, and on April 28 appeared only in coronal emission. Observations of the progress of the plage across the disk indicate that the extreme western portion of the plage lay from 0° to 3° behind the

limb during the rocket flight. On the EUV spectroheliograms, the feature appears at the extreme right hand position of the limb, or about 70° from the north pole.

(5) An isolated small center at 25°S, 18°E, in which an Al spot develops on April 29, 1966.

Figures III-1 and III-2 show the solar disk for April 28 in the light of H-alpha and Ca-K, respectively. In both monochromatic images, Feature 1 appears as a fairly compact, intense plage. To the east of this region lies a region of moderate activity, which is centered about 25°N, 22°W, and appears to contribute little to the EUV radiation. This region shows a plage structure of much greater complexity, and has associated with it a filament that extends from it to the northeast.

Feature 2 appears highly structured in both H-alpha and Ca-K, and also in the cooler ions radiating in the EUV. A comparison of the Ca-K picture of this region (Figure III-2) with the disk image of O V at 630A shows a quite striking agreement in structure, with two large plages toward the east, preceded by several smaller ones toward the west. An example of this feature in a hotter ion is most clearly seen in the second-order emission of Fe XVI 335A, which appears at 670A against an essentially zero background. At these temperatures of 4 to 5 x 10^6 °K, the coronal enhancement appears as two larger, fairly well-defined regions of much less complex structure.

A quite well-defined plage region appears on the disk at the same position as Feature 3, and the association of Feature 4 with a

plage region just behind the limb has already been pointed out. The latter feature shows no evidence of its presence in the cooler EUV lines such as O V at 630A, and begins to appear only faintly in Ne VII at 465A, at a temperature of 5 x 10^5 °K. As seen on April 28, then, we may consider Feature 4 as being purely coronal.

B. Limb Observations

A particularly useful comparison of the EUV radiation from the solar corona would be with limb spectra from a coronagraph-spectrograph in such forbidden lines as Fe X 6374A and Fe XIV 5303A. Unfortunately, the only limb spectra available near the time of the rocket flight were taken on April 27 at Sacramento Peak Observatory, the day before the flight occurred. The details of the limb enhancement in the visible lines are thus not directly comparable with the EUV observations except in a qualitative sense. However, certain characteristics of the structure of the visible line radiation are quite interesting and have their evident counterparts in the EUV spectroheliograms taken on the next day.

Figures III-3 and III-4 show, respectively, the Sacramento Peak limb spectra for April 27 taken at high resolution, in the regions of 6374A and 5303A, respectively. The spectra are centered at 65° position angle on the solar disk as measured clockwise from the north point of the solar limb. The P-correction for the dates April 27 and 28, 1966 was nearly -25°, thus the spectra are centered about a point on the east limb at 20°N latitude. A point by point comparison of the intensity profiles of these spectra shows a rather

broad maximum at nearly 20°N, with two maxima of lesser width on either side. This enhancement corresponds closely to the position and extent of Feature 3 on the same date, and we may safely identify the forbidden-line enhancement with the active region and forbidden line enhancement listed as Feature 3. In addition, there appears a bright knot of emission at 5303A poleward from the other feature. This emission does not appear in the red line. The overall impression gained from the two spectra is that the green line, which is representative of hotter material than the red line, exhibits the same general variation in brightness along the limb in an active region, but possesses one additional important characteristic; namely, the addition of very bright, concentrated maxima presumably representing hot, dense "knots" of coronal material.

The quiet corona adjacent to the active region shows a general increase in red-line emission towards the equator, and an increase of the green-line emission poleward. The former phenomenon is similar to the behavior of the solar limb as seen in Mg IX at 368A on the EUV spectroheliograms. The latter effect appears to be due to the presence of other coronal activity to the north of the main feature. Because the axis of solar rotation is inclined to the plane of the sky with the north pole inclined away from the observer by an angle of B = 4°, the belt of activity appears to be displaced to the north as one moves in slightly from the limb.

The primary feature in both the red and green lines appears to extend along an arc of about 5° at the solar limb, and is extended to either side by enhancements about 3° in width. The total

north-to-south distance of Feature 3 as it appears in the EUV lines is also about 11°, although filmgrain noise makes the boundary of the EUV enhancement less well defined than it is in the visible lines. A localized brightening does appear in Feature 3 south of the brightest portion of the enhancement in some of the brighter lines, notably 335A and 361A of Fe XVI. The fact that there is a difference of one day between the two observations makes detailed comparisons uncertain, both because of solar rotation and possible time changes in the physical structure of the enhancement. A look at the Ca-K picture clearly shows the part of the plage closest to the limb to be made up of a three-fold structure. The central maximum, which is the brightest portion of the region, connects with another maximum to the south by a bright channel, whereas the northern appendage is separated by a dark region.

We conclude, then, that there is a one-to-one correspondence between the elements of Feature 3 as seen in Ca-K, and in the coronal visible and EUV radiation, at least among elements of the order of size of a few degrees on the solar disk. The coronal emission, however, shows little structure on a smaller scale than this, although the presence of lines of widely differing temperatures in the same region of the corona suggests unresolved coronal structure on an even smaller scale. There thus appears to be a continuity in the gross structure of an enhancement with the underlying plage that is preserved across the transition region, but structures as small as the chromospheric network are completely smeared out by the time they reach the corona.

C. The EUV Spectroheliograms

1. Line Predictions and Observations

Tables III-1 to III-9 list all the predicted lines arising from the screening transitions $2s^2 2p^n \rightarrow 2s2p^{n+1}$ of the Be I to F I isoelectronic sequences, and the 2s → 2p transitions of the Li I sequence for the elements O, Ne, Mg, Si, and S. In addition, the resonance lines of Al XI, X; P XIII, XII; and Na VIII are included because of the intensity of the resonance lines from the Li I and Be I sequence. Also included are the lines arising from the Fe ions, and a few of the stronger nickel lines. All the lines listed may be excited directly from the ground term or from some metastable level. Recent computations by Bely (1966a, 1966b) of the collisional cross sections of the lithium type ions indicate that, in these ions at least, the quadrupole excitation cross sections in some cases are larger than the permitted dipole cross sections. Therefore a metastable level might be easily excited and could suffer a second collision to the upper level of an enhanced line. We thus see lines of different multiplicity in the same ions, although the non-resonance lines are decidedly weaker. For the very high temperature ions, departures from L-S coupling destroy metastability and the enhanced lines must be excited directly from the ground state. We therefore observe enhanced lines only in a few ions whose temperature is rather low ($\lesssim 10^6$ °K).

The quantities f_{eff} represent the effective oscillator strengths rather than the actual f-values of the lines in question. The method of calculating them from the actual f-values is described

in Chapter V. For the sake of consistency within an isoelectronic sequence, the oscillator strengths were taken for the most part from Varsavsky (1961) for resonance transitions, although more recent values as compiled by Pottasch (1967) will be used later in the data reductions. The f-values not directly given by Varsavsky were obtained from the relative line strengths in L-S coupling (Allen 1963). Departures from L-S coupling become increasingly important for the ions of greater charge; however a check is possible in the case of Fe XIII with intermediate coupling line strengths calculated by House (1967). The L-S coupling approximation for Fe XIII gives f-values in agreement with House's results to within a few percent.

Since uncertainties of several tenths of an Angstrom in the measured wavelengths of the emission features in the spectroheliograms exist, a somewhat roundabout method of identifying some of the weaker lines had to be used. When possible, a comparison was made with slit spectra taken by NRL during other flights to determine the wavelengths of the emission features more accurately than would be possible by direct measurement. As might be expected, nearly all lines observable on the spectroheliograms were also visible on the slit spectra. The tables at the end of the chapter then confirmed most of the earlier identifications. In the longer wavelength regions ($\gtrsim$ 400A) only the very strongest lines were visible in the slit spectra, and several low excitation lines were recorded for the first time on the spectroheliograms as plage-type features. A good example is a group of lines of Mg VI and Ne VI at around 400A.

The following subsections give a description of the identified lines and include several lines in the discussion whose appearance on the spectroheliograms is uncertain. In particular, lines between 264 and 304A which overlap the He II Lyman-alpha image at the east limb may be quite strong yet invisible in the sharp features used for identification due to the overpowering strength of the He II disk image.

2. Lithium Sequence

The properties of the lithium-type ion emission have been discussed briefly by C. Pecker (1963) and by Tousey (1963, 1964). In spite of comparatively small oscillator strengths ($\lesssim 0.1$) the resonance doublet $2p\ ^2P_{3/2,\ 1/2} - 2s\ ^2S_{1/2}$ is easily seen in the more abundant elements. Two effects combine to increase the strength of the lines. First, the comparatively small value of W/kT results in a large value of the Gaunt factor P(W/kT), and this increases the collisional excitation rate. Also, as we shall see later, the relative abundances of these ions decreases rather slowly with increasing temperature.

The sequence first appears with the lines 609.8A and 625.3A of Mg X. These lines appear rather weak because of the overlapping with emission from the O V 629.7A disk, and the low transmission of the aluminum filter at these wavelengths. Although most of the solar image at 609.8A overlaps the second order He II Lyman-alpha image, the east limb of the Mg X line projects enough beyond the helium disk to make features (3) and (4) visible.

The two corresponding lines of Al XI at 550.0A and 568.5A are not evident due to the low abundance of aluminum on the sun, and the fact that they are superimposed upon images of O IV at 554A and He I at 584A.

Both lines of Si XII at 499.3A and 521.1A are prominent. The lines of P XIII at 456.1 and 481.4A are absent, although there is a very weak line at about 483A that remains unidentified. It is tempting to assign this line to P XIII; the other line is however definitely not present. The 483A line is more likely the second order image of an unidentified but strong line at 241.7A.

A similar situation exists for S XIV which according to photospheric abundance determinations by Goldberg, Müller, and Aller (1960) should emit almost as strongly as Si XII. A strong line is present at 422A which could correspond to Ivanov-Kholodnyi and Nikolskii's (1962) extrapolation of the S XIV K-line as being at 421A. The other line at around 446A is not in evidence, however, and the line at 422A is more likely the second order of a line of Fe XIV at 211A.

3. Beryllium Sequence

The resonance singlets of the Beryllium sequence ($2s^2\ ^1S_0 \rightarrow 2s2p\ ^1P_1$) are possibly in evidence continuously from O V at 629.7A to Si XI at 303.4A with the exception of F VI and Na VIII, although Al X is very weak. The 629.7A line of O V is very strong with most of the emission coming from the disk, and the active regions showing considerable plage-type structure. Ne VII at 465.3A is also strong but shows less disk emission and some evidence of extended coronal

emission. Feature 3 is evident as a sharp plage at the base of extended, diffuse coronal emission. Mg IX appears strongly at 368.1A and continues the trend toward more diffuse radiation associated with the corona, less emission from the disk, and less noticeable plage-type structure. Limb brightening is still very strong. A line at 330A was observed by Tousey and was suggested by him to be Al X 332.9A; this line is also present weakly in Features 3 and 4. Si XI at 303.6A falls almost completely upon the He II 303.8A image, but the active coronal emissions are evident due to the strength of the line. Pottasch (1964) identifies a line at 278.7A from Hinteregger's (1964) data as arising from P XII, but the weakness of the line and the presence of the He II 304A disk superimposed on the east limb prevent its appearance on the spectroheliograms. The line of S XIII at 257.3A is present but badly blended with other lines of silicon and sulfur.

The triplet spectra of the beryllium-type ions are seen with reasonable certainty only in the case of Mg IX. Zirin (1964) identifies a line at 444A as arising from the Mg IX triplet, and the spectroheliograms show weakly other lines at about 449A and 440A. The corresponding lines of Si XI lie between 365A and 372A and are not apparent. Part of the reason for their absence may be the wealth of faint lines in this region from Mg VII, and the strong, diffuse line of Mg IX at 368.1A.

4. Boron Sequence

The lines of the boron sequence are in general considerably weaker than those of the lithium and beryllium sequences, largely

because the large number of transitions possible makes the oscillator strength of each rather small. The comparatively small term splitting in this series gives rise to rather close blends of lines which are difficult to separate in images of extended features.

In O IV the term splitting is very small. The $^2P \rightarrow {}^2P$ transitions produce a blend at around 554A which is quite strong due to the high abundance of oxygen. Considerable emission arises from the quiet regions of the solar disk, but limb brightening is also pronounced in contrast to the helium images. The lines of the multiplet $^2P \rightarrow {}^2S$ may be present at 608.4A and 609.8A but are blended considerably with second order helium Lyman-alpha and Mg X 609.8A.

The spectrum of Ne VI is very faint, and the resonance $^2P \rightarrow {}^2D$ lines at 449A and 562A are unobservable in the spectroheliograms, partially because of overlap with the Ne I 584A disk image. The two lines expected from the $^2P \rightarrow {}^2S$ transitions at 430A and 432A are not evident with certainty either, but are obscured by resonance lines of Mg VII. One line present at about 402A in feature 3 as a small, plage-type feature corresponds to the strongest line of the $^2P \rightarrow {}^2P$ multiplet at 401.9A ($^2P_{3/2} \rightarrow {}^2P_{3/2}$). The other lines are considerably weaker in L-S coupling and are masked by the resonance lines of Mg VI which are almost identical in appearance. A very weak line on the red side of Ne VI 399.8A probably arises from $^2P_{1/2} \rightarrow {}^2P_{3/2}$ of Ne VI at 399.8A. Of the remaining lines, the 3/2 → 1/2 transition at 401.9A blends almost

exactly with a Mg VI line of the same wavelength, and the 1/2 → 1/2 transition at 401.1A blends with Mg VI 400.7A.

The spectrum of Mg VIII is present with a good many lines including the resonance doublet at 430.5A and 436.7A. Lines of the $^2P - {}^2P$ multiplet are present at 311.8A, 313.7A, 315.0A and 317.0A, but these are obscured somewhat by the lines of the $2s^2 2p^3\ {}^4S \rightarrow 2s2p^4\ {}^4P$ transitions of Si VIII. The $^2P \rightarrow {}^2S$ multiplet is not visible.

Tousey, et. al. (1965) identify a line at 356.0A as arising from the quartet terms $2s2p^2\ {}^4P_{5/2} \rightarrow 2p^3\ {}^4S_{3/2}$. This line appears very faintly on the spectroheliograms as a plage in Feature (3). The other lines of the multiplet at 352.4A and 353.8A are also present. The line at 356.0A is, however, almost exactly coincident with a close resonance pair of Si X $^2P_{3/2} \rightarrow {}^2D_{3/2,\ 5/2}$ at 356.1A. Since the other line at 347.4A is also present, the 356A line must be considered a blend.

Other lines of the Si X doublet transitions at 272A and 277A have been observed by Tousey et. al. (1965) and identified as the $^2P - {}^2S$ transitions, but they are completely masked at the west limb by the He II Lyman-alpha line. Near the west limb a coronal enhancement is seen in the proper position of Feature (1) in this wavelength region, but the feature is too extended for a wavelength measurement.

Several lines appear on the spectroheliograms in the region 254A - 261A which may be attributed partly to the $^2P - {}^2P$ transition

of Si X. These lines are blended with several lines of the S X resonance quartet and are difficult to identify individually.

The quartet lines of Si X lie around 290A and the same difficulty in observing them as in observing the $^2P \rightarrow {}^2S$ lines applies. There is an enhancement corresponding to Feature 1 at this wavelength, but other contributors could be the $2s^22p^2\ {}^3P \rightarrow 2s2p^3\ {}^3P$ transitions of Si IX (a resonance multiplet) and the $3s\ {}^2S_{1/2} \rightarrow 3p\ {}^2P_{3/2}$ 293.3A transition of Ni XVIII. Also contributing to the emission at 290A of Feature 1 could be the resonance multiplet $^2P \rightarrow {}^2D$ of S XII.

No lines of S XII have been observed with any certainty, although many predicted lines either lie in the He II 304A disk at their east limb, or become difficult to pick out in the short wavelength end of the spectroheliograms. In addition, the energy levels are uncertain and had to be obtained by an extrapolation of Moore's (1949) data.

5. Carbon Sequence

The carbon sequence is similar to the boron sequence in that many close blends are formed by the small term splittings.

Emission from O III is completely absent in the wavelength range under consideration here, although Moore's (1949) tables predict three lines from the $^3P_{0,1,2} \rightarrow {}^3S_1$ multiplet at 507.4A, 507.7A and 508.2A respectively. If present, these lines should appear as emission from the disk; their absence is a result of the fact that the temperatures necessary for their formation (10^5 °K) place their origin low in the chromosphere-coronal transition region. The amount of emitting material in this region appears to be very small, thus

conclusion is similar to that of Kozlovsky and Zirin (1968), who have studied the coronal emission of O VI at somewhat higher temperatures. Apparently absent also are the lines of Ne V. The resonance lines at 568A - 572A are masked anyway by the He I 584A line, but the $^3P \rightarrow {}^3P$ lines at 480A - 483A should be more easily visible if they were present with comparable intensity. The $^3P \rightarrow {}^3S$ triplet at 358A - 359A is also not in evidence.

The resonance $^3P \rightarrow {}^3D$ lines of Mg VII range from 429A to 435A and are present with fair intensity. The $^3P \rightarrow {}^3P$ lines at 364A - 368A are also present with much less intensity. The $^3P \rightarrow {}^3S$ lines at 276A - 278A are badly blended with other lines of Si VII and Si X, and in Features (3) and (4) are obscured by the He II 304A disk.

Faint images of the limb at 342A, 345A, and 350A appear to be due to the resonance lines of Si IX. The first of these, however, may be blended with second-order 171A emission from Fe IX. Both Features 3 and 4 are present at 342A, but Feature 3 takes on more of a coronal enhancement appearance than that of a plage, although a small brightening remains at the center. The $^3P \rightarrow {}^3P$ transitions suffer from interference with the He II 304A disk, and possibly also some resonance lines of S XI. The $^3P \rightarrow {}^3S$ transitions at 224A - 227A may well contribute to the very wide band of blended lines in that region. Other multiplets lying in the same region are from S IX and S X. The lines of the $^3P \rightarrow {}^3S$ multiplet of S XI at 185A - 191A do not appear.

6. Nitrogen Sequence

The ground term ^4S of the nitrogen sequence is unsplit, and connects by permitted transitions with only one other term, ^4P. Although the oscillator strengths are not particularly large, the splitting of the ^4P term is sufficient to make most of the identifications of these lines fairly reliable.

No lines of Ne IV are evident with any certainty. Mg VI appears fairly conspicuously at 399Å - 403Å, but its lines are partially blended with those of Ne VI in the same region, as described in subsection 4 of this section. The Si VIII lines at 314Å - 320Å are superimposed on a non-resonance Mg VIII multiplet, but the lower temperature at which the latter is present ($\sim$ 800,000 °K) makes these lines fairly readily distinguishable.

The spectrum of S X has been observed experimentally by Kononov (1965) who fixes the resonance quartet lines at 257.1Å, 259.5Å, and 264.3Å. The last of these is blended with Fe XIV at 264.5Å. The first two may contribute appreciably to the wide, complex blend of lines at 256Å - 258Å.

7. Oxygen Sequence

Only the resonance triplet of Mg V at 351Å - 355Å is evident with any degree of certainty as a weak series of plage images of Feature 3. The lines of Si VII at 273Å - 278Å are covered by the He II disk, and the lines of S IX at 221Å - 229Å (Kononov 1965) are badly blended with other lines of Si IX.

8. Fluorine Sequence

The resonance lines of the fluorine sequence mirror the resonance doublets of the lithium sequence; an inverted $^2P_{3/2,\ 1/2}$

term connects with a ^2S term. The two lines of Mg IV are not apparent at 321A and 323A, but Si VI emits weakly at 246.0A and 249.1A. The two lines of S VIII occur at 198.6A and 202.7A in a region that contains a large number of lines from Fe XIII (Fawcett et. al. 1966, 1967) which are very incompletely observed. The second of these lines may possibly account for a part of the emission of a long unidentified line at around 202A.

9. Spectra from n = 3 Electrons

By far the most important contribution to lines of the sodium to argon sequences comes from iron in the corona. The spectra of Fe VIII - Fe XIV in the region from 170A to 220A were largely unknown until comparatively recently due to the long uncertain extrapolations required from elements of lower ionization in the same series. Because of their intensity and strong analogy with the lithium and beryllium sequences, the resonance lines of Fe XVI at 335.4A and 360.8A and of Fe XV at 284.1A were easily identified shortly after their first observations. (Hinteregger 1961; Hall, Damon and Hinteregger 1963). Another possible line of the magnesium sequence is Ca IX at 466.2A which is visible in the spectroheliograms as a faint line just to the red of Ne VII 465.3A. Diffuse emission from Feature 1 at about 290A suggests that Ni XVIII 293.3A of the Na I sequence may be partially responsible; however, the companion line at 322.0A does not appear.

The remaining sequences, from aluminum (Fe XIV) to argon (Fe IX) are represented in the spectroheliograms solely by iron. The lines from these spectra divide themselves into two groups --

screening transitions of the type $3s^2 3p^n \rightarrow 3s3p^{n+1}$ and transitions involving a p → d jump, $3p^n \rightarrow 3p^{n-1}3d$. The former are the resonance spectra but are quite poorly known. The lines arising from these transitions lie in the region of 340A - 390A (Varsavsky 1961, House 1967). Several lines of low to moderate intensity are evident in this region and may in the future be attributed to iron.

The 3p → 3d transitions of Fe IX - XIV span the range of 171A to 220A and result in strong emission from the corona for which detailed identification has only recently been established. The first step in identifying these lines was made by Fawcett et. al. (1963) who noticed a coincidence between the solar lines and those present in a Zeta discharge. It appeared that the Zeta iron lines resulted from contamination of the plasma by the steel walls. Further work by Elton et. al. (1964), House, Deutschmann, and Sawyer (1964), and by the Culham Laboratory group in England (Fawcett and Grabriel 1965, 1966; Gabriel, Fawcett, and Jordan 1965, 1966; and Fawcett, Gabriel, and Saunders 1967) has resulted in a gradual identification of the lines in this region, the most recent being those of Fe XIII.

As the n = 3 shell empties from Fe IX to Fe XIV the wavelengths of the 3p → 3d transitions slowly increase in a regular manner. The Fe VIII ion, although belonging to the potassium sequence has a ground configuration of $3p^6 3d$ rather than $3p^6 4s$. The resonance lines therefore arise from screening transitions $3p^6 3d\ ^2D_{3/2,\ 5/2} \rightarrow 3p^5 3d^2\ ^2F_{5/2,\ 7/2}$ at 186.6A and 185.2A. This reverses the trend of decreasing wavelength with decreasing ionization.

TABLE III-1

Li I sequence

$2s \rightarrow 2p$

Trans	Mg X		Al XI		Si XII		P XIII		S XIV	
	λ	f_{eff}	λ	f_{eff}	λ	f_{eff}	λ	f_{eff}	λ	f_{eff}
$^2S_{1/2} \rightarrow {}^2P_{1/2}$	625.3	.045	568.5	.040	521.1	.035	481.4	.035	(446)	.030
$^2S_{1/2} \rightarrow {}^2P_{3/2}$	609.8	.085	550.0	.075	499.3	.075	456.1	.065	(421)	.060

Table III-2

Be I sequence

$2s^2 \rightarrow 2s2p$

	O V		Ne VII		Na VIII		Mg IX		Al X		Si XI		P XII		S XIII	
Trans	λ	f_{eff}	λ	f_{eff}	λ	f_{eff}	λ	f_{eff}	λ	f_{eff}	λ	f_{eff}	λ	f_{eff}	λ	f_{eff}
$^1S_o \rightarrow {}^1P_1$	629.7	.87	465.3	.63	411.1	.56	368.1	.50	332.9	.45	303.6	.41	278.7	.38	(257.3)	.36
			$2s^2p \rightarrow 2p^2$										$2s^2p \rightarrow 2p^2$			
$^3P_2 \rightarrow {}^3P_1$							441.1		397.7		361.3		324.9			
$^3P_1 \rightarrow {}^3P_0$							445.9		403.6		368.4		328.3			
$^3P_2 \rightarrow {}^3P_1$							443.4		400.4		364.5		328.3			
$^3P_1 \rightarrow {}^3P_2$							439.2		395.4		358.5		328.3			
$^3P_2 \rightarrow {}^3P_1$							448.3		406.4		371.7		335.6			
$^3P_2 \rightarrow {}^3P_2$							444.0		401.2		365.4		335.6			

TABLE III-3

B I sequence

$2s^2 2p \rightarrow 2s2p^2$

Trans	O IV λ	O IV f_{eff}	Ne VI λ	Ne VI f_{eff}	Mg VIII λ	Mg VIII f_{eff}	Si X λ	Si X f_{eff}	S XII λ	S XII f_{eff}
$^2P_{1/2} \rightarrow {}^2D_{3/2}$			558.6	.05	430.5	.04	347.4	.04	287.1	.03
$^2P_{3/2} \rightarrow {}^2D_{3/2}$			562.7	.11	436.7	.09	356.1	.08	298.4	.06
$^2P_{3/2} \rightarrow {}^2D_{5/2}$			562.8		436.7		356.1		298.4	
$^2P_{1/2} \rightarrow {}^2S_{1/2}$	608.4	.02	429.9	.015	335.2	.011	272.0	.009	227.4	.008
$^2P_{3/2} \rightarrow {}^2S_{1/2}$	609.8	.04	432.4	.029	339.0	.022	277.3	.019	234.5	.016
$^2P_{1/2} \rightarrow {}^2P_{1/2}$	554.1	.13	401.1	.09	313.7	.07	256.6	.06	216.5	.05
$^2P_{1/2} \rightarrow {}^2P_{3/2}$	553.3	.07	399.8	.05	311.8	.04	253.8	.03	212.9	.02
$^2P_{3/2} \rightarrow {}^2P_{1/2}$	555.3	.07	403.3	.05	317.0	.04	261.2	.03	222.9	.02
$^2P_{3/2} \rightarrow {}^2P_{3/2}$	554.5	.33	401.9	.24	315.0	.18	258.4	.14	219.1	.12
				$2s2p^2 \quad 2p^3$						
$^4P_{1/2} \rightarrow {}^4S_{3/2}$			451.6		352.4		287.2		240.8	

TABLE III-3 (cont.)

B I sequence

$2s^2 2p \rightarrow 2s2p^2$

Trans	O IV		Ne VI		Mg VIII		Si X		S XII	
	λ	f_{eff}	λ	f_{eff}	λ	f_{eff}	λ	f_{eff}	λ	f_{eff}
$^4P_{3/2} \rightarrow {}^4S_{3/2}$			452.6		353.8		289.3		243.5	
$^4P_{5/2} \rightarrow {}^4S_{3/2}$			454.0		356.0		292.3		247.8	

Table III-4

C I sequence

$2s^2 2p^2 \rightarrow 2s2p^3$

	O III		Ne V		Mg VII		Si IX		S XI	
Trans	λ	f_{eff}	λ	f_{eff}	λ	f_{eff}	λ	f_{eff}	λ	f_{eff}
$^3P_o \rightarrow {}^3D_1$			568.4	.02	429.1	.018	342.0	.013	280.6	.012
$^3P_1 \rightarrow {}^3D_1$			569.8	.07	431.2	.05	345.0	.04	284.0	.04
$^3P_1 \rightarrow {}^3D_2$			569.8		431.3		345.1		285.7	
$^3P_2 \rightarrow {}^3D_1$			572.0	.02	434.6	.014	349.7	.011	287.7	.07
$^3P_2 \rightarrow {}^3D_2$			572.1		434.7		349.8		289.5	
$^3P_2 \rightarrow {}^3D_3$			572.3	.09	434.9	.07	350.0	.06	289.7	.05
$^3P_o \rightarrow {}^3P_1$			480.4	.015	363.7	.012	290.6	.010	240.5	.008
$^3P_1 \rightarrow {}^3P_{2,1,0}$			481.3	.05	365.2	.04	292.8	.03	243.0	.02
$^3P_2 \rightarrow {}^3P_{2,1}$			482.9	.08	367.7	.06	296.2	.05	245.7	.04
$^3P_o \rightarrow {}^3S_1$	507.4	.04	358.0	.03	276.1	.02	223.7	.017	187.6	.014
$^3P_1 \rightarrow {}^3S_1$	507.7	.13	358.5	.08	277.0	.06	225.0	.05	189.1	.04
$^3P_2 \rightarrow {}^3S_1$	508.2	.21	359.4	.14	278.4	.11	227.0	.08	190.8	.07
$^1D_2 \rightarrow {}^1D_2$	599.6		416.2		319.0		258.1		216.2	
$^1D_2 \rightarrow {}^1P_1$	525.8		365.6		280.7		227.3		191.0	
$^1S_o \rightarrow {}^1P_1$	597.8		416.8		320.5		259.7		217.8	

Table III-5

N sequence

$2s^2 2p^3 \rightarrow 2s2p^4$

	Ne IV		Mg VI		Si VIII		S X	
Trans	λ	f_{eff}	λ	f_{eff}	λ	f_{eff}	λ	f_{eff}
$^4S_{3/2} \rightarrow {}^4P_{5/2}$	543.9	.25	403.3	.18	319.8	.14	264.3	.12
$^4S_{3/2} \rightarrow {}^4P_{3/2}$	542.1	.17	400.7	.12	316.2	.095	259.5	.08
$^4S_{3/2} \rightarrow {}^4P_{1/2}$	541.1	.08	399.3	.06	314.3	.048	257.1	.04
$^2D_{5/2} \rightarrow {}^2D_{5/2}$	469.8		349.2		277.1		228.7	
$^2D_{5/2} \rightarrow {}^2D_{3/2}$	469.8		349.1		277.1			
$^2D_{3/2} \rightarrow {}^2D_{5/2}$	469.8		349.2		276.9			
$^2D_{3/2} \rightarrow {}^2D_{3/2}$	469.8		349.1		276.8		228.2	
$^2D_{5/2} \rightarrow {}^2P_{3/2}$	358.7		270.4		216.9		180.7	
$^2D_{3/2} \rightarrow {}^2P_{3/2}$	358.7		270.4		216.8		180.4	
$^2D_{3/2} \rightarrow {}^2P_{1/2}$	357.8		269.0		214.8		177.6	
$^2P_{3/2} \rightarrow {}^2D_{5/2}$	521.8		388.0		308.3		225.1	
$^2P_{3/2} \rightarrow {}^2D_{3/2}$	521.8		388.0		308.2			
$^2P_{1/2} \rightarrow {}^2D_{3/2}$	521.7		387.8		307.7			
$^2P_{1/2} \rightarrow {}^2S_{1/2}$	421.6		314.6		250.6			
$^2P_{3/2} \rightarrow {}^2S_{1/2}$	421.6		314.7		251.0			
$^2P_{3/2} \rightarrow {}^2P_{3/2}$	388.2		293.1		235.6			
$^2P_{3/2} \rightarrow {}^2P_{1/2}$	387.2		291.5		233.2		196.8	
$^2P_{1/2} \rightarrow {}^2P_{3/2}$	388.2		293.0		235.2			
$^2P_{1/2} \rightarrow {}^2P_{1/2}$	387.2		291.4		232.8			

Table III-6

O I sequence

$2s^2 2p^4 \rightarrow 2s2p^5$

Trans	Mg V λ	Mg V f_{eff}	Si VII λ	Si VII f_{eff}	S IX λ	S IX f_{eff}
$^3P_2 \rightarrow {}^3P_2$	353.1	.14	275.4	.11	224.8	.69
$^3P_2 \rightarrow {}^3P_1$	351.1	.05	272.6	.04	221.3	.03
$^3P_1 \rightarrow {}^3P_2$	355.3	.05	278.4	.04	228.9	.03
$^3P_1 \rightarrow {}^3P_1$	353.3	.02	275.7	.02	225.3	.018
$^3P_1 \rightarrow {}^3P_o$	352.2	.04	274.2	.03	223.3	.02
$^3P_o \rightarrow {}^3P_1$	354.2	.04	276.8	.03	226.6	.02
$^1D_2 \rightarrow {}^1P_1$	276.6		217.8		179.3	
$^1S_o \rightarrow {}^1P_1$	312.3		246.1		202.6	

Table III-7

F I sequence

$2s^2 2p^5 \rightarrow 2s2p^6$

	Mg IV		Si VI		S VIII	
Trans	λ	f_{eff}	λ	f_{eff}	λ	f_{eff}
$^2P_{3/2} \rightarrow {}^2S_{1/2}$	321.0	.15	246.0	.11	198.6	.09
$^2P_{1/2} \rightarrow {}^2S_{1/2}$	323.3	.07	249.1	.06	202.7	.04

Table III-8

p - d transitions of Fe ions

Ion	Transition	ΔJ	λ
Fe XIII	$3p^6 3d\ ^2D - 3p^5 3d^2\ ^2F$	5/2-7/2	185.2
		3/2-5/2	186.6
Fe IX	$3p^6\ ^1S \rightarrow 3p^5 3d\ ^1P$	0 - 1	171.1
Fe X	$3p^5\ ^2P \rightarrow 3p^4 3d\ ^2P$	3/2-3/2	177.2
	$^2P \rightarrow\ ^2D$	1/2-3/2	175.3
		3/2-5/2	174.6
Fe XI	$^3p^4\ ^1D \rightarrow 3p^3 3d\ ^1F$	2 - 3	179.8
	$^3P \rightarrow\ ^3D$	2 - 3	180.4
		1 - 2	182.2
		0 - 1	181.1
		2 - 2	178.0
		1 - 1	---
Fe XII	$3p^3\ ^2D_{5/2} \rightarrow 3p^2 3d^2 F_{7/2}$	5/2-7/2	186.9
	$^4S \rightarrow\ ^4P$	3/2-1/2	192.4
		3/2-3/2	193.5
		3/2-5/2	195.1
Fe XIII	$3p^2\ ^1D - 3p3d\ ^1F$	3 - 4	196.6
	$^3P \rightarrow\ ^3D$	2 - 3	203.8
		1 - 2	
		0 - 1	
		2 - 2	
		1 - 1	
Fe XIV	$3p\ ^2P - 3d\ ^2D$	1/2-3/2	211.3
		3/2-5/2	219.1

Table III-9

s → p transitions of Fe ions

Ion	Transition	ΔJ	λ(A)
Fe X	$3s^2\ 3p^5\ ^2P \rightarrow 3s\ 3p^6\ ^2S$	3/2-1/2	347
		1/2-1/2	367
Fe XI	$3s^2\ 3p^4\ ^3P \rightarrow 3s\ 3p^5\ ^3P$	2 - 2	358
		2 - 1	350
		1 - 2	376
		1 - 1	367
		1 - 0	360
		0 - 1	369
Fe XII	$3s^2\ 3p^3\ 4S \rightarrow 3s\ 3p^4\ ^4P$	3/2-1/2	356
		3/2-3/2	360
		3/2-5/2	369
Fe XIII	$3s^2\ 3p^2\ ^3P \rightarrow 3s\ 3p^3\ ^3D$	0 - 1	360
		1 - 2,1	373
		2 - 3,2,1	386
Fe XIV	$3s^2\ 3p\ ^2P \rightarrow 3s\ 3p^2\ ^2D$	3/2-5/2,3/2	370
		1/2-3/2	346
	$3s^2\ 3p\ ^2P \rightarrow 3s\ 3p^2\ ^2P$	1/2-3/2	251.8
		3/2-3/2	264.5
		3/2-1/2	270.5
	$3s^2\ 3p^2\ P \rightarrow 3s\ 3p^2\ ^2S$	1/2-1/2	274.3
		3/2-1/2	288.7
Fe XV	$3s^2\ ^1S \rightarrow 3s\ 3p\ ^1P$	0 - 1	284.1
Fe XVI	$3s^2\ S \rightarrow 3p\ ^2P$	1/2-1/2	360.8
		1/2-3/2	335.4

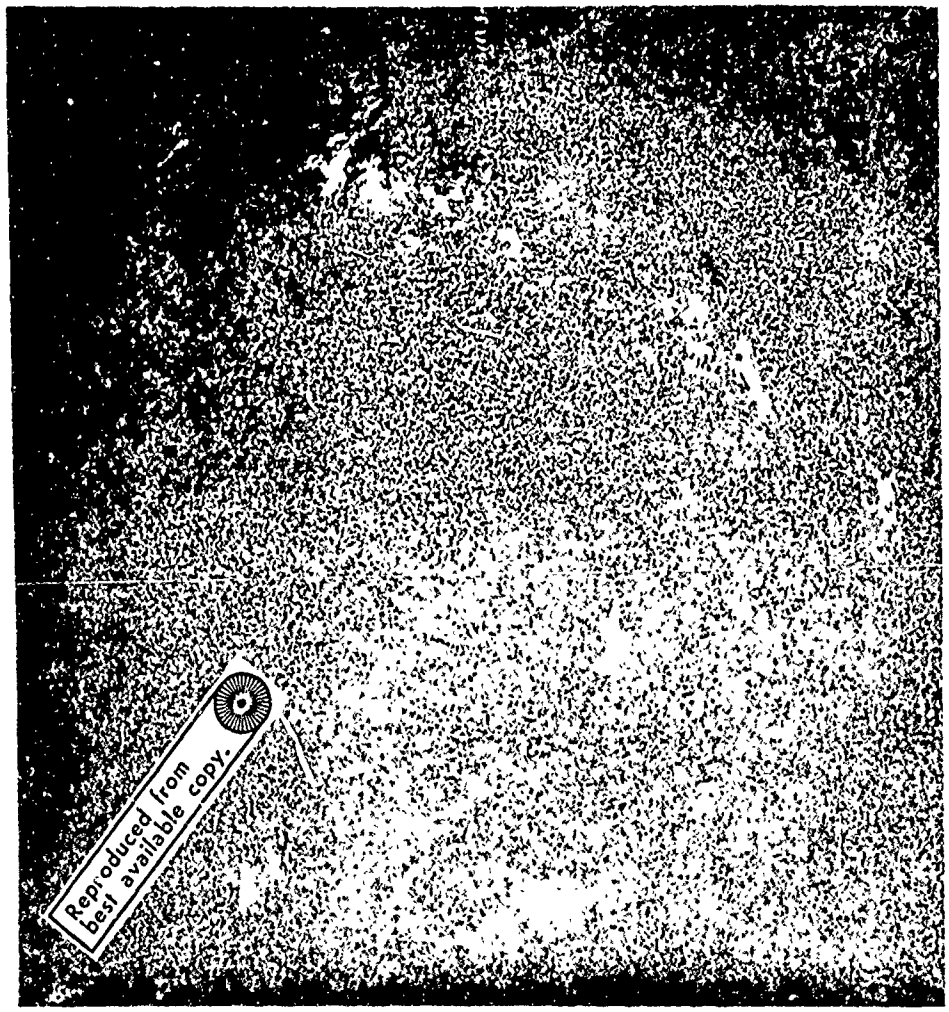

Figure III-1. The solar disk in H-alpha on April 28, 1966. (Sacramento Peak Observatory photograph).

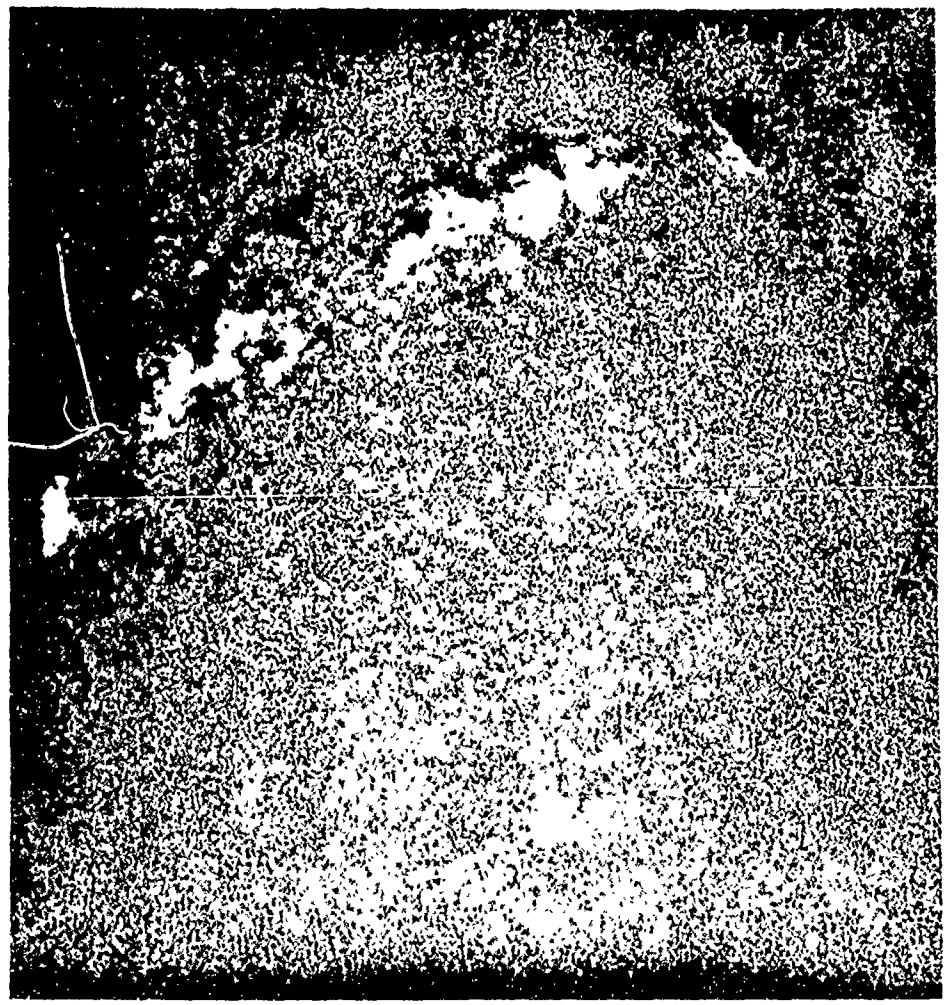

Figure III-2. The solar disk in Ca-K on April 28, 1966. (McMath-Hulbert Observatory photograph).

Figure III-3. Coronagraph spectrum of the solar limb in the wavelength region 6374A. (Courtesy, Sacramento Peak Observatory).

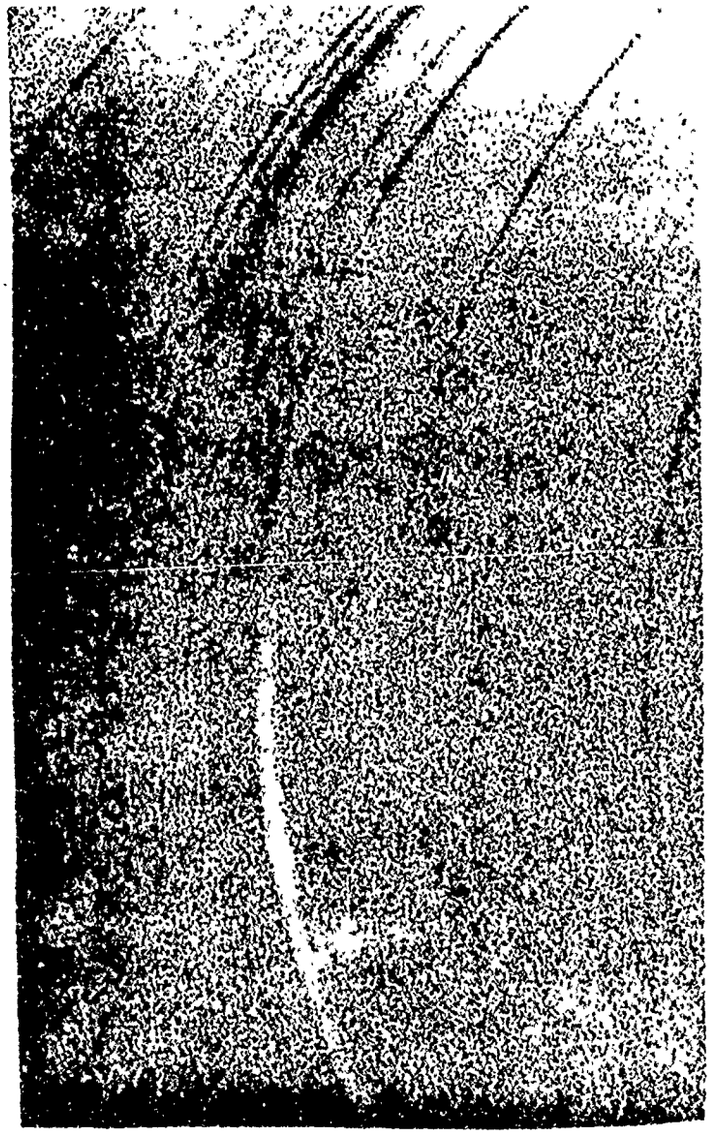

Figure III-4. Coronagraph spectrum of the solar limb in the wavelength region 5303A. (Courtesy, Sacramento Peak Observatory).

PART TWO -- THEORY OF CORONAL RADIATION IN THE EXTREME ULTRAVIOLET

CHAPTER IV

IONIZATION

A. The Coronal Approximation

The presence of a line spectrum from any source of radiation offers a means of determining both the chemical composition within the source and the physical conditions under which the lines are formed. As a gas is heated, its atoms become ionized to a degree which, in general, depends both on the temperature and density of the gas, and the extent to which the gas departs from thermodynamic equilibrium. Similarly, the ions become excited to a degree that also varies with the same physical parameters. Since excitation of a given ion presupposes that physical conditions necessary for the ion's formation are present, we shall consider the problem of ionization first, in this chapter, and treat excitation later, in Chapter V. It is not immediately obvious that these two processes may be decoupled; for example, ionization may occur from any state of excitation of the parent ion, and excitations may occur by recombinations from the next higher stage of ionization to an excited level. For the present, I shall assume that the processes may be decoupled, and later examine the effects of possible deviations from this assumption.

Soon after the high temperature of the solar corona became apparent, Biermann (1947), and Woolley and Allen (1948) realized

that the dominant processes governing ionization equilibirum in the corona are ionization by electron-ion collisions and recombination by ion-electron radiative capture. If $q_{i,i+1}$ and $\alpha_{i+1,i}$ are the respective rate coefficients for these two processes, and N_e, N_i, and N_{i+1} represent the number densities of electrons and ions of a given element in ionization stages i and i+1 respectively, then

$$N_e N_i q_{i,i+1} = N_e N_{i+1} \alpha_{i+1,i} \quad (1)$$

or

$$\frac{N_i}{N_{i+1}} = \frac{\alpha_{i+1,i}}{q_{i,i+1}} \quad (2)$$

represents the equilibrium population ratio. In nearly all cases the rate coefficients are functions of temperature only; therefore such an ionization balance renders the ion population density independent.

The validity of the form of (2) for computing ionization equilibria is still recognized today, but computation of the rate coefficients has been greatly refined. Early attempts to calculate the collisional ionization rate employed the Born plane-wave approximation (Biermann 1947, Miyamoto 1949). This approximation assumed that the electron energies are large compared to the ion's Coulomb field potential, and that the electron therefore may be treated as a plane wave. This condition is poorly satisfied in the corona where ionization is by thermal electrons with energies close to the threshold energy at least under non-flare conditions.

More rigorous classical cross sections were computed by Woolley and Allen (1948) and Elwert (1952). Later the cross sections were recomputed quantum-mechanically by Schwartz and Zirin (1959) and Burgess (1960). The former computation used Coulomb waves and considered only the S angular momentum states, whereas Burgess considered the general case for hydrogenic ions. The agreement between the classical and quantum-mechanical computations with Coulomb field is quite good.

More recent refinements in coronal ionization theory include additional processes which affect the ionization in varying amounts. We shall discuss each of these and its effects in turn.

B. Dielectronic Recombination

By the early 1960's a serious discrepancy between the ionization temperatures computed from the coronal emission lines and the temperatures computed from the lines' Doppler broadenings was evident. A significant advance in removing this discrepancy was made by Burgess (1964, 1965a) and Burgess and Seaton (1964) with the proposal that the recombining electron may also excite the capturing ion and in so doing form a doubly excited state. This dielectronic recombination process had been recognized for some time (Massey and Bates 1942, Bates and Dalgarno 1962) but Burgess was the first to show that for electron temperatures nearly equal to the excitation energies, dielectronic recombination can dominate the ordinary radiative recombination by as much as one or two orders of magnitude. Calculations of the ionization curves of Fe made by Burgess and Seaton (1964) show that the temperature of maximum abundance for each

ion is approximately doubled, and that the ionization curves are less sharply peaked than those of previous calculations (Seaton 1962, House 1964).

If the dielectronic recombination rate is included in $\alpha_{i+1,i}$ of (2) then the recombination rate is density independent only in the low density approximation. The reason for this is that ions with extremely large quantum numbers may be formed in the dielectronic recapture process, and these ions may be destroyed by ionizing collisions before they have time to radiate. The energy level at which this effect occurs is called the thermal limit of the ion. Work is now in progress by Burgess and other investigators to produce ionization curves that properly take into account the density effects. For the present, we may easily compare the radiative de-excitation and collisional ionization rates of ions of large principal quantum number n, and find out what sort of quantum numbers may exist under coronal conditions.

Consider the classical value for the total oscillator strength of an hydrogenic ion for all transitions from the n to the n' shell. This is given by

$$f_{nn'} = 1.96 \times \frac{1}{n^2} \frac{1}{\left[\frac{1}{n'^2} - \frac{1}{n^2}\right]^3} \left(\frac{1}{n^3} \frac{1}{n'^3}\right) \qquad (3)$$

The Einstein A-coefficients follow immediately from eq. (3), and are

$$A_{nn'} = 8.05 \times 10^9 \, Z^4 \left(\frac{1}{n'^2} - \frac{1}{n^2}\right)^2 f_{nn'} \qquad (4)$$

The lifetime of state n against radiative decay is then

$$\frac{1}{\tau_{rad}(n)} = \sum_{n'=1}^{n-1} A_{nn'} = \frac{1.58\times10^{10}}{n^3} Z^4 \sum_{n'=1}^{n-1} \frac{1}{n'(n^2-n'^2)} \qquad (5)$$

Evaluation of (5) is straightforward if we replace the summation by an integration. For n reasonably large, the assumption of continuity of n' will make no significant difference. We have

$$\frac{1}{\tau_{rad}(n)} = \frac{1.58\times10^{10}}{n^3} Z^4 \int_1^{n-1} \frac{dn'}{n'(n^2-n'^2)}$$

$$= 7.9 \times 10^9 \frac{Z^4}{n^5} \ln\left[\frac{(n-1)^3(n+1)}{2n-1}\right] \qquad (6)$$

Equation (6) gives an analytic representation of the radiative lifetime of the n-shell of an hydrogenic ion. We see that, apart from a slowly-varying logarithmic factor, $\tau_{(n)} \propto n^5$, and the ions of large quantum number become extremely long-lived if left undisturbed.

The destruction of these large ions is chiefly by collisional ionization, whose rate coefficient is given by (Burgess and Seaton 1964)

$$q_{i,i+1} = 2 \times 10^{-8} \frac{T^{\frac{1}{2}} \xi_i}{\chi^2} \exp(-11605\chi/T) \qquad (7)$$

where ζ_i is the number of electrons in the outer shell, χ is the ionization potential in electron volts, and T is the electron temperature. For an hydrogenic ion, $\zeta_i = 1$. Furthermore, for large values of n, the argument of the exponential is small and the exponential function approaches unity. We may further express χ_n, the ionization potential from the nth shell by

$$\chi_n = \frac{13.59}{n^2} Z^2 \tag{8}$$

If we substitute (8) into (7) and invoke the approximations described above we obtain

$$q_n = 2.72 \times 10^{-7} T^{\frac{1}{2}} n^4/Z^4 \tag{9}$$

From (9), we may obtain the lifetime against collisional ionization of an ion in state n, which is simply,

$$\tau_{coll}(n) = (N_e q_n)^{-1} \tag{10}$$

In addition to collisional ionization and radiative de-excitation, we need to consider the possible effects of collisional excitations and de-excitations in establishing the thermal limit of an ion. A collisional excitation will raise the energy level of the outer electron to a higher level which will almost certainly be ionized; a de-excitation will lower the energy to a level that may easily decay by either radiation or a further collision. The additional tendency for the ion to undergo further ionization will then be the sum of all collisional excitation rates minus the sum of all collisional de-excitation rates from state n. A comparison of this

difference with the direct collisional ionization rate will show whether or not we may safely ignore excitations and de-excitations by collisions.

We may assume that the collisional excitation rate is that given by Van Regemorter (1962)

$$C_{nn'} = \frac{1.7 \times 10^{-3}}{W_{nn'} T^{\frac{1}{2}}} f_{nn'} \exp\left(- \frac{11605\, W_{nn'}}{T}\right) \tag{11}$$

with the Gaunt factor of order unity. If the energy of the excitation is small compared with the mean thermal energy of the exciting electrons, the value of the exponential will be nearly unity. Upon substituting hydrogenic values for the excitation energy, $W_{nn'}$, and the oscillator strength, $f_{nn'}$ into (11), we find that

$$C_{nn'} = \frac{2.5 \times 10^{-4}}{Z^2 T^{\frac{1}{2}}} \frac{n^3 n'^5}{(n^2 - n'^2)^4} \tag{12}$$

The effect of collisional transitions will then be given by the summation of (12) over all $n' > n$ minus the summation over all $n' < n$. If we replace the summations by integrations we find that

$$\sum_{n'=n+1}^{\infty} C_{nn'} \approx \frac{2.45 \times 10^{-4}}{Z^2 T^{\frac{1}{2}}} n^3 \int_{n+1}^{\infty} \frac{n'^5\, dn'}{(n^2 - n'^2)^4} \tag{13}$$

and similarly, we may write for the de-excitations

$$\sum_{n'=1}^{n-1} C_{nn'} \approx \frac{2.45 \times 10^{-4}}{Z^2 T^{\frac{1}{2}}} n^3 \int_1^{n-1} \frac{n'^5 \, dn'}{(n^2 - n'^2)^4} \qquad (14)$$

The net effect of the collisional excitations and de-excitations is given by the difference between (13) and (14). Evaluation of the integrals gives

$$\left(\sum_{n+1}^{\infty} - \sum_{1}^{n-1} \right) C_{nn'} = 4.6 \times 10^{-5} Z^{-2} T^{-\frac{1}{2}} \left[n^3 + \mathcal{O}\left(\frac{1}{n}\right) \right] \qquad (15)$$

This expression may be compared directly with the collisional ionization rate given by (9). We find that the lifetime of the ion against collisional transitions, τ'_{coll}, as compared with collisional ionizations is

$$\frac{\tau'_{coll}(n)}{\tau_{coll}(n)} = \frac{q_n}{\left(\sum_{n+1}^{\infty} - \sum_{1}^{n-1} \right) C_{nn'}} = 5.9 \times 10^{-5} T n Z^{-2} \qquad (16)$$

This ratio is considerably greater than unity for all coronal conditions. Thus the net effect of bound-bound collisional transitions in establishing the thermal limit is negligible.

Table IV-1 shows some typical lifetimes in the range n=2 to 1000, with Z=1, $T=10^6$°K and N_e=1 cm^{-3}. For the lowest energy levels the exact quantum-mechanical values of the Einstein A's as computed by Menzel and Peckeris (1935) are used. For n=10, both classical and quantum-mechanical expressions agree to within ten percent; this agreement will improve as n increases.

The next step is to obtain an expression for the ratio of the radiative and collisional lifetimes. We may assume for any given ion that the value of the principal quantum number that yields a ratio equal to unity represents the highest state of excitation that can contribute to the dielectronic recombination process. It is possible to obtain an expression merely by taking the ratio of (6) and (10), but because of the presence of the logaritnmic factor in (6), and the breakdown of the classical assumptions for small n, it seems better to obtain an empirical formula that will make computation easier. The justification for this will be apparent by the near-linearity of the variation of $\tau_{rad}(n)/\tau_{coll}(n)$ with n on a logarithmic scale.

If we let $R_o(n) = \tau_{rad}(n)/\tau_{coll}(n)$ at $N_e = 1$, $T = 10^6$ °K, and Z = 1, we find empirically that

$$\log R_o(n) = 8.75 \log n - 14.03 \qquad (17)$$

From (6) and (9) however, we see that the ratio R(n), for any N_e, T, and Z is

$$\log R(n) = \log R_o(n) - 8 \log Z + \frac{1}{2} \log T_6 + \log N_e \qquad (18)$$

where $T_6 = T/10^6$ °K. If we combine (17) and (18), set log R(n) = 0 to correspond to a ratio of unity, and solve for log n, we find

$$\log n = 1.60 + .913 \log Z - .0571 \log T_6 - .114 \log N_e \qquad (19)$$

We see at once that the temperature dependence is so weak that we may eliminate the third term by assuming T_6 to be of order unity. The dependence on N_e is weak also, but the electron density can vary by several orders of magnitude in the corona. Table IV-2 gives values of n under which an hydrogenic ion may be considered stable against re-ionization, as a function of electron density and effective ionic charge. Note that this charge is one greater than the charge of the ion as a whole, and is numerically equal to the Roman numeral designation of the ion in astrophysical notation.

The numbers given in Table IV-2 show that collisional destruction in the denser regions of the corona may occur for ions with $n \lesssim 40$ for lower stages of coronal ionization. The thermal limit rises to $n \lesssim 80$ at densities of 10^7 and for ions in the higher stages of ionization.

Table IV-3 lists values of the correction factor, D, by which the dielectronic recombination coefficient must be multiplied to correct for the thermal limit, as a function of the quantum number, n_o, that corresponds to this limit. These values are taken from Burgess (1965c), and specifically refer only to Ca II. Since the recombining electron may be assumed to be hydrogenic in high states of excitation, the values in Table IV-3 should also be indicative of

other ions. This amounts to a significant reduction in the overall recombination rate, but since the ratio $\alpha^{d}_{i+1,i}/\alpha^{r}_{i+1,i}$ may in some cases be as large as 100 to 1000, the reduction is by a small enough factor so that for most ions the primary means of recombining will still be the dielectronic process. The effect of the destruction of the larger ions will definitely have to be evaluated before we can justify the statement that coronal ionization is density independent to a good approximation. In Section D we shall return to this question after calculating the density-independent ionization curves.

C. Two-Step Collisional Ionization

An investigation by Athay and Hyder (1963) considers the effect of an excitation by collision into an excited, metastable state followed by a second ionizing collision. If the excited level is not metastable, the probability of a radiative de-excitation is much larger than that of a collisional de-excitation, and essentially all the ions will be ionized directly from the ground state. If the reverse is true, that is, if collisional de-excitation is favored, then a detailed balance is set up between the ground and excited states, and a pseudo-Boltzmann population between the two states occurs. In this case the ion behaves essentially as two separate ions with respect to further ionization, with the ground and metastable states acting as the respective ground states. The result is a lowering and broadening of the ionization curves with a slight shift to lower temperatures.

Athay and Hyder applied this picture to iron using an electron density of 10^9 and a temperature of 8×10^5 °K. They found levels metastable under these conditions in Fe XI, XII, XIII, XIV, and XV, with excitation potentials of 138, 10 and 5.7, 26, 23, and 30 electron volts, respectively. Only Fe XI of these ions has a metastable level whose energy is larger than 10% of the ionization energy. In this particular ion, however, the energy ratio approaches 50%. Athay and Hyder then computed the relative abundances of the ions at 6×10^5 °K and at 8×10^5 °K, and compared the abundances with those computed from the one-level ions (without dielectronic recombination), and from the several-level ions in which all levels are considered metastable. This third computation represents a limiting case only. Standard theory at the time of the investigation gave an Fe X to Fe XIV abundance ratio of unity at 800,000 °K. This is shifted to about 750,000 °K and 650,000 °K for the two types of computations carried out by Athay and Hyder. If we regard the smaller shift as typical, we note the change in temperature is only slightly more than six percent. Since most coronal emission, even in normal enhancements, comes from regions of density somewhat lower than 10^9 cm^{-3}, this change in temperature is probably close to an upper limit. The effects of a variation of coronal density on ionization theory through this mechanism are thus certain to be small compared to observational uncertainties.

D. Autoionization via Doubly Excited States

Recent work by Goldberg, Dupree, and Allen (1965), and Allen and Dupree (1967) considers the possibility of an electron-ion

collision producing a doubly excited bound state of the ion with one of the electrons subsequently yielding its excitation energy to remove the other. The second part of this two-step process is the inverse of dielectronic recombination.

In their earlier work, Goldberg, Dupree, and Allen calculate the effect of collisional excitation to autoionizing levels for the ions Fe XV and XVI; O IV, V, and VI, and show that the ratio of the rate coefficient of autoionization to that of collisional ionization is a strong function of temperature, and varies considerably among the ions considered. The later work by Allen and Dupree included computations of ionization equilibrium for the ions of oxygen, neon, silicon, and iron. Among these four elements, only Fe showed a significant change in the ionization equilibrium. Curves of Fe XIV, XV, and XVI are narrowed as a result of the inclusion of autoionization, whereas others, such as those of Fe IX and XVII are broadened. Temperature shifts to lower values, which may be expected, are small when they occur, and lie between shifts in the logarithm of 0.2 to 0.15 (a factor of from 0.96 to 0.71.). The greatest shift in the maximum occurs for the ion Fe XVI. The significance of the shift is somewhat questionable, however, since it reflects more a change in the skewness of the curve than a change in its overall position along the temperature axis.

In summary, then, the statement of Allen and Dupree that "the process of autoionization cannot be ignored in the ionization equilibrium of certain elements" is certainly true in general. For many types of investigation of corona. structure, however, including

the present one, the observations are simply not accurate or unambiguous enough as yet for this refinement to have any effect on the conclusions.

E. Computation of Ionization Curves

Of the three additional processes recognized in the last decade as being possibly significant in their effect upon coronal ionization, that of dielectronic recombination produces by far the largest change in the picture. In addition, it is the only one of the three whose rate coefficient has been put in a simple enough form for a relatively fast computation for large numbers of elements in various stages of ionization. We therefore include in the computations which follow only the following processes: (1) direct collisional ionization, (2) radiative recombination, and (3) dielectronic recombination. The neglect of two-step collisional ionization, autoionization, and the effect of the thermal limit on dielectronic recombination cannot affect the total ionization rate coefficient by more than a factor of two at most, and in many cases these effects are nonexistent or negligible. The effects on the resulting equilibrium will be small and of the following nature: (a) a slight lowering of the temperatures of the ionization curves, and (b) the introduction of a small degree of sensitivity of the ionization to electron density.

The quantum-mechanical expression approximating the collisional ionization rate coefficient is given by eq. (7). The rate coefficient for ordinary radiative recombination is given by Burgess and Seaton (1964) as

$$\alpha^{r}_{i+1,i} = 1.3 \times 10^{-9} \frac{Z^{2}_{i+1} \chi^{\frac{1}{2}}}{T} \qquad (20)$$

in the hydrogenic approximation, where Z_{i+1} is the charge on the recombining ion.

In his earlier papers, Burgess (1964, 1965a) derives an expression for the dielectronic recombination rate coefficient for the individual doubly excited states. We may denote the initial state of the recombining ion as j, and the doubly excited state of the product ion as $(j',n\ell)$, where j' is the quantum state of the excited core and (n,ℓ) the quantum numbers of the outer electron. From the doubly excited state, the ion may auto-ionize with a transition $j \rightarrow k$ in the core furnishing energy to the outer electron causing it to undergo the transition to the continuum $n\ell \rightarrow E\ell'$. The transition probability for this reaction (the Auger process) is given by $A_a(j', n\ell \rightarrow k, E\ell')$. On the other hand, the inner core may de-excite radiatively to quantum state k, and leave the ion in a bound state. We denote this radiative transition probability by $A_r(j', n\ell \rightarrow k, n\ell')$. For a band of incident electrons of energy E and energy interval dE, Burgess gives the following expression for the mono-energetic dielectronic recombination coefficient:

$$\alpha^{d}_{i+1,i}(j, j'; n\ell) = \frac{h^3}{8\pi m_e^2 v}\frac{dN_e}{N_e dE}\frac{g(j'n\ell)}{g(j)} \times$$

$$\times \frac{\sum_{\ell'} A_a(j';n\ell \rightarrow j,E\ell') \sum_{k} A_r(j';n\ell \rightarrow k,n\ell)}{\sum_{k} A_r(j';n\ell \rightarrow k,n\ell) + \sum_{\ell'} A_a(j';n\ell \rightarrow k,E\ell')} \qquad (21)$$

where the g's are statistical weights. The summation over ℓ' gives the total probability of the occurrence of an autoionization following the recapture, and the summation over k represents a sum over all possible means of de-excitation of the core of the doubly-excited ion. Burgess points out that earlier assumptions that autoionization is far more likely than radiative decay are valid only in the low temperature (E/kT >> 1) approximation. In the corona this condition certainly is not present.

As it stands, Equation (21) is too cumbersome to be of much use for a general computation, and it demands a knowledge of transition probabilities which are poorly known. A more tractable expression with an accuracy of at least 10% is given also by Burgess (1965b), for a Maxwellian distribution of electron energies. It is as follows:

$$\alpha^{a}_{i+1,i} = 3 \times 10^{-3}\, T^{-3/2}\, B(Z_i) \sum_{j'} f(j'j) A(x) e^{-E/kT} \qquad (22)$$

for the recombining ion initially in state j. Also,

$$A(x) = \frac{x^{\frac{1}{2}}}{1 + .105x + .015x^2} \qquad (23)$$

$$B(Z_i) = Z_i^{1/2}(Z_i + 1)^{5/2}(Z_i + 13.4)^{-1/2} \tag{24}$$

$$x = (Z_i + 1)^2 \left(\frac{1}{\nu_j^2} - \frac{1}{\nu_{j'}^2}\right) \tag{25}$$

$$\bar{E}/kT = \frac{.158(Z_i + 1)^2 (T/10^6)^{-1} \left(\frac{1}{\nu_j^2} - \frac{1}{\nu_{j'}^2}\right)}{1 + .015\, Z_i^3\, (Z_i + 1)^{-2}} \tag{26}$$

The quantities ν_j, $\nu_{j'}$ represent the effective principal quantum numbers of the initial state j and the excited state j'.

Equation (22) still suffers from the necessity of determining accurate oscillator strengths for the excitations of the allowed doubly excited states. We can make a somewhat futher simplification by invoking the following three assumptions:

(1) The recombining ion is in the ground state. This implies that eq. (22) will represent completely $\alpha^d_{i+1,i}$ if j represents the ground state.

(2) The expression for $A(x)$ is a slowly varying function of the degree of excitation of the ion over most of the important transitions. Under assumption (1), $1/\nu_j^2 = 1/\nu_1^2$, and as the level of excitation of the recombining ion increases, $1/\nu_j^2$, rapidly approaches zero. In general, the f-values decrease for the more highly excited levels, and the resonance transitions furnish the largest single contribution to the summation in (22), although not,

final word of warning, however, it should be noted that at present there exists no set of computations that includes dielectronic recombination and also includes simultaneously the effects of two-step collisional ionization, collisional excitation plus auto-ionization, and the effect of the thermal limit. Although these last three effects may be small individually, they will tend to act together in reducing the ionization temperatures rather than cancel one another out, and their combined effect may well be appreciable. It is doubtful that any future refinements will revolutionize the state of the theory to the extent that Burgess' inclusion of dielectronic recombination has done. The present trend appears to be leading to slightly lower temperatures which, however, are still significantly higher than those of the pre-Burgess era.

field. This approximation is most accurate when the stage of ionization is relatively high and the outer electron shell of the ion is nearly empty.

Assumption (2) will lead to an overestimate of the value of $\alpha^{d}_{i+1,i}$, due primarily to an overestimate of $\bar{E}/kT$ in eq. (26) through the factor $(\nu_j^{-2} - \nu_{j'}^{-2})$, which is set equal to ν_1^{-2}. A replacement of ν_1 by n, as indicated in assumption (3) will, on the other hand, tend to decrease $\bar{E}/kT$, since in all cases $n > \nu_1$. Since the magnitude of the rate coefficient in the case of coronal ions will be affected by only a few percent either way, the combined errors will tend to cancel.

As a result of these three assumptions we can finally write eq. (22) as follows:

$$\alpha^{d}_{i+1,i} = \frac{3 \times 10^{-3}}{T^{3/2}} \frac{Z_i^{1/2}(Z_i + 1)^{5/2}}{(Z_i^2 + 13.4)^{1/2}} A_n \left(\frac{Z_i + 1}{n_1^2}\right) \zeta_{i+1} \times \exp\left\{ - \frac{.158(Z_i + 1)^2 (T/10^6)}{n_1^2 [1 + .015 Z_i^3 (Z_i + 1)^{-2}]} \right\} \quad (28)$$

$$\text{cm}^3 \text{ sec}^{-1} .$$

We can now compute the ionization curves of the various elements from eqs. (7), (20), and (28) substituted into eq. (2), with $\alpha^{r}_{i+1,i} + \alpha^{d}_{i+1,i} = \alpha_{i+1,i}$. The results of the computations for χ_{ion}, the relative abundance of each ion with respect to the total abundance of its parent element, are shown in Figures IV-2 through IV-10

for the elements O, Ne, Na, Mg, Al, Si, S, Ca, Fe, and Ni, in the temperature range from 2×10^5 to 10^7 °K.

The most obvious feature of the set of curves in Figures IV-1 through IV-10 is the fact that the curves vary greatly in both width and height, and that in general the broader the curve, the higher it is. The question of the breadth of the curves obviously centers around the question of how much energy is necessary to destroy the ions relative to the amount necessary to produce them. The broadest curves, those of the He and Ne isoelectronic sequences, represent ions that are formed by relatively low-energy collisions, but destroyed only by collisions of much higher energy. This is the result of the extreme stability of the closed electron shells, and results in a high degree of stability of such ions over a large temperature range. The fact that their curves are also higher is simply the result of the fact that at their peaks, their neighboring ions are either largely destroyed or unformed.

Because the He and Ne-type ions require energies for excitation that are a substantial fraction of their ionization energies, no significant emission from these ions is observed. They do make their presence felt in a secondary way, however. The stability of these ions insures a large reservoir of ions which may recombine to form Li and Na-type ions, and we note that the ionization curves for these ions are also considerably broadened. These ions are relatively easy to excite, and the broadening of their ionization curves contributes significantly to their strong emission.

F. Evaluation

Figures IV-11 to IV-13 show an enlargement of the ionization curves of Si XII, Fe XIV, and Fe XVI from the present investigation, indicated by alternate dot-dash curves. The solid curves show the corresponding curves of Allen and Dupree (1967) for the same ions, and include the effects of collisional excitation to autoionizing levels. Where these effects are appreciable, as with the Fe ions, the dashed curve shows the Allen and Dupree calculations with the autoionization through collisions omitted. Also shown are ionization curves recently computed by Jordan (1967) both excluding and including the effect of destruction of ions whose excitation energies lie above the thermal limit.

It is evident that the changes in the ionization curves that result from these refinements are not large. The high-temperature approximation which I used in the present computations likewise seems to have no effect large enough to be significant, in view of the limited accuracy of the observations that are to be interpreted through coronal ionization theory.

As it stands, then, coronal ionization theory appears to be in a pretty strong position generally, although numerous refinements are still possible and desirable. The present computations were carried out in the year 1966 with the goal of obtaining a reasonably good representation of the ionization features of a large number of ions with a minimum of input data. The subsequent computations which include the refinements mentioned above bear out the validity of my general formulation as a first approximation. As a

final word of warning, however, it should be noted that at present there exists no set of computations that includes dielectronic recombination and also includes simultaneously the effects of two-step collisional ionization, collisional excitation plus auto-ionization, and the effect of the thermal limit. Although these last three effects may be small individually, they will tend to act together in reducing the ionization temperatures rather than cancel one another out, and their combined effect may well be appreciable. It is doubtful that any future refinements will revolutionize the state of the theory to the extent that Burgess' inclusion of dielectronic recombination has done. The present trend appears to be leading to slightly lower temperatures which, however, are still significantly higher than those of the pre-Burgess era.

Table IV-1

Lifetimes of ions of principal quantum number n with $T = 10^6$ °K, $Z = 1$, $N_e = 1$.

	Radiative	Classical	Collisional
	Menzel & Peckeris (Quantum mechanical)		
$\tau(2)$	2.14×10^{-9}		2.30×10^{2}
$\tau(3)$	1.01×10^{-8}		4.54×10
$\tau(4)$	3.33×10^{-8}		
$\tau(5)$	8.71×10^{-8}		
$\tau(6)$	1.94×10^{-7}		
$\tau(10)$	1.92×10^{-6}	2.09×10^{-6}	3.68×10^{-1}
$\tau(14)$	8.97×10^{-6}		
$\tau(30)$		3.25×10^{-4}	4.54×10^{-3}
$\tau(100)$		9.65×10^{-2}	3.68×10^{-5}
$\tau(300)$		1.90×10	4.54×10^{-7}
$\tau(1000)$		6.31×10^{3}	3.68×10^{-9}

Table IV-2

Values of the thermal limit, n_o, for $T = 10^6$ °K. For $T = .5 \times 10^6$, multiply by 1.04. For $T = 5 \times 10^6$, multiply by .913.

Z	log N_e 5	6	7	8	9	10
6	55	42	32	25	20	15
7	63	49	37	29	22	17
8	70	55	43	32	25	19
9	79	62	47	36	28	21
10	87	68	51	40	31	23
11	95	74	56	44	34	25
12	105	79	62	47	36	28
13	117	91	69	54	42	32
14	123	96	72	56	44	33
15	126	98	74	58	45	34
16	135	105	79	62	48	36
17	141	110	83	65	50	38
18	151	118	89	69	54	41

Table IV-3

The reduction D in the dielectronic recombination coefficient as a function of the principal quantum number of the thermal limit, n_o.

n_o	D
200	.91
100	.62
60	.43
20	.15
10	.06
8	.04
6	.02

Figures IV-1 to IV-10.

Ionization curves of some of the more common elements. The quantity X_{ion} refers to the fraction of the atoms of the element in question in the state of ionization represented by the curve. Although Arabic numerals are used for improved readability, the numbers represent astrophysical rather than spectroscopic notation. For example, curve 14 in the Fe graph represents Fe XIV, not Fe^{+14}.

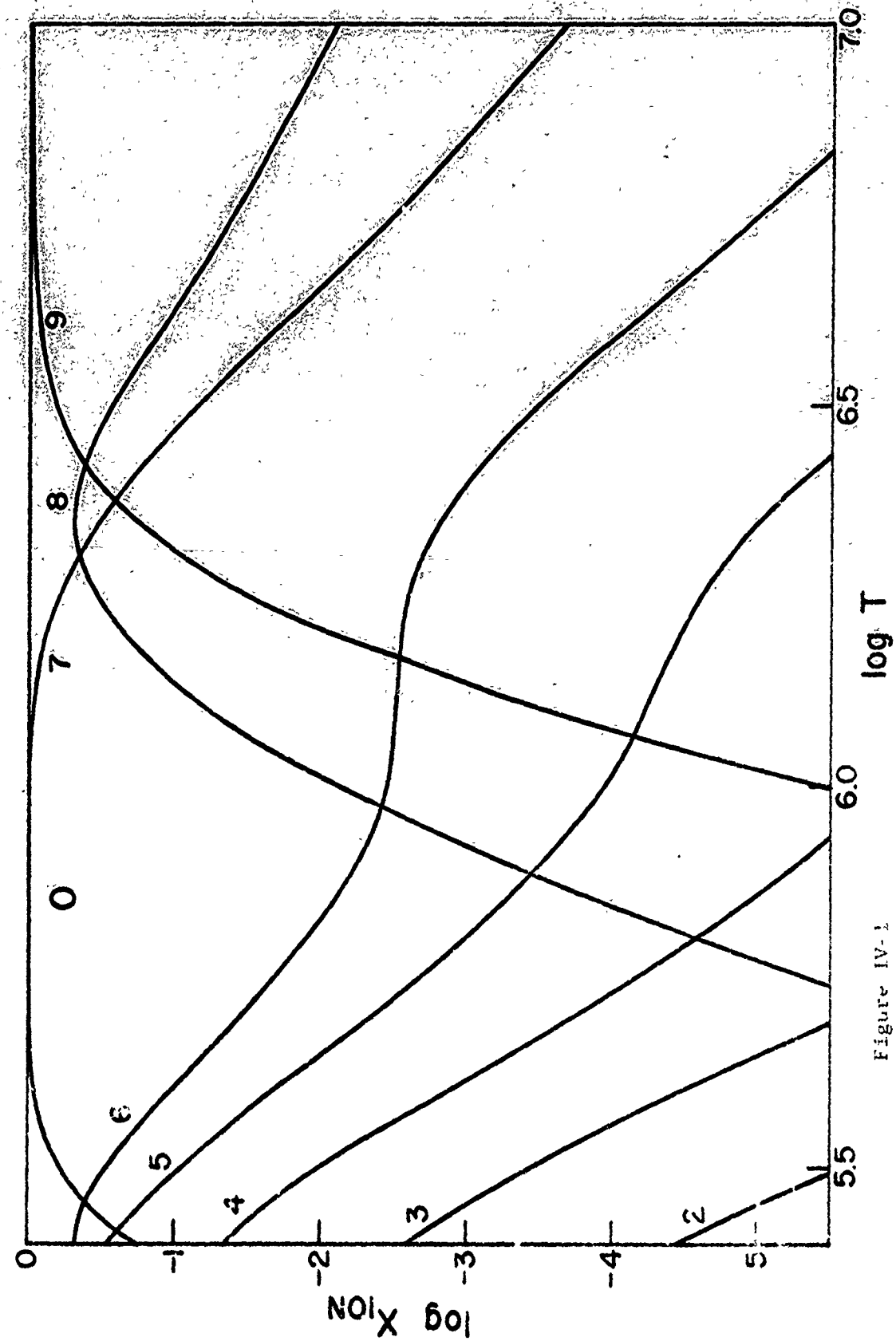

Figure IV-1

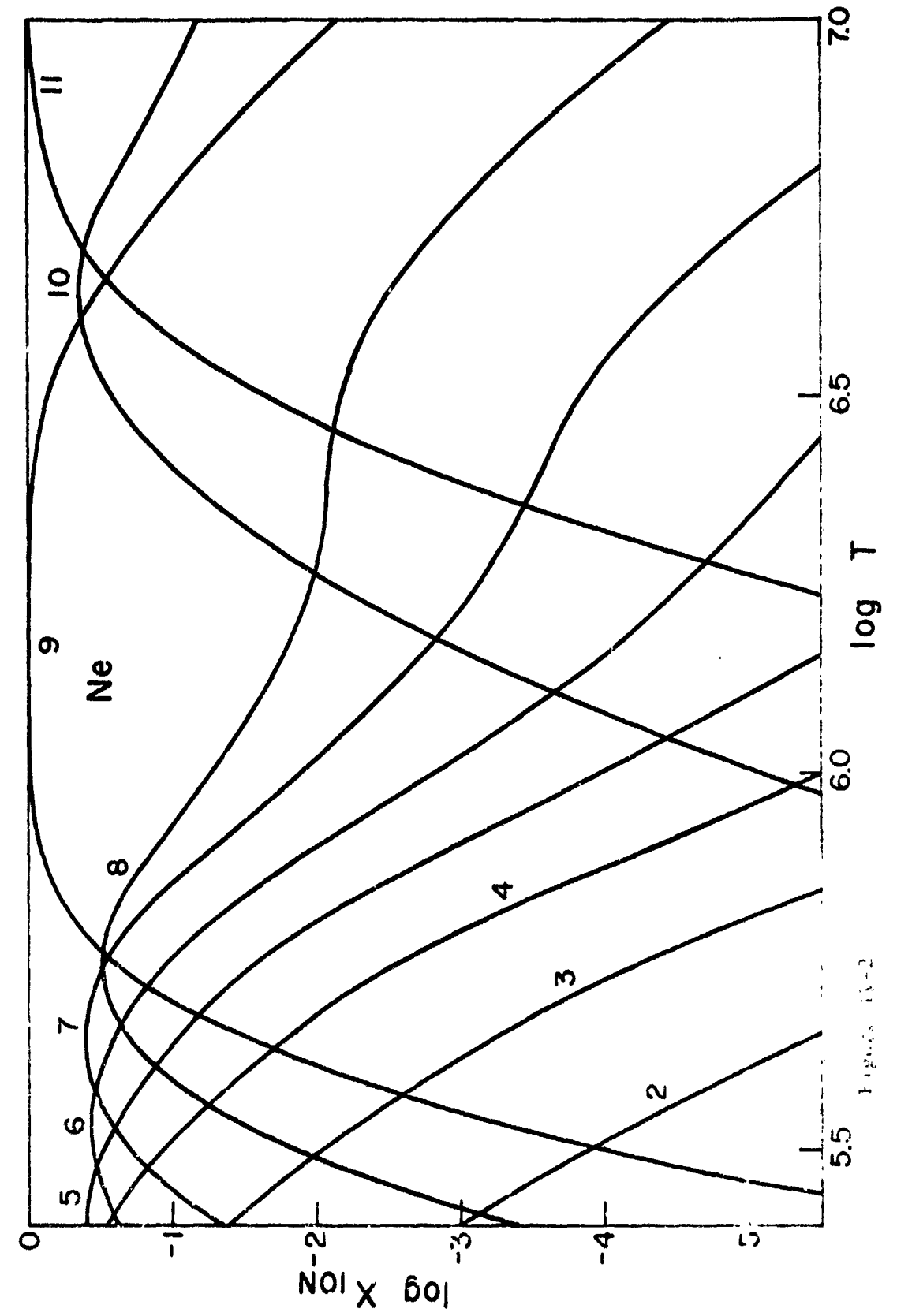
Ne
log X ION
log T
0
-1
-2
-3
-4
5
5.5
6.0
6.5
7.0
2
3
4
5
6
7
8
9
10
11

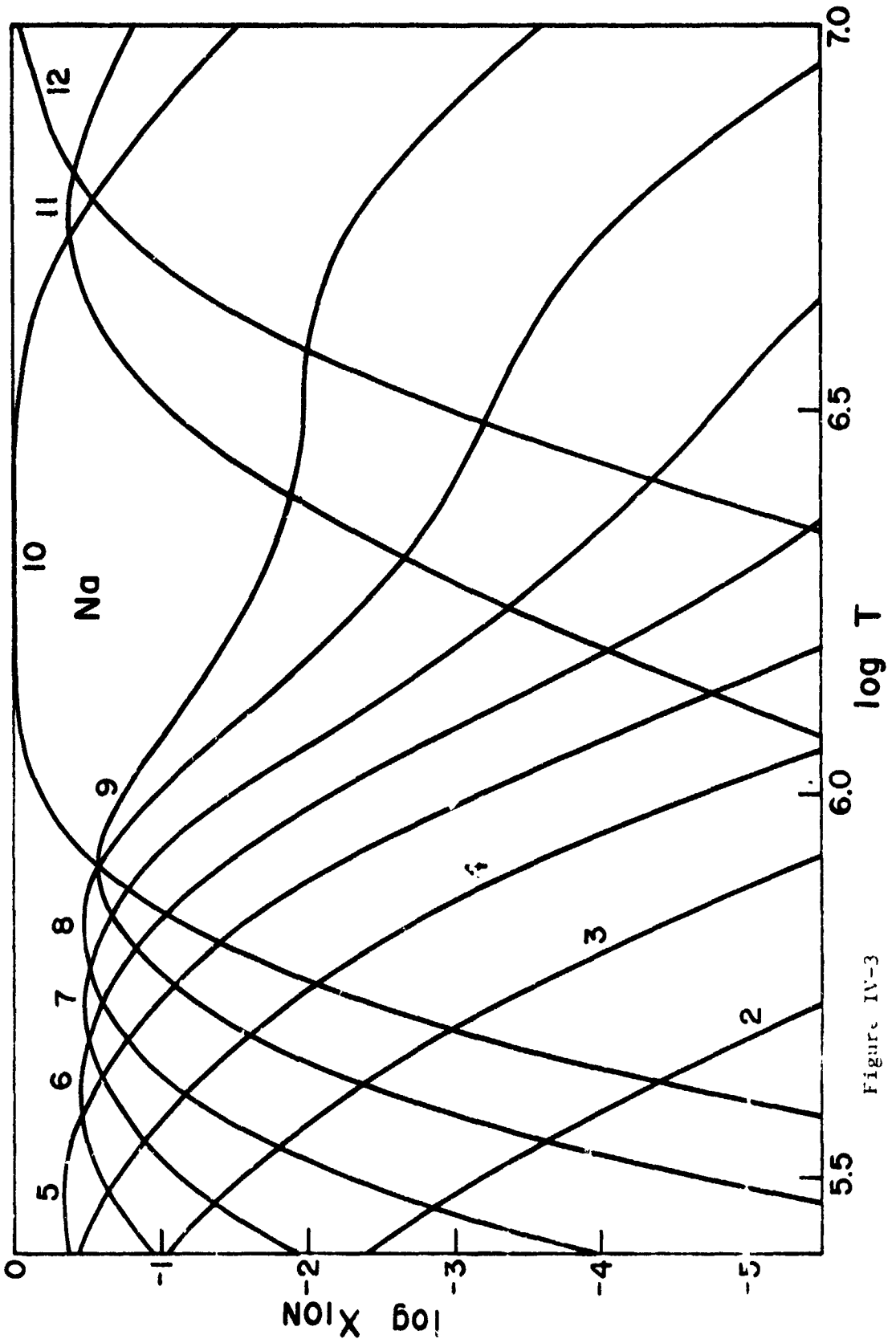

Figure IV-3

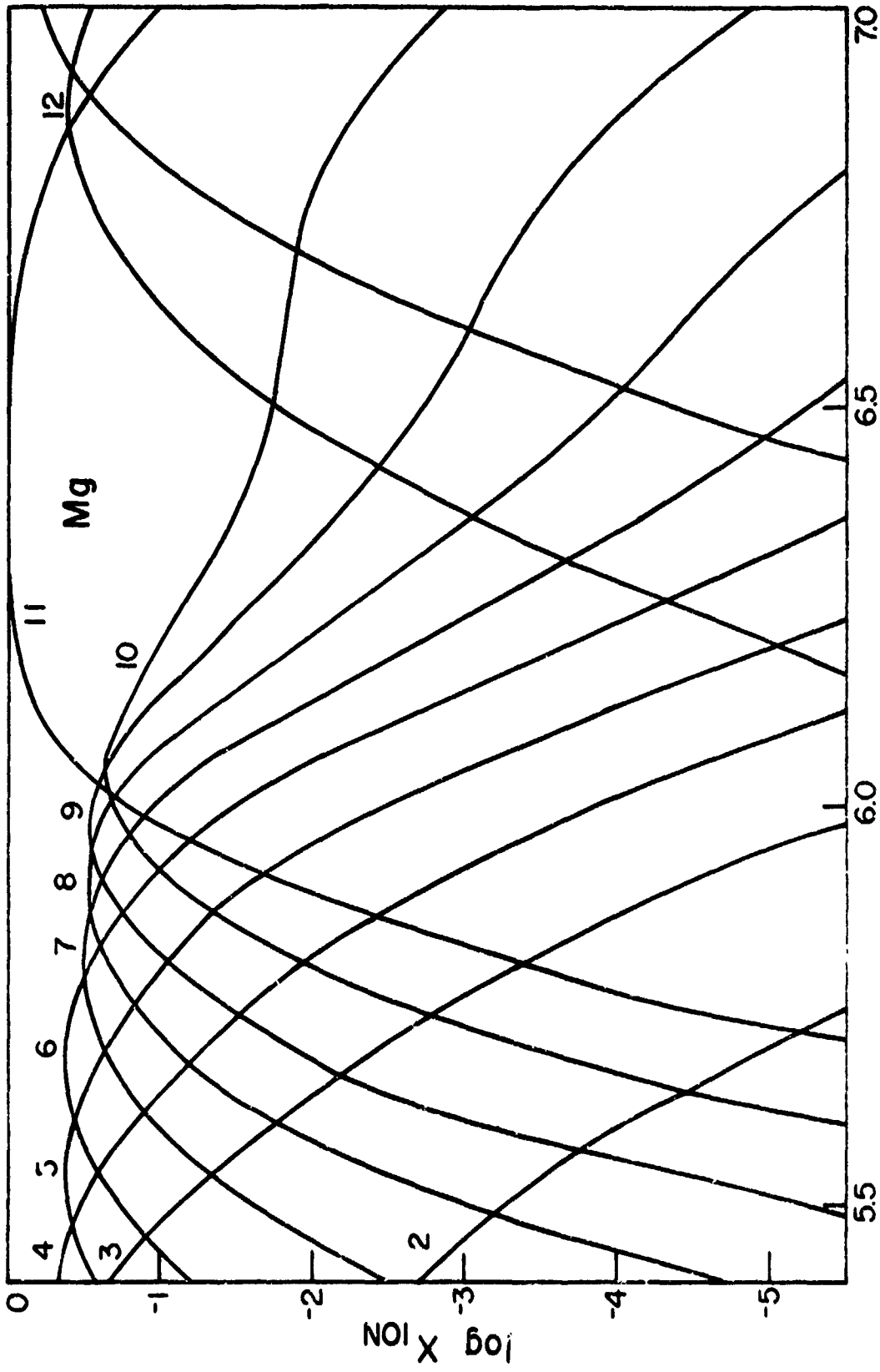

Figure IV-4

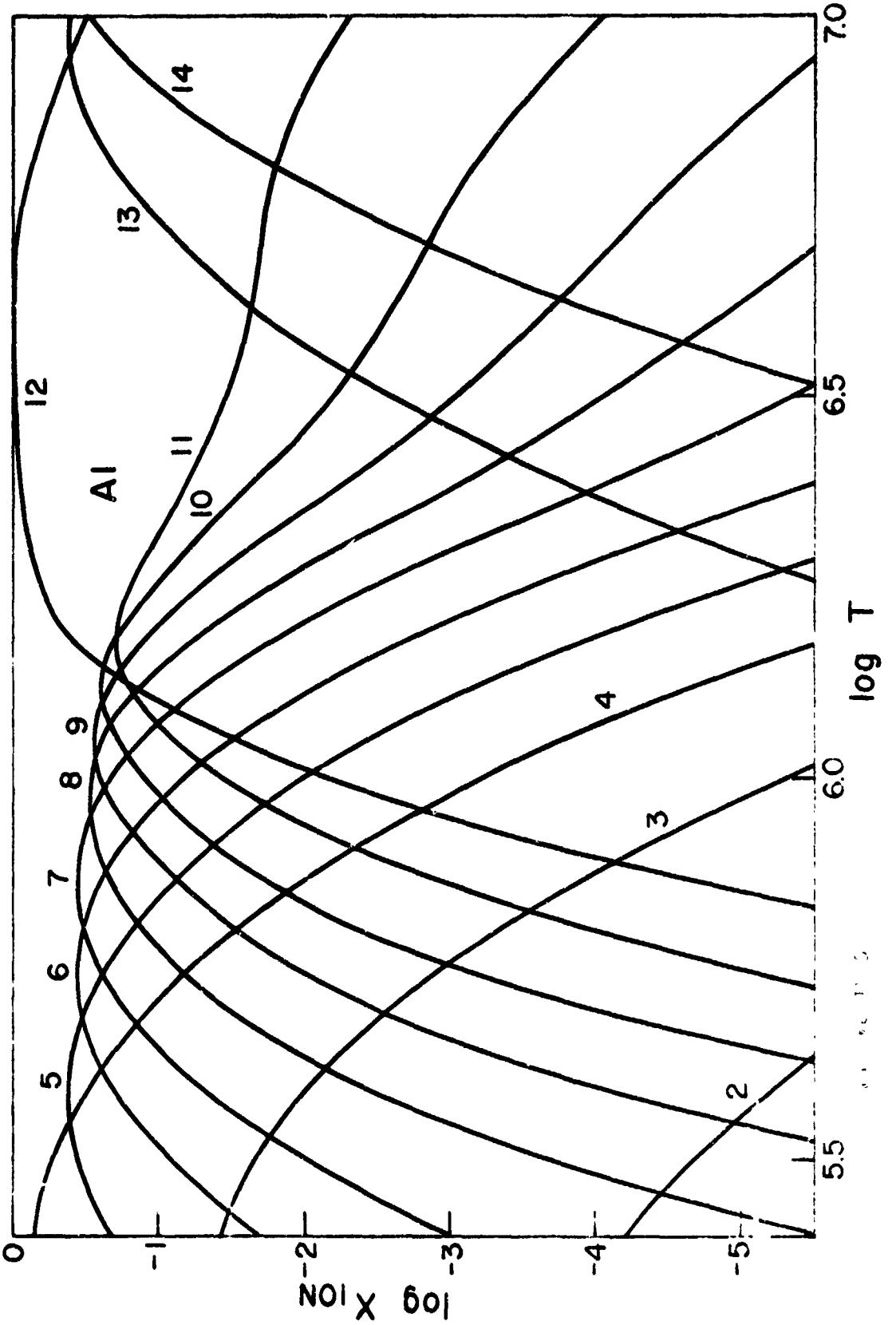
Al
1
2
3
4
5
6
7
8
9
10
11
12
13
14
0
-1
-2
-3
-4
-5
log X ION
5.5
6.0
6.5
7.0
log T

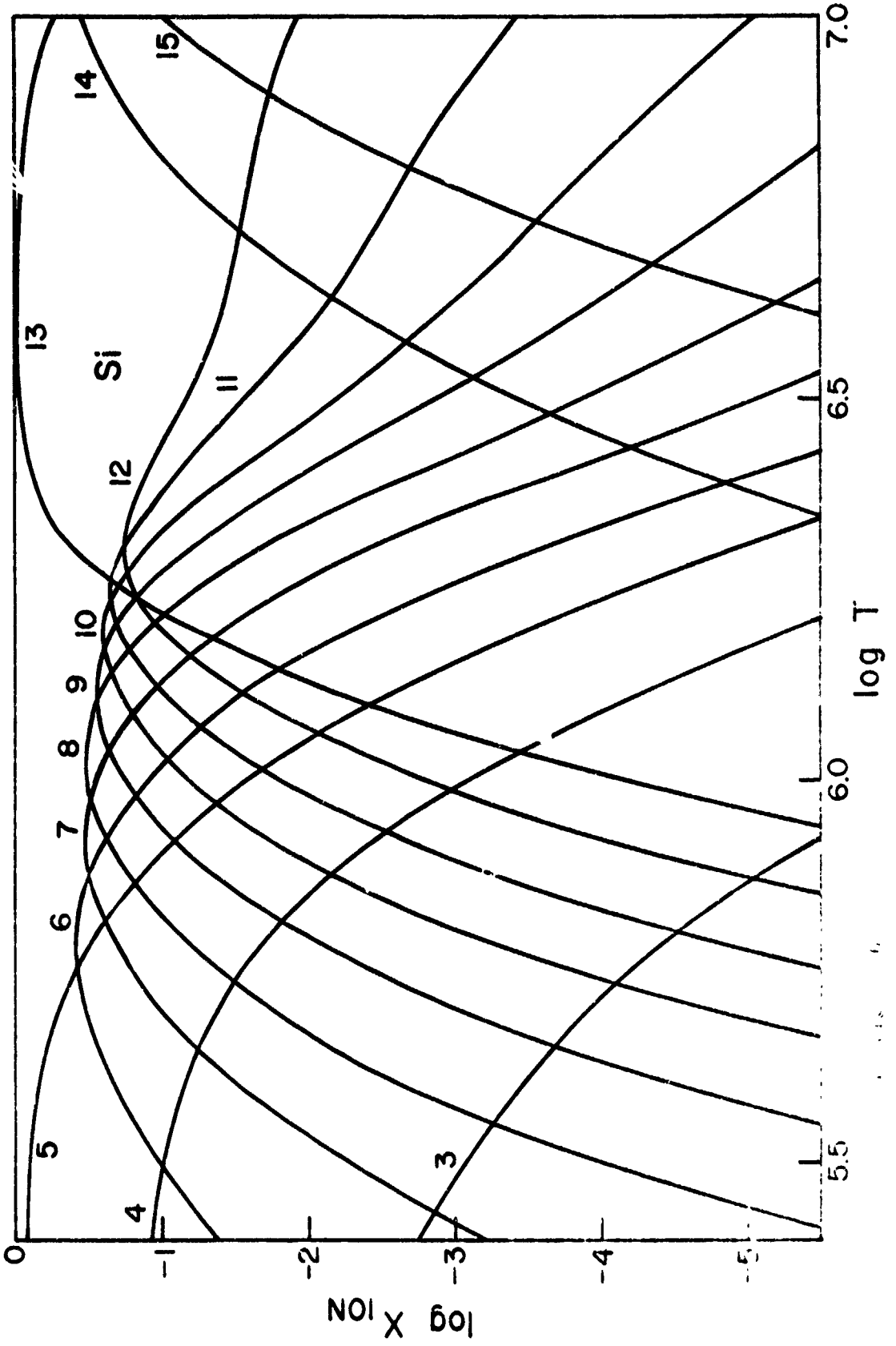
Si
13
14
15
12
11
10
9
8
7
6
5
4
3
0
-1
-2
-3
-4
-5
5.5
6.0
6.5
7.0
log T
log X ION

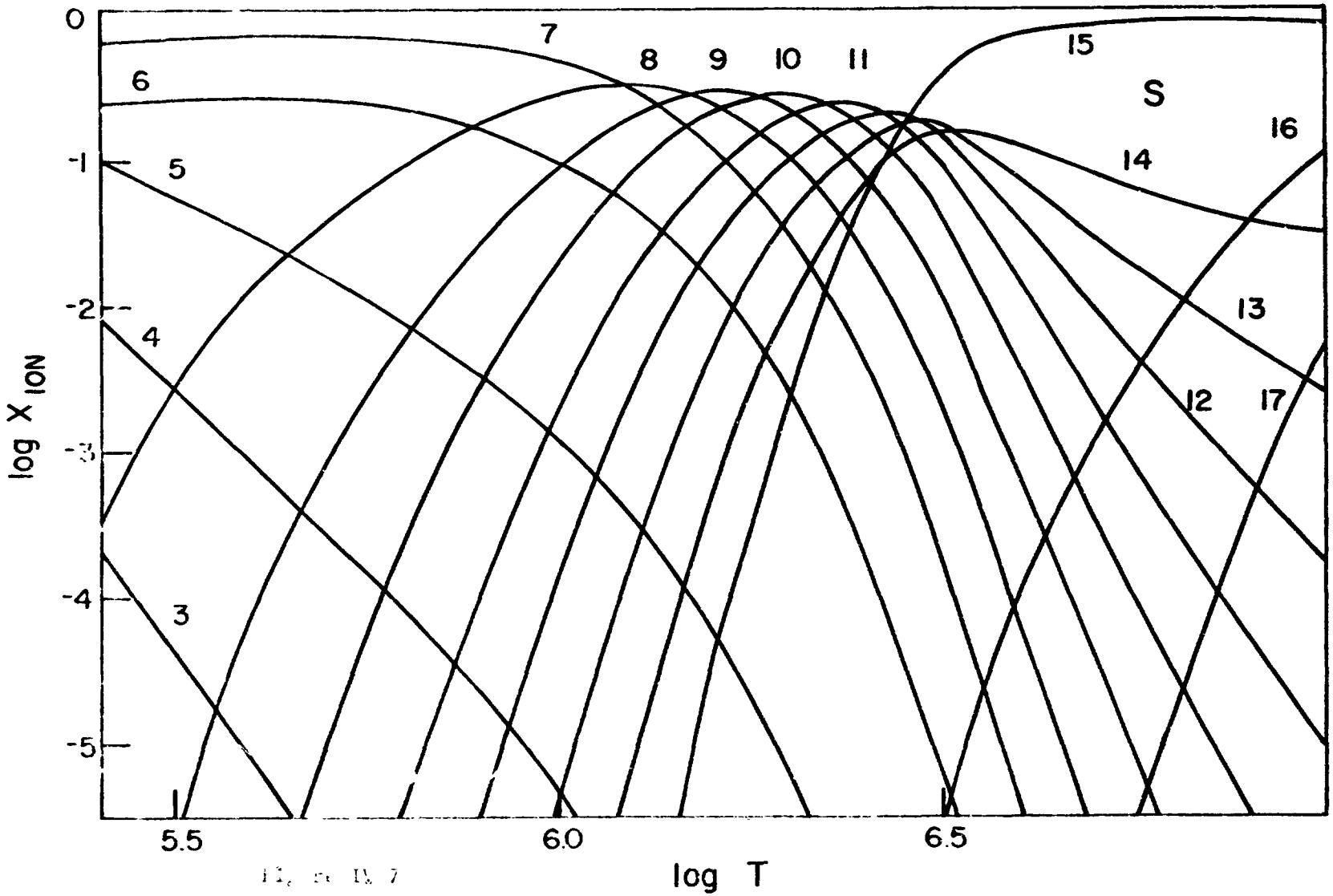

Fig. 8. IV. 7

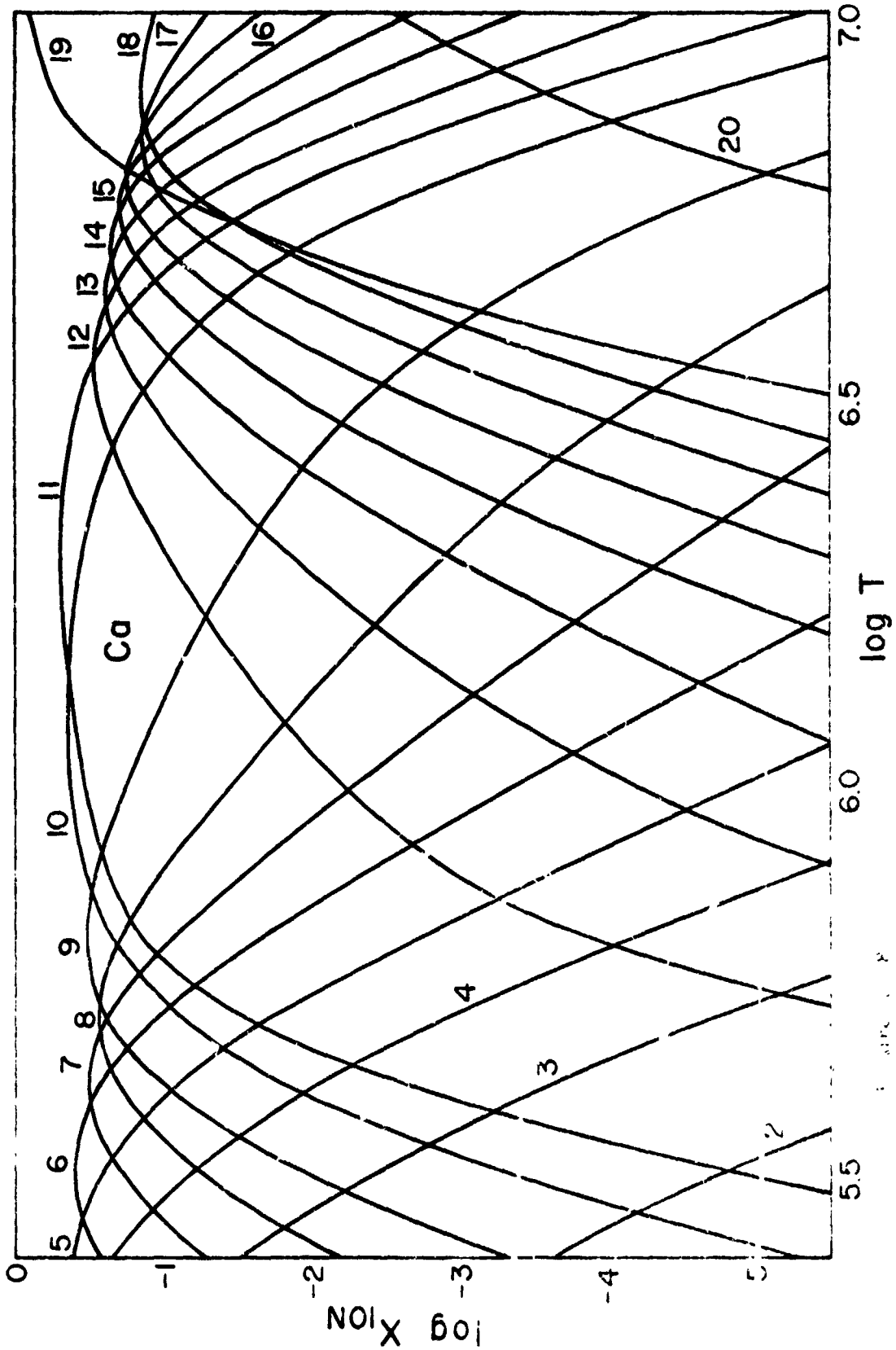
Ca
log T
log X_{ION}
7.0
6.5
6.0
5.5
0
-1
-2
-3
-4
5
6
7
8
9
10
11
12
13
14
15
16
17
18
19
20
4
3
2

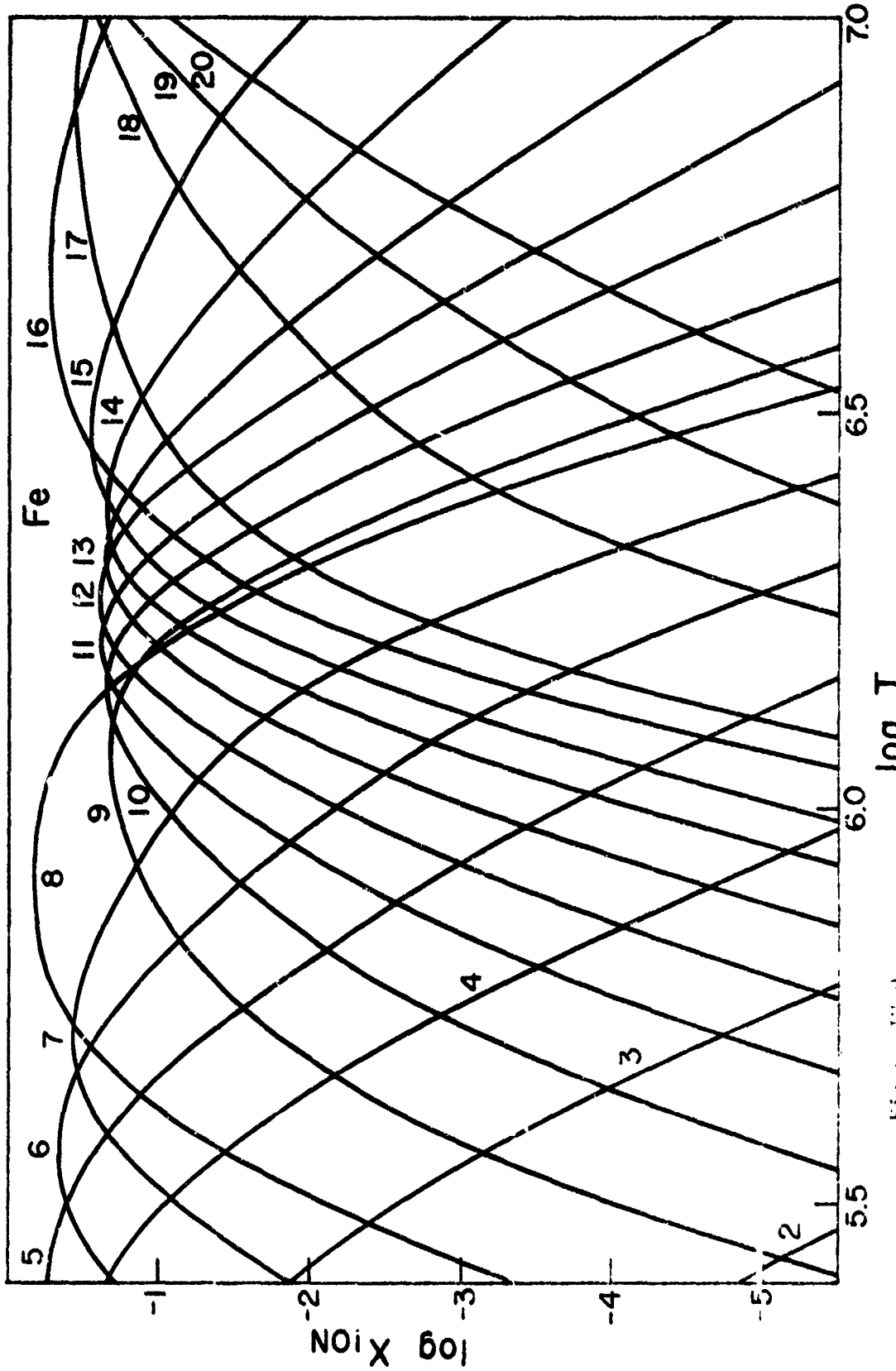
Fe
log X_{ION}
log T
-1
-2
-3
-4
-5
5.5
6.0
6.5
7.0
1
2
3
4
5
6
7
8
9
10
11
12
13
14
15
16
17
18
19
20

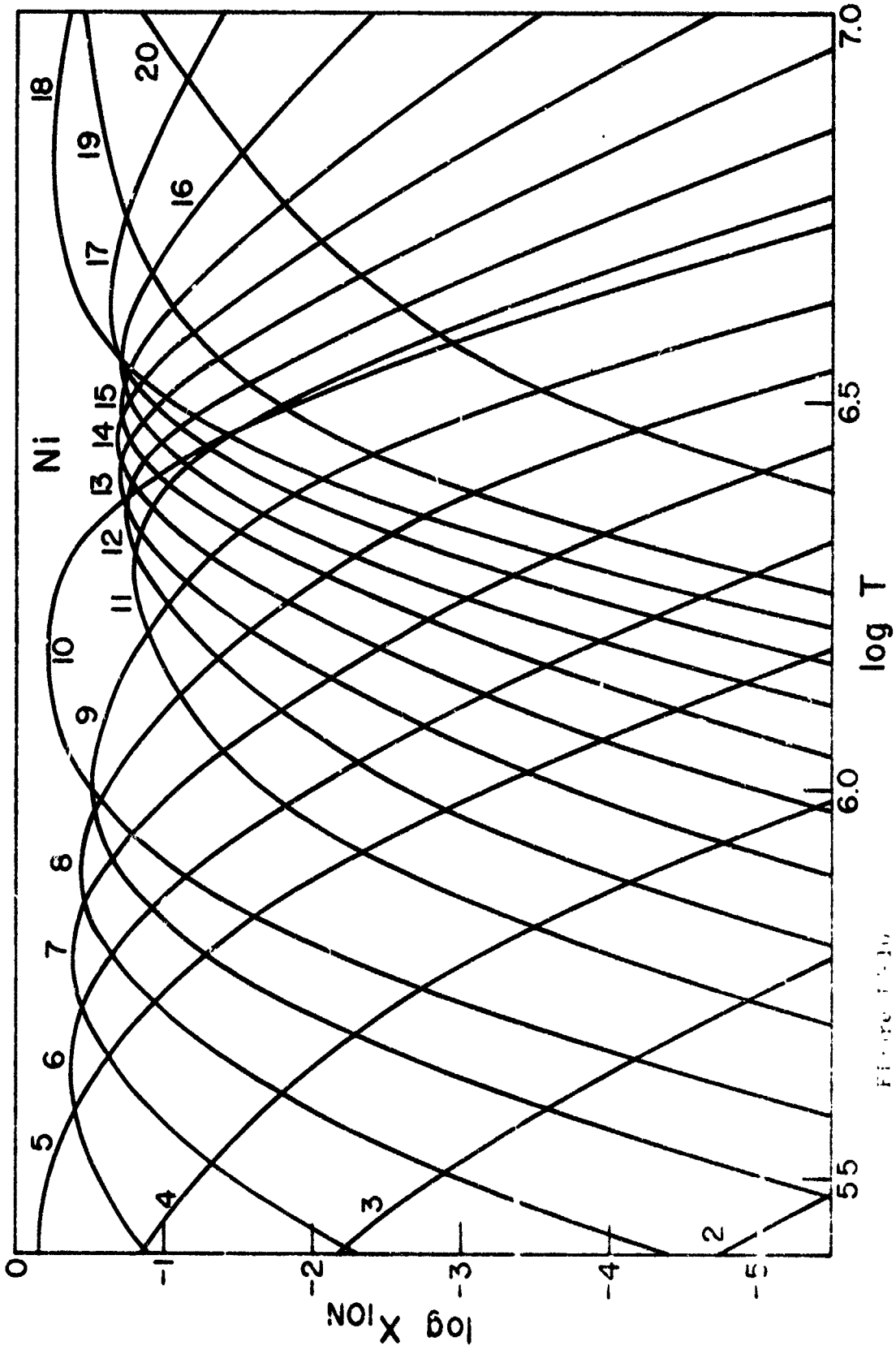
Ni
18
19
20
17
16
15
14
13
12
11
10
9
8
7
6
5
4
3
2
0
-1
-2
-3
-4
-5
5.5
6.0
6.5
7.0
log T
log X ION

Figures IV-11 to IV-13.

Ionization curves of Si XII, Fe XIV, and Fe XVI respectively, from the present calculations, and from calculations by Jordan (1967), and Allen and Dupree (1967).

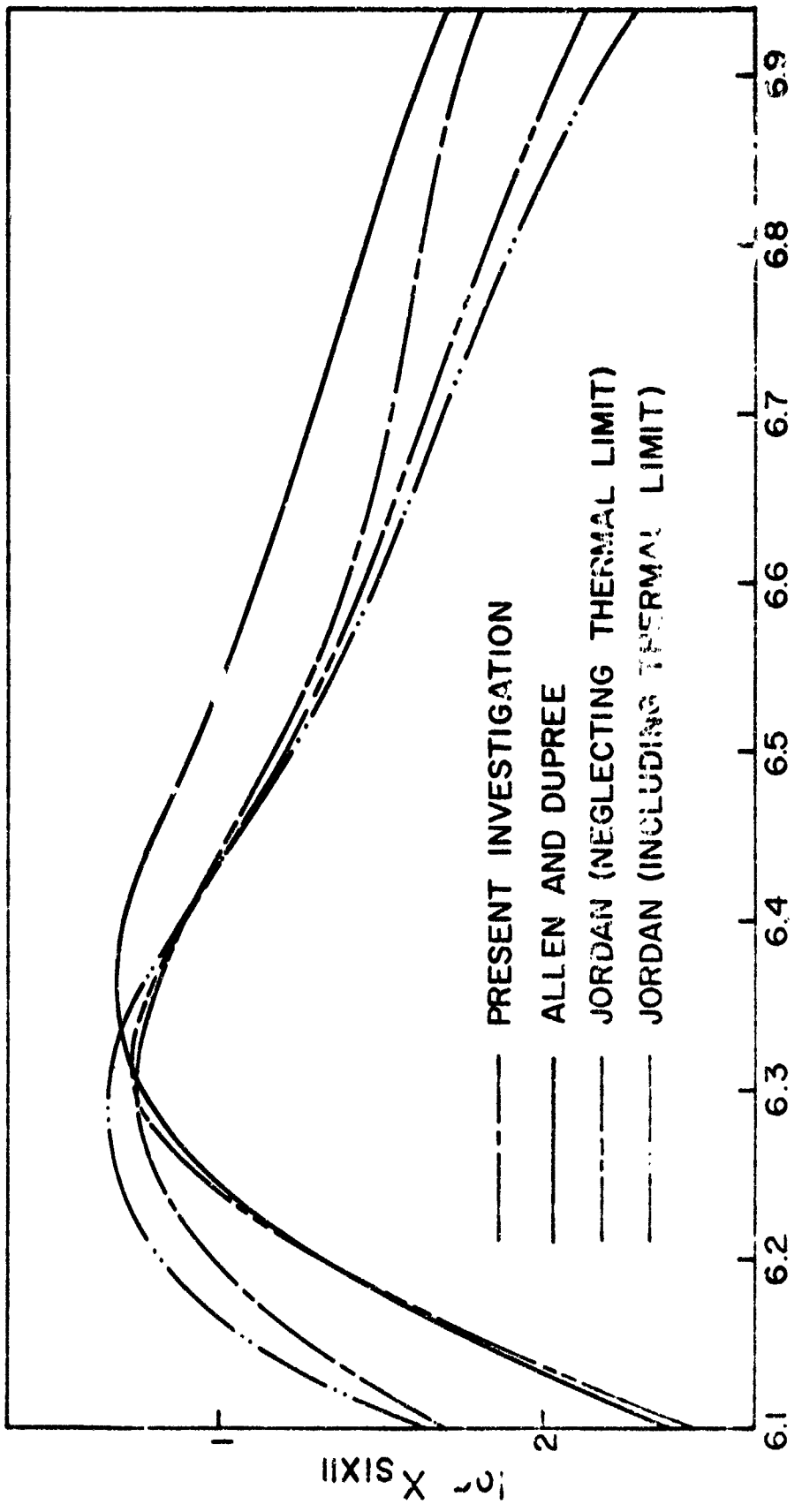
PRESENT INVESTIGATION
ALLEN AND DUPREE
JORDAN (NEGLECTING THERMAL LIMIT)
JORDAN (INCLUDING THERMAL LIMIT)
log T
6.1
6.2
6.3
6.4
6.5
6.6
6.7
6.8
6.9
1
2

Figure IV-11

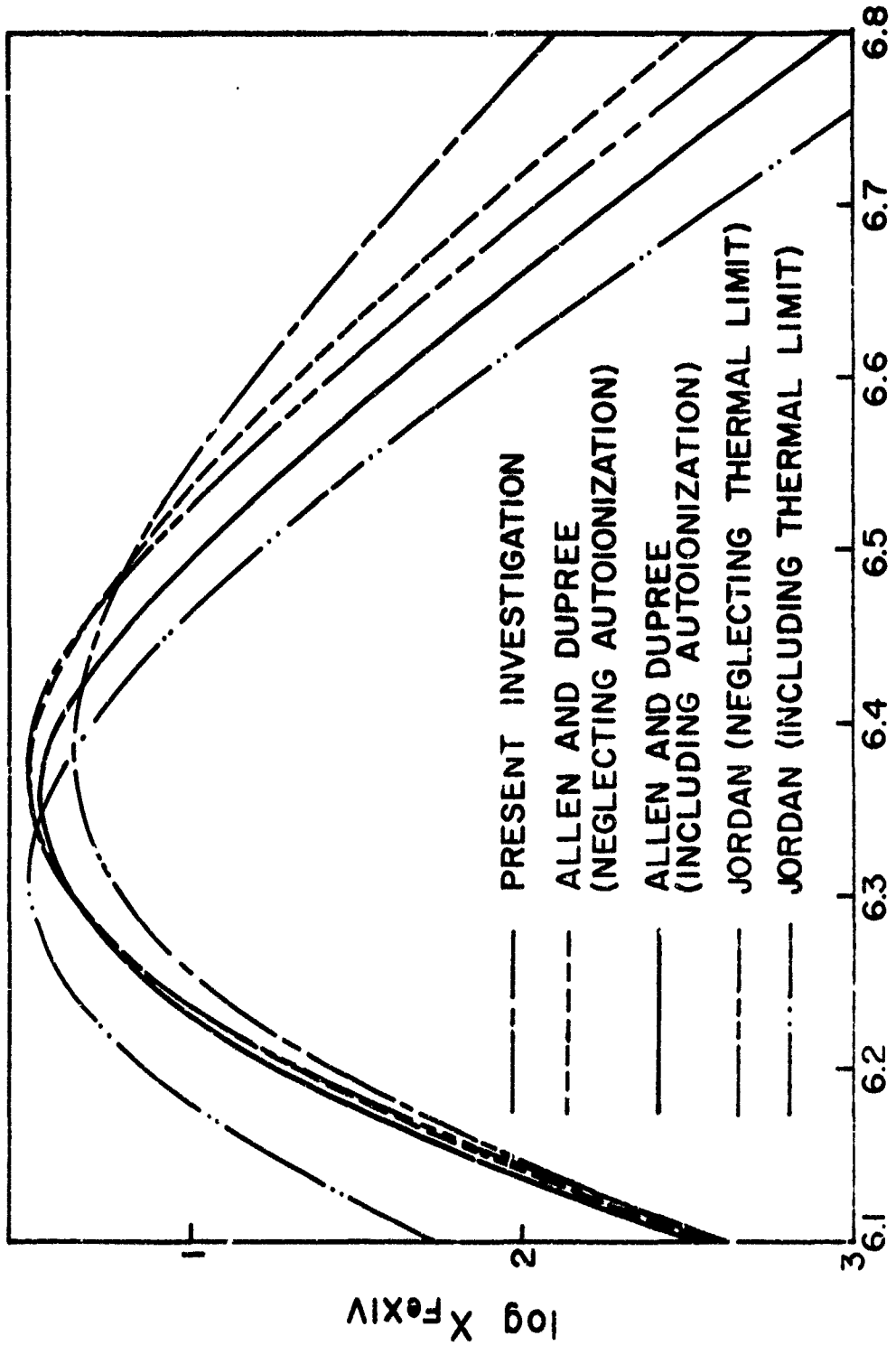
log χ_{FeXIV}
1
2
3
6.1
6.2
6.3
6.4
6.5
6.6
6.7
6.8
log T
PRESENT INVESTIGATION
ALLEN AND DUPREE (NEGLECTING AUTOIONIZATION)
ALLEN AND DUPREE (INCLUDING AUTOIONIZATION)
JORDAN (NEGLECTING THERMAL LIMIT)
JORDAN (INCLUDING THERMAL LIMIT)

Figure IV-12

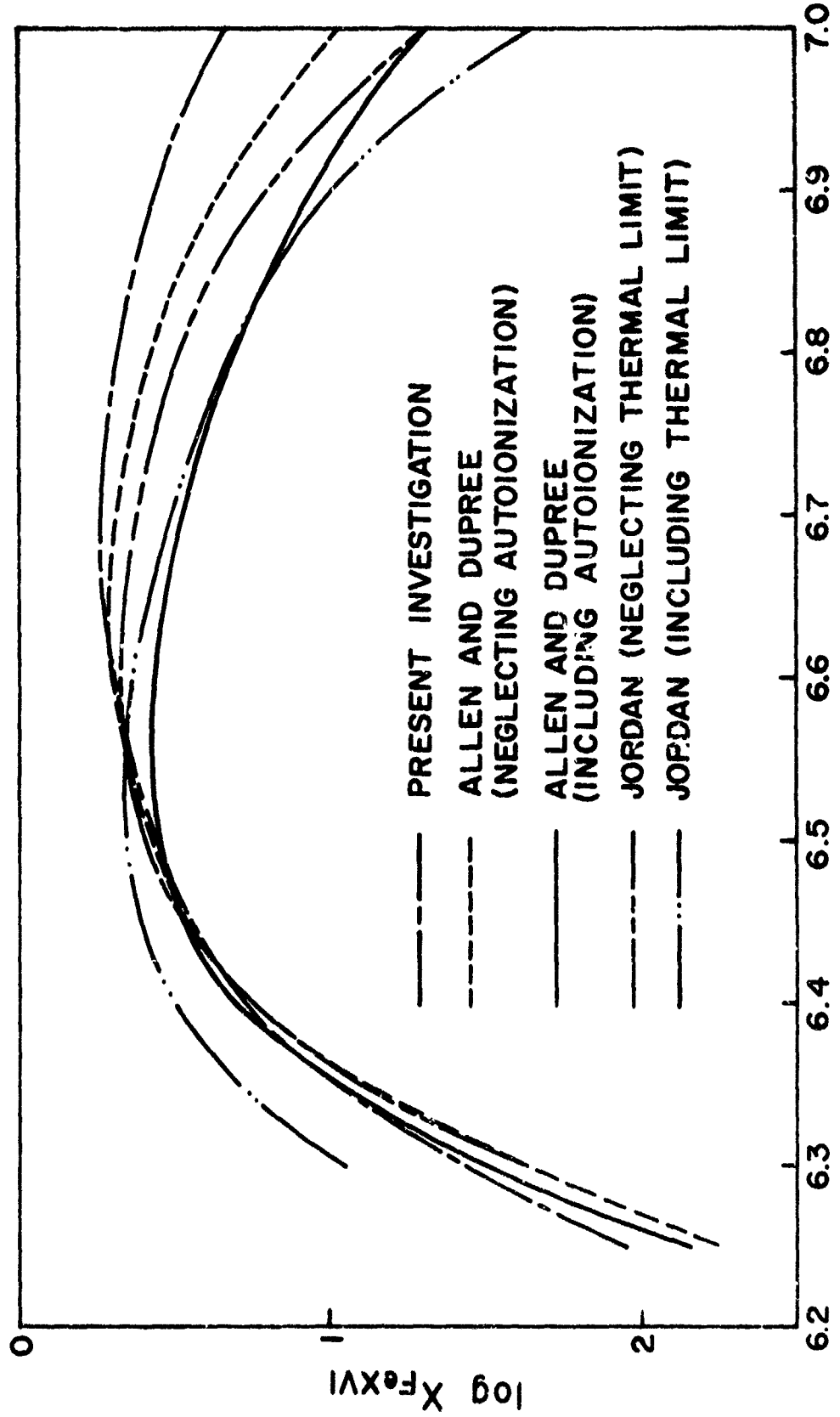
log $X_{Fe\,XVI}$
0
1
2
6.2
6.3
6.4
6.5
6.6
6.7
6.8
6.9
7.0
log T
PRESENT INVESTIGATION
ALLEN AND DUPREE (NEGLECTING AUTOIONIZATION)
ALLEN AND DUPREE (INCLUDING AUTOIONIZATION)
JORDAN (NEGLECTING THERMAL LIMIT)
JORDAN (INCLUDING THERMAL LIMIT)

Figure IV 13

CHAPTER V

EMISSION LINES IN THE EXTREME ULTRAVIOLET

A. General Remarks

Since the emission lines in the extreme ultraviolet arise from permitted transitions, the very low coronal densities imply that the chance of an ion suffering a collision with an electron while in an excited state is very small. Thus every ion in a permitted (non-metastable) excited state will have time to radiate. The problem of predicting how an optically thin sample of the coronal gas will radiate in a given line thus reduces to one of calculating the rate of population of the upper level of the line, if we assume that the composition and state of the gas are known.

Once a photon is created, we must consider the possibility of its being absorbed and re-radiated in a different direction. This process, called resonance scattering, results in no net loss of energy in the radiation field. However, a sufficient number of scatterings before the photon leaves the corona may result in one of the absorbing ions being de-excited by a collision with an electron. The photon is then destroyed, and its energy is returned to the thermal energy reservoir of the gas. This will happen under coronal conditions if optical depths approach a value of 10^4 (Ivanov-Kholodnyi and Nikolskii 1961). This situation never occurs in the corona.

Therefore, optical depth considerations become unnecessary if one merely wishes to consider the total amount of emission from the entire solar disk. A study of the resolved solar disk in the EUV lines, however, requires knowledge of whether the optical depth in the lines is less than or greater than unity, since even if all radiation may ultimately excape, appreciable scattering destroys information of where the photons originated.

The absorption coefficient per ion at the center of a line is given by

$$\alpha_o = \frac{\pi^{\frac{1}{2}} e^2}{m c} \frac{1}{\Delta\nu} f \qquad (1)$$

and if we assume that the line broadening is purely thermal this becomes

$$\alpha_o = 9.03 \times 10^{-15} f \lambda \left(\frac{\mu}{T}\right)^{\frac{1}{2}} \qquad (2)$$

(λ in Angstroms, μ in atomic mass units)

Here f is the absorption oscillator strength of the line, and μ is the atomic weight. In the case of the Fe XVI line at 335A, the strongest line used in the present investigation for study of the structure of coronal features, α_o 2.9×10^{-15}. An ion density of about 5×10^4 cm^{-3}, and a path length of 5×10^9 cm, which are close to the maximum values encountered later, give an optical depth of about 0.7. Thus some scattering may occur in the denser regions in the strongest lines, but the effect should not seriously obscure the feature, and we are justified in treating it as being optically thin.

B. Excitation Mechanisms

In principle a coronal ion may be excited by two mechanisms if we assume an optically thin gas. The ion may suffer a collision by an electron resulting in an excitation, or the excited ion may be formed by a recombination from the next higher stage of ionization plus a cascade to the excited state of interest. The rate coefficient of the former process can be represented reasonably well by an expression derived by Van Regemorter (1962)

$$C_{ij} = \frac{1.7 \times 10^{-3}}{W_{ij} T^{\frac{1}{2}}} f_{ij} e^{-y} P(y) \qquad (3)$$

$$y = \frac{11605 W_{ij}}{T}$$

where f_{ij} is the oscillator strength of the transition $i \rightarrow j$, W is the excitation potential in electron volts, and P is a Gaunt factor averaged over a Maxwellian electron-velocity distribution. It is possible (Pottasch 1964, Jordan 1966b) that the expression for P as given by Van Regemorter may be low by a factor of 1.5 to 2. Typical values are of order unity.

We may easily estimate the relative importance of radiative recombination plus cascade as compared with collisional excitation in populating the upper level of a resonance line. The collisional ionization rate, $N_e N_i q_{i,i+1}$ must, in secular equilibrium, equal the recombination rate $N_e N_{i+1} \alpha^{tot}_{i+1,i}$. We wish to compare the latter with the collisional excitation rate, $N_e N_i C_{1j}$. Because the collisional ionization rate coefficient is similar in its mathematical

form to the rate coefficient for collisional excitation, and since the ratio of excitation and ionization rates is independent of N_e and N_i, it is convenient to use $N_e N_i q_{i,i+1}$ in place of $N_e N_{i+1} \alpha^{tot}_{i+1,i}$ as a measure of the recombination rate. This will serve as an upper limit to the rate of population of an upper level of a line by cascade. If, for the moment, we consider all excitations as arising from the ground state, and assume that P, ζ, and f are all of order unity, then division of (3) by IV-(7) gives the following result for the ratio of the rates of the two processes:

$$\frac{C_{1j}}{q_{i,i+1}} = 8.5 \times 10^4 \frac{\chi^2_{i,i+1}}{W_{1j} T} \exp\left(-11605(W_{1j} - \chi_{i,i+1})/T\right) \quad (4)$$

In the extreme ultraviolet spectrum from 171A to about 700A the corresponding excitation energies range from 17.7 to 72.6 electron volts. The ionization potentials of the ions giving rise to the lines range from 208 to 523 eV. Let us consider the possibility of making the ratio in eq. (4) as small as possible, in order to favor recombination as a means of populating an excited level. We may take in the exponent χ small, W large, and T large; and in the rest of the expression χ small, W large, and T small. (This last assumption on T contradicts the first, but this can only strengthen the argument). Substitution yields $C/q \approx 5$, with the exponential near unity. The actual ratios will be a good deal larger than this since our assumptions are to a large extent exclusive of one another. Thus we may neglect any consideration of

recombination as a mechanism contributing to resonance line emission. A further justification for this is seen from the fact that all direct excitations result in an emission of a photon of the line in question, but only a part of the total recombination considered in the above argument will cascade via any given line.

There remains the question of whether or not excitation of a resonance line may occur by a collision to a higher state plus a cascade. From eq. IV-(3), it is evident that the oscillator strength, $f_{nn'}$, for an hydrogenic ion varies approximately as n'^{-3} for fixed n. Although oscillator strengths of many transitions are poorly known, as an order-of-magnitude estimate this statement is valid also for many-electron configurations. The collisional excitation rates therefore may be expected to decrease with increasing energy due to the decrease in f-values, and also the decrease in the quantity $\exp(-11605W_{ij}/T)W_{ij}$. From these semi-quantitative arguments we conclude that direct excitation is considerably more important in populating the upper level of a resonance line than is indirect excitation plus cascade. The fact that very few lines which do not connect with the ground term are observed (Wiuing 1966) gives observational support to the assumption that direct excitation is the dominant process.

C. Emissivity of the Coronal Gas

The rate coefficient of population of a permitted excited level by direct collisional excitation is given by Eq. (3). If we assume that this is the dominant process, and that all ions so excited will

radiate a photon of energy $h\nu$, then the emissivity of the gas in that particular line is

$$E = C_{lj} N_{ion} N_e h\nu \text{ erg cm}^{-3} \text{ sec}^{-1} \quad (5)$$

If we let $A_{e\ell} = N_{e\ell}/N_H$, the relative concentration of the element with respect to hydrogen, and X_{ion} = the fraction of the element in the stage of ionization giving rise to the line, then for a hydrogen density equal to 0.8 times the electron density, (5) becomes

$$E = 0.8 X_{ion} A_{e\ell} C_{lj} N_e^2 h\nu$$

$$= 2.2 \times 10^{-15} N_e^2 T^{-\frac{1}{2}} X_{ion} A_{e\ell} f_{lj} P(y) e^{-y} \quad (6)$$

$$\text{erg cm}^{-3} \text{ sec}^{-1}$$

Both the emissivity and ionization curves clearly show a feature which can in principle severely complicate any analysis of coronal structure from a study of line emission. The ions with closed shells, because of the large difference between the energies needed to create and destroy them can exist over an extremely large temperature range. Although they are difficult to excite, and by themselves emit almost no observable lines in the EUV wavelengths, they provide a tremendous reservoir of ions from which neighboring stages of ionization may be formed. Thus the lithium-type and sodium-type ions experience a much slower decrease in their abundances with increasing temperatures than would otherwise be the case. Good examples of this can be seen for Si XII and Fe XVI.

In the case of Fe XV, the effect is still present even two stages of ionization removed from a closed shell.

As a result of this state of affairs, significant emission in a line can occur at temperatures far removed from the temperature of maximum abundance. As an example, consider Si XII which maximizes at 2×10^6 °K. At 8×10^6 °K its emissivity has dropped to 0.1 of its maximum. Thus, if one considers a non-homogeneous gas in which density correlates positively with temperature, an increase in density by only a factor of $10^{\frac{1}{2}}$ will completely compensate for the temperature increase, and a larger rate of increase of density with temperature will shift the temperatures of maximum emission quite rapidly toward larger values, and greatly increase the range of temperatures at which significant emission occurs. The conclusion is that a strong tendency for high temperatures to be associated with high densities in the coronal material would result in a strengthening of the lines from the lithium- and sodium-like ions, as compared with other ions whose temperatures of maximum abundance are the same. This effect should be most noticeable in the hot, dense regions of an enhancement.

D. Extension to Multiplets

The preceding discussion applies directly to transitions which arise from an unsplit ground term. If the ground term is split, two modifications must be made in the argument. First, the argument in favor of treating the gas as if it were optically thin is no longer strictly appropriate since an excitation by a photon from one level of the ground term may result in radiation to a different level.

The second alteration produced by the split ground term is that we are now forced to make an assumption concerning the relative populations of the levels within the term in order to predict the line intensities. The simplest assumption would be that the density is sufficient to populate the levels in equilibrium with the kinetic temperature. This is more likely to be true in the dense ennancements than in the quiet corona. Since the term splitting is much less than kT, we may write for a given level i

$$N_i = \frac{g_i}{g_{term}} \tag{7}$$

where N_i is the relative population of the level in question.

From eq (3), the rate of excitation from level i to level j by collision is proportional to the oscillator strength f_{ij}. The rate of population of any given upper level j by all the lower levels i will be proportional to

$$\frac{\sum_{i<j} f_{ij}\, g_i}{g_{term}} = \sum_{i<j} N_i\, f_{ij} \tag{8}$$

and the rate of depopulation, once the excitation has occurred will be proportional to

$$\frac{A_{jk}}{\sum_{i<j} A_{ji}} = \frac{g_k\, f_{kj}}{\sum_{i<j} g_i\, f_{ij}} \tag{9}$$

If we multiply expression (8) by (9) and make use of the fact that the f-value times the statistical weight for a line is the same

for emission and absorption, we obtain an expression that replaces f_{lj} in eq. (6). Thus

$$f_{eff,jk} = \frac{g_j f_{jk}}{g_{term}} \qquad (10)$$

The intensity of each line is therefore reduced in proportion to the relative population of its lower level compared to the entire population of the lower term.

It must be remembered that eq. (10) is definitely a limiting case in the sense described above, and is also an approximation in that the summation $\sum fg$ in (8) only represents an approximate expression of the collision rates, whereas the same summation in (9) is exact, if the lines in the multiplet are close in wavelength. The result of a strong underpopulation of the upper levels of the ground term would be a marked reduction in the strengths of lines whose upper levels cannot be populated by collisions from the ground level, relative to the total multiplet strength.

The preceding discussion does not consider the possibility of excitation of a forbidden level since the excitation cross sections are very poorly known. Recent work by Bely (1966a, 1966b) shows that these are in some cases quite large and may give rise to strong non-resonance line emission.

PART THREE -- A STUDY OF THE STRUCTURE OF EUV ENHANCEMENTS

CHAPTER VI

EMISSION WITHIN THE LIMB ENHANCEMENT AS A FUNCTION OF TEMPERATURE

A. General Remarks -- Mathematical Difficulties

The emissivity of the coronal gas as given by eq. V-(6) may be integrated over a line of sight to give the surface brightness of the feature in question. If the emissivity, E, is taken as a function of position, x, along the line of sight, then the brightness, I, in erg cm^{-2} sec^{-1} radiated in all directions is given by

$$I = \int E(x)\, dx \qquad (1)$$

Substitution of V-(6) into (1) gives a general expression for I in terms of the ionization and excitation conditions of the gas:

$$I = 2.2 \times 10^{-15} A_{e\ell} f_{eff} \int P(y) e^{-y} X_{ion}(T) T^{-\frac{1}{2}} N_e^2\, ax \qquad (2)$$

Eq. (2), although exact insofar as the excitation rates of the emitting ions are known, is not in a particularly useful form for interpreting the observed brightness of a feature in various lines. We therefore proceed to transform the integral over path length into an integral over temperature, in a manner similar to

what Athay (1966) has done. Let us make the following substitutions in eq. (2):

$$G(T) = P(y)e^{-y} X_{ion}(T)\, T^{-\frac{1}{2}} \tag{3}$$

$$dx = \frac{dx}{d\ \log T}\, d\ \log T \tag{4}$$

and we find, upon substituting (3) and (4) into (2):

$$I = 2.2 \times 10^{-15} A_{e\ell}\, f_{eff} \int G(T)\, N_e^2 \frac{dx}{d\ \log T}\, d\ \log T \tag{5}$$

The quantity (dx/d log T) as a function of position may pass through many singular points along the line of sight as local maxima and minima of temperature are traversed. In temperature space, however, (dx/d log T) is no longer interpreted as an inverse logarithmic temperature gradient, but rather corresponds physically to the <u>total</u> increment of path length, dx, along the line of sight, per unit increment in log T as a function of temperature. Since log T is the independent variable, (dx/d log T) $\to \infty$ implies that $dx \to \infty$. This is ruled out by the geometric limitations of the problem.

The rather inelegant use of a common logarithm as a variable of integration in eq. (5) will perhaps be justified by its convenience as a physical quantity. We make two further definitions in the following analysis for the purpose of simplifying our notation:

$$\theta = \log T \qquad (T \text{ in } ^\circ K) \tag{6}$$

$$\phi(\theta) = N_e^2 \frac{dx}{d \log T} = N_e^2 \frac{dx}{d\theta} \qquad (7)$$

In writing eq. (7), we have tacitly assumed that we can express ϕ as a point function of temperature. In a very simple structure this may be obviously true, but in a complex structure with many streamers representing strong density and temperature fluctuations, eq. (7) must be more carefully defined.

Consider as an example a case in which T is a monotone function of the position along the line of sight, x. Then we may easily write $N_e^2 = N_e^2(T)$ and $x = x(T)$, and the interpretation of (7) remains completely unambiguous. If, however, given values of T are encountered many times along the line of sight, then N_e^2 and x will not be single-valued functions of T. The definition of $\phi(\theta)$ will then be arrived at in the following manner.

We may divide the line of sight up into intervals, i, within each of which the condition of single-valuedness described above is satisfied. The boundaries of the intervals are specified by the following consideration A boundary will occur whenever the temperature reaches a local extremum. Both position and density will then be single valued functions of temperature within each interval. Next, consider a temperature, T. Our method of subdividing the line of sight assures us that within each interval, i, the value of T, and the corresponding value of θ may be realized either once or not at all. Each time T occurs, it will have associated with it a value of $(N_e^2)_{i,\theta}$ and a value of $(dx/d\theta)_{i,\theta}$ for the particular interval, i. We then define $\phi(\theta)$ in the following fashion:

$$\phi(\theta) = \sum_i (N_e^2)_{i,\theta} \left|dx/d\theta\right|_{i,\theta} \qquad (8)$$

When defined in this manner, the quantity $\phi(\theta)$ has the following physical interpretation: Any set of lines, j, whose emission characteristics differ only in the temperatures, θ_j, at which the lines occur, and whose emissivity curves approximate a δ-function about these temperatures, will have relative brightnesses of $I_j \propto \phi(\theta_j)$. The absolute value of the derivative in (8) assures us that the net effect of increasing and decreasing temperature gradients along the line of light will be cumulative.

Having thus defined $\phi(\theta)$ in a suitable fashion, we may rewrite (5) in the following manner for a line denoted by j:

$$I_j = 2.2 \times 10^{-15} A_{e\ell} f_{eff,j} \int G_j(\theta)\, \phi(\theta)\, d\theta \qquad (9)$$

and define an average value of ϕ in the following manner:

$$\langle\phi\rangle_j \equiv \frac{\int G_j(\theta)\, \phi(\theta)\, d\theta}{\int G_j(\theta)\, d\theta} \qquad (10)$$

Thus far, the development has consisted only of physical statements and mathematical definitions, with no description of how observed values of I_j for the various lines may be used to obtain empirically the structural function, $\phi(\theta)$. Although $\phi(\theta)$ is well defined, its interpretation in terms of the observed brightnesses of the lines made use of highly idealized assumptions concerning

the emission properties of the lines. In practice, the emissivity curves are not sufficiently narrow to be considered δ-functions, and also exhibit a significant variety of shapes as well as magnitudes. We can, however, define a quantity, $\langle\phi\rangle_{j,\,meas.}$, in terms of the measured brightness of line j, $I_{j,meas.}$, as follows:

$$\langle\phi\rangle_{j,meas.} = \frac{I_{j,meas.}}{2.2 \times 10^{-15} A_{e\ell} f_{eff,j} \int G_j(\theta)\, d\theta} \qquad (11)$$

We may then compute $\langle\phi\rangle_{j,\,meas.}$ for each line for which reliable photometric measurements of $I_{j,\,meas.}$ are obtainable, and plot these values of $\langle\phi\rangle_{j,\,meas.}$ against θ. The assignment of a value of θ_j is somewhat arbitrary; we shall define θ_j as the centroid of the function $G_j(\theta)$. After evaluating the uncertainties in the abundances of the elements, $A_{e\ell}$, in the next section, we shall calculate values of $\langle\phi\rangle_{j,\,meas.}$ from the observed lines, and discuss how accurately a plot of the points $(\theta_j, \langle\phi\rangle_{j,\,meas.})$ would be expected to represent the function $\phi(\theta)$.

B. Relative Abundances

In addition to the manner in which emission of a given ion varies with temperature, knowledge of the relative abundance of the parent element, $A_{e\ell}$, and the effective f-value of the line in question is necessary before we can infer the amount of radiating material within an enhancement from its brightness profile. The f-values of most of the important EUV transitions are now reasonably well known and are tabulated by Pottasch (1967) in his most recent determination of element abundances from coronal EUV lines.

The question of element abundances raises more serious uncertainties, particularly since there exist unexplained discrepancies between measurements of photospheric and coronal abundances. The latter have been calculated by Pottasch in his several papers, using an equation similar to (2) with the temperature-dependent factors taken outside the integral and replaced by the following average:

$$\langle G(T) \rangle \equiv 0.7\, P(y) e^{-y}\, X_{ion}(T)\, T^{-\frac{1}{2}} \Big|_{T=T_{max}} \tag{12}$$

and therefore

$$A_{e\ell} \int_R N_e^2\, dx = \frac{I}{1.1 \times 10^{-15} \langle G(T) \rangle\, f_{eff}} \tag{13}$$

The right-hand side of (13) is completely determined from theory and from observations. Note the difference of a factor of two between (13) and (2). This difference arises from the fact that Pottasch considers the emission from the total sum emitted in all directions, of which half is radiated toward the photosphere and is never observed.

Pottasch assumes that the quantity $\int_R N_e^2\, dx$, where R is the region over which the line in question effectively emits, is a function of temperature only. He then considers the quantities $A_{e\ell}$, which represent the elemental abundances, as unknown parameters which may be adjusted such that a plot of $\int_R N_e^2\, dx$ versus temperature from all available lines shows a minimum amount of scatter. The resulting abundances, shown in Table VI-1 show the most recent values

of Pottasch (1967) as compared with the photospheric abundances of Goldberg, Müller, and Aller (1960). Both sets of abundances are expressed with that of silicon set at 100 as a standard. On the basis of a comparison of the radio solar emission with that of the emission lines, Pottasch had concluded that $A_{Si} \approx 10^{-4}$.

Pottasch's most recent analysis (1967) employs data from both photoelectric and photographic observations of the solar disk as a whole (Hinteregger, Hall, and Schweizer 1964; Austin, Purcell, Tousey, and Widing 1966; Blake, Chubb, Friedman, and Unzicker 1965; Hall, Schweizer, and Hinteregger 1965; and Hall, Schweizer, Heroux, and Hinteregger 1965). These data are undoubtedly more accurate than the values of the surface brightness I measured photometrically from the spectroheliograms, which are given in Table VI-2. Because of this, I felt it most prudent to make no initial assumptions regarding the abundances, or to attempt to re-derive them, but rather to investigate how the assumption of each set of abundances in turn will affect the conclusions regarding the structure of the enhancements, and to evaluate each set on the basis of self-consistency of the results.

C. Computations of $\phi(\theta)$

Table VI-2 lists the values of the maximum brightnesses of Features 3 and 4 as measured photometrically from the spectroheliograms in the various lines. The absence of a measurement of the Fe XIV 265A line in Feature 4 is due to overlapping with the He II 304A disk image. The emission from Fe XV at 284A also overlaps the

He II 304A disk, but the line is strong enough to yield a reliable measurement of its maximum brightness in spite of the high background.

The Ni XVIII lines are conspicuous by their absence. Since we observe strong emission from the lines of Fe XVI at 335A and 361A, we should also expect to see emission from Ni XVIII fairly easily at 322A, unless a rapid decrease in $\phi(0)$ occurs somewhere between the temperatures characteristic of the two ions. The stronger Ni XVIII line at 293A overlaps the He II disk. Observations of some of the fainter lines in this wavelength region, whose intensities could not be determined reliably but could be estimated theoretically, indicate that we may place an upper limit of I for Ni XVIII 322A at around 4×10^2 erg cm^{-2} sec^{-1}, or about 0.01 that of its corresponding line of Fe XVI at 361A.

Examination of Table VI-2 shows that there is very little difference between the brightnesses of Features 3 and 4 in the various lines as compared with the differences in the brightnesses among the lines themselves. The one exception to this is the 465A line of Ne VII which shows up much more strongly from Feature 3 than from Feature 4. The spectroheliograph picture of the Ne VII line shows at the position of Feature 3 a small, well-defined bright spot on the disk that has no counterpart in Feature 4. The coronal emission, on the other hand, appears to be very similar for the two features, and is measureable quite unambiguously from Feature 4 in all given lines. I shall therefore consider only Feature 4 for a structural analysis. To be sure, the marked limb brightening of

the sun in Ne VII must be subtracted from the photometric traces of Feature 4, but the limb appears distinctly enough in the tracings that no ambiguity arises.

Figures VI-1 and VI-2 show the points $(\theta_j, \langle\phi\rangle_{j,meas.})$ calculated from the values of $I_{j,\,meas.}$ listed in Table VI-2, a graphical integration of the $G_j(\theta)$, for the relative abundances of Goldberg et. al. (1960) and Pottasch (1967) respectively. The f-values are the same as used by Pottasch (1967) in his most recent analysis of coronal element abundances, and represent a compilation of the work of several authors. The error bars included represent an estimate of the combined uncertainties of excitation and ionization theory, f-values, and errors arising from uncertainties in the photometry. In the case of Ni XVIII, since the line at 322A is not actually observed, the points plotted represent an upper limit. Although Goldberg et. al. (1960) give no abundance results for neon, the value obtained by Pottasch (1967) is consistent in general with values obtained by other investigators, and no serious uncertainty in the neon abundance is evident at present. Therefore, I include the Pottasch value of a_{Ne} on both plots.

Both sets of abundances allow a reasonable curve $\phi(\theta)$ to be fitted to the data, and both curves show the same general character. A rapid rise in the emitting ability of the features occurs from temperatures of about 5×10^5 °K to about 2.5×10^6 °K. The curves then begin to flatten out and reach a maximum around 3×10^6 °K, which is followed by a rapid decrease at higher temperatures.

As I have drawn it, the $\phi(\theta)$ curve obtained from the Goldberg abundances shows a much steeper initial rise and a larger maximum than does the Pottasch curve. It may be argued that the former curve should have been drawn to pass between the ranges of values of Fe XIV and Si XII, instead of effectively ignoring the latter. A curve thus drawn would more nearly resemble the Pottasch curve. Since the Si XII lines were made from a different exposure than any of the other lines in the same temperature region, it seemed more prudent to place faith in the Fe XIV and XV measurements to eliminate the possibility of an unknown source of systematic photometric error.

Although they allow a reasonably good curve to be fitted to the points, both sets of data produce inconsistencies that make it impossible for such a curve to pass through the error bars of all lines. As compared with Goldberg, the high Pottasch abundance of iron removes the discrepancy between Si XII and the higher ionization stages of iron, but introduces one between Fe IX and Mg IX.

D. Theoretical Uncertainties in $\phi(\theta)$

Although most of the scatter in Figures VI-1 and VI-2 is undoubtedly due to observational errors, and, to a smaller extent, to uncertainties in the ionization and excitation theories there remains an additional source of error that is non-random and arises from variations in the shapes of the emissivity curves of the ions. To illustrate the nature of this uncertainty, consider the following hypothetical example.

Assume we have two ions which have the same values of θ_j, $\int G_j(\theta)\, d\theta$, and all atomic parameters included in eq. (9). We then should require that $\langle\phi\rangle_j$ would be the same for both ions, since we are associating it with θ_j in both cases, and we wish to establish a procedure by which $\phi(\theta_j) = \langle\phi\rangle_j$ for all ions. However, eq. (10) clearly shows that we are not able to do this. If ion #1 has an emissivity curve $G_1(\theta)$ that posesses a long tail on the low temperature side, and ion #2 has a similar tail on the high temperature side, then if $\phi(\theta)$ is an increasing function of θ, $\langle\phi\rangle_2$ will be greater than $\langle\phi\rangle_1$, whereas if $\phi(\theta)$ is a decreasing function, the reverse will be true. It follows that the points plotted in Figures VI-1 and VI-2 will not yield the actual curve $\phi(\theta)$, but a curve subject to a systematic error, particularly where its slope is steepest.

We may make an approximate correction to this error, provided the changes in the curve implied by these considerations are not too severe. The following steps will outline the procedure used in making the corrections:

1. From the curve, $\phi(\theta)$, as we have drawn it, compute each $\langle\phi\rangle_j$ from eq. (10).

2. Plot each point, $(\theta_j, \langle\phi\rangle_j)$ on a graph. These points in general will not lie on the curve $\phi(\theta)$. Instead, they represent the curve we should expect to obtain by ideal measurements from a line of sight whose emission efficiency with temperature actually obeys the function, $\phi(\theta)$.

3. Since $\phi(\theta)$, as we have shown it, is actually a curve derived from observations, the corrected curve, which we denote as $\phi_{cor}(\theta)$, should be defined by points lying the same distance from $\phi(\theta)$ on a logarithmic scale as $\langle\phi\rangle_j$, but in the opposite direction.

Figures VI-3 and VI-4 repeat in solid lines the same curves $\phi(\theta)$ that were given by the data points in Figures VI-1 and VI-2, respectively. The tail of each arrow corresponds to the point $(\theta_j, \phi(\theta_j))$ for each ion, whereas the head corresponds to the point $(\theta_j, \langle\phi\rangle_j)$. The dashed curve drawn shows the curve $\phi_{cor}(\theta)$. We note that the changes appear to be relatively small over the ascending branches of the curves, but are somewhat larger over the much steeper descending branches. In addition, the point at which the maximum of $\phi_{cor}(\theta)$ occurs is shifted to 5×10^6 °K from 2.5×10^6 °K, and at temperatures above 5×10^6 °K, $\phi_{cor}(\theta)$ decreases extremely rapidly. This rapid decrease becomes all the more significant if we remember that the value of $\langle\phi\rangle_{\text{Ni XVIII, meas.}}$ is an upper limit, and that the high-temperature decrease in ϕ may actually be much steeper. We thus have rather definite evidence that strong decreases in the amount of material in the two coronal features observed occurs at around 5×10^6 °K. To support this conclusion, we note that the visible coronal lines of Ca XV, which correspond to temperatures between 5 and 6×10^6 °K are generally not observed in long-lived enhancements of the type we are discussing here. On the other hand, observations of Fe XVI in the EUV, an ion not much cooler than Ca XV, have long shown that emission from this ion depends very sensitively on the degree of normal solar activity present.

Table VI-1

Relative Abundances (Si = 100)

	Pottasch (1967)	Coldberg et. al. (1960)
C	1000	1600
N	120	300
O	500	2800
Ne	70	--
Mg	60	75
Al	4	5
Si	100	100
S	40	63
Fe	100	12
Ni	9	2.5

Table VI-2

Maximum brightness of Features 3 and 4 in the various lines.

Ion	(A)	I(erg cm^{-2} sec^{-1}) Feature 3	Feature 4
Fe IX	171	6.6×10^3	7.7×10^3
Fe XIV	211	5.0×10^4	2.0×10^4
Fe XIV	265	1.5×10^4	
Fe XV	284	1.2×10^5	6.3×10^4
Ni XVIII	322	$\lesssim 4 \times 10^2$	$\lesssim 4 \times 10^2$
Fe XVI	335	1.0×10^5	9.7×10^4
Fe XVI	361	4.9×10^4	3.8×10^4
Mg IX	368	1.1×10^4	1.3×10^4
Ne VII	465	4.9×10^4	7.2×10^3
Si XII	499	6.0×10^3	4.4×10^3
Si XII	521	2.4×10^3	1.8×10^3

Figures VI-1 and VI-2

The points $(\theta_j, \langle\phi\rangle_{j,\,meas})$ as determined from measured brightnesses, $I_{j,\,meas}$, of Feature 4 in various EUV lines. Included also are the curves $\phi(\theta)$ drawn to approximate the distribution of these points. The abundances assumed are those of Goldberg, Müller, and Aller (1960), and Pottasch (1967) respectively.

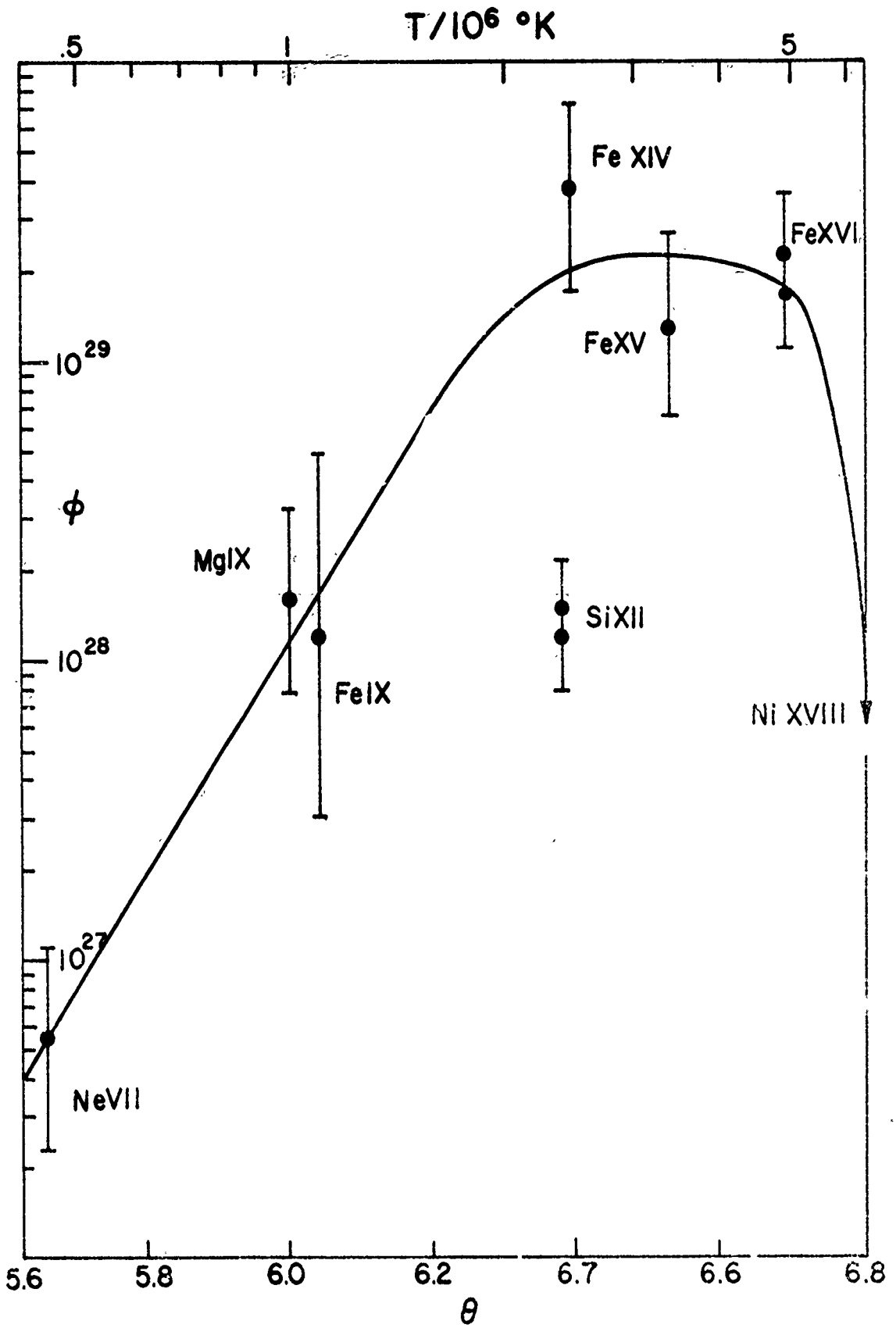
T/10⁶ °K
.5
1
5
Fe XIV
FeXVI
FeXV
10²⁹
φ
MgIX
SiXII
10²⁸
FeIX
Ni XVIII
10²⁷
NeVII
5.6
5.8
6.0
6.2
6.7
6.6
6.8
θ

Figure VI-1

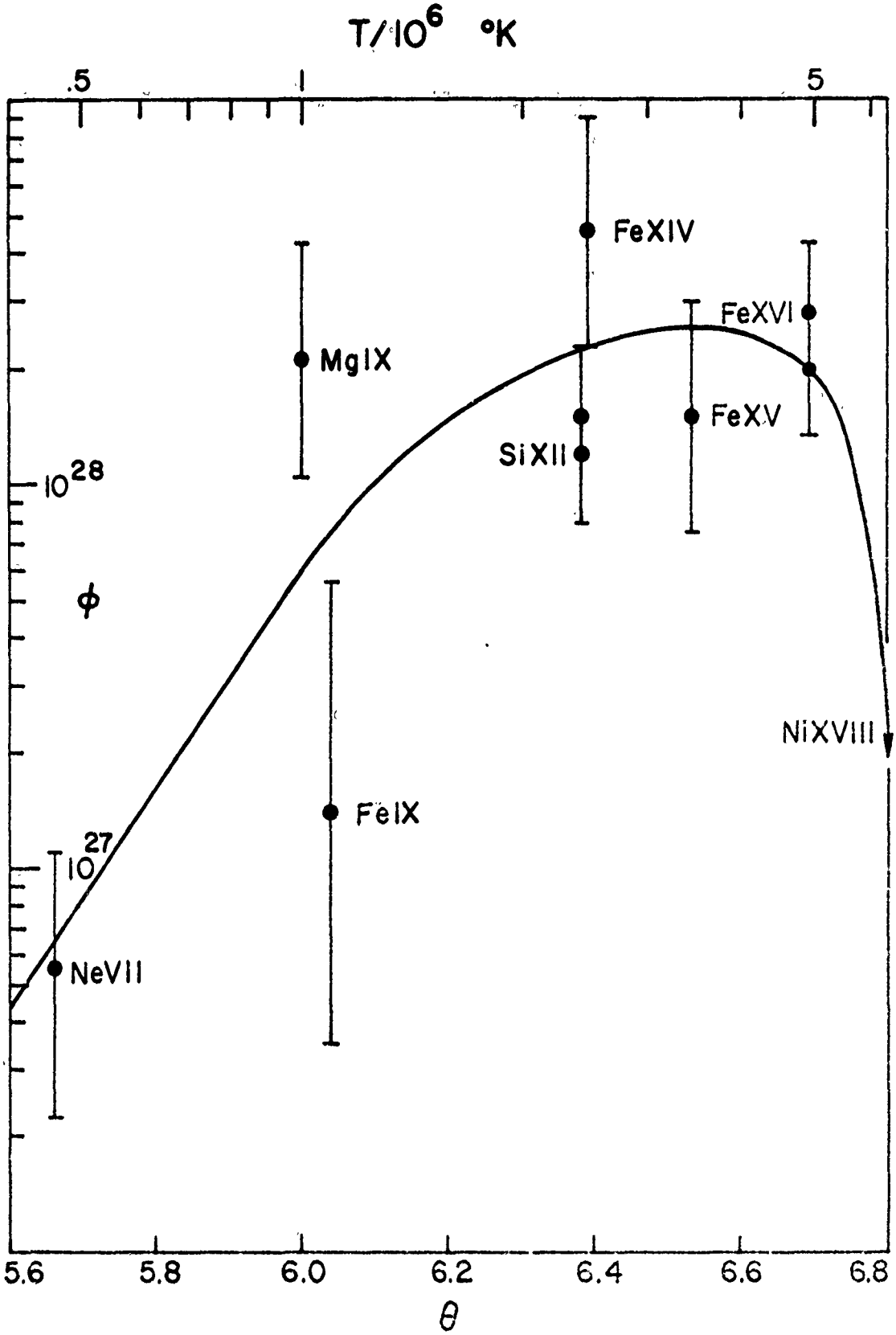
T/10^6 °K
.5
1
5
FeXIV
FeXVI
MgIX
FeXV
SiXII
10^28
φ
NiXVIII
FeIX
10^27
NeVII
5.6
5.8
6.0
6.2
6.4
6.6
6.8
θ

Figure VI-2

Figures VI-3 and VI-4.

The curves $\phi(0)$ repeated from Figures VI-1 and VI-2 respectively, are shown as solid lines. The dashed line shows the corrected curve, $\phi_{cor}(0)$, inferred from the errors implied by the shifts indicated by the arrows (see text).

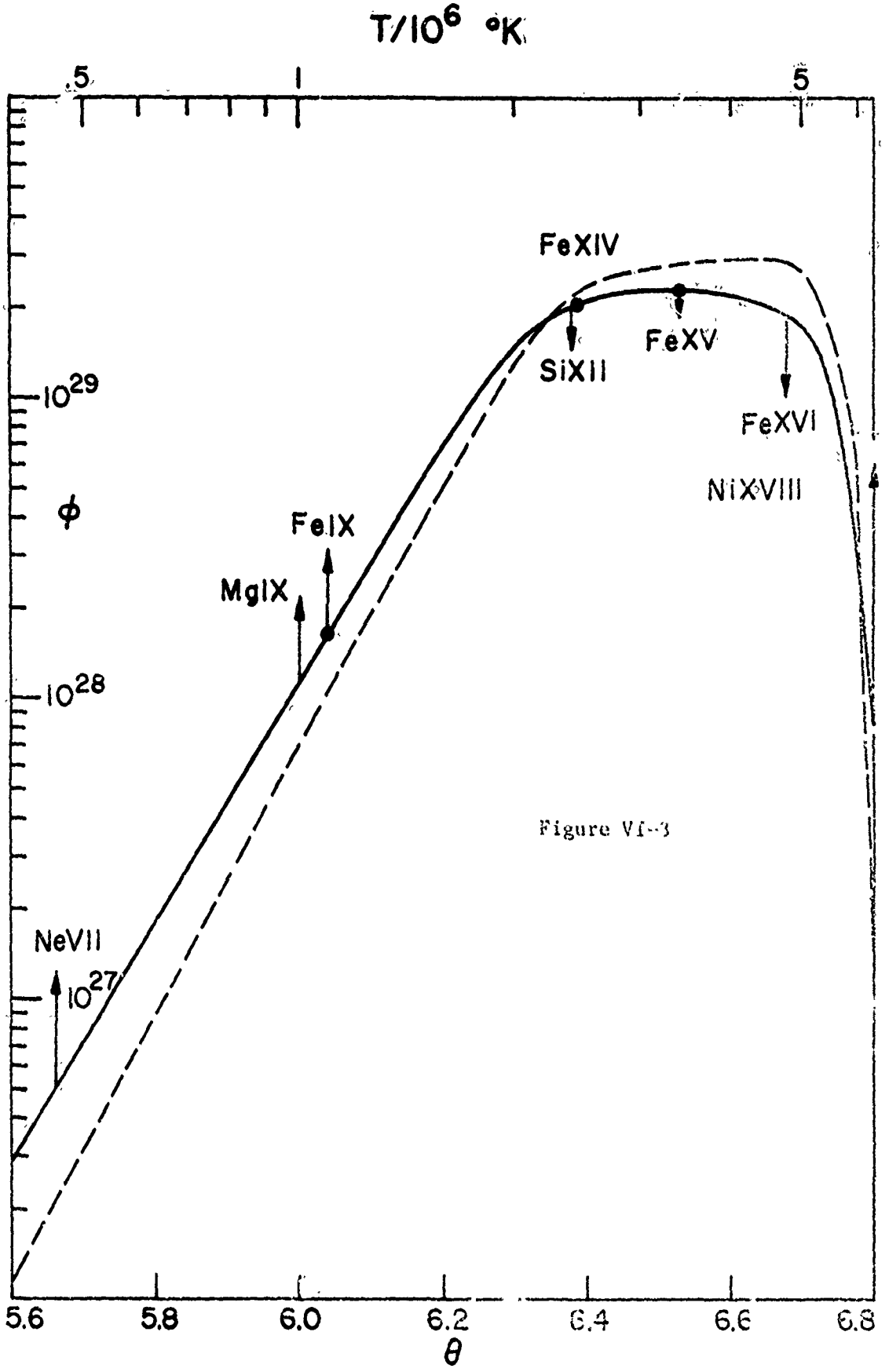
T/10^6 °K
.5
1
5
FeXIV
SiXII
FeXV
FeXVI
NiXVIII
10^29
φ
FeIX
MgIX
10^28
NeVII
10^27
5.6
5.8
6.0
6.2
6.4
6.6
6.8
θ

Figure VI-3

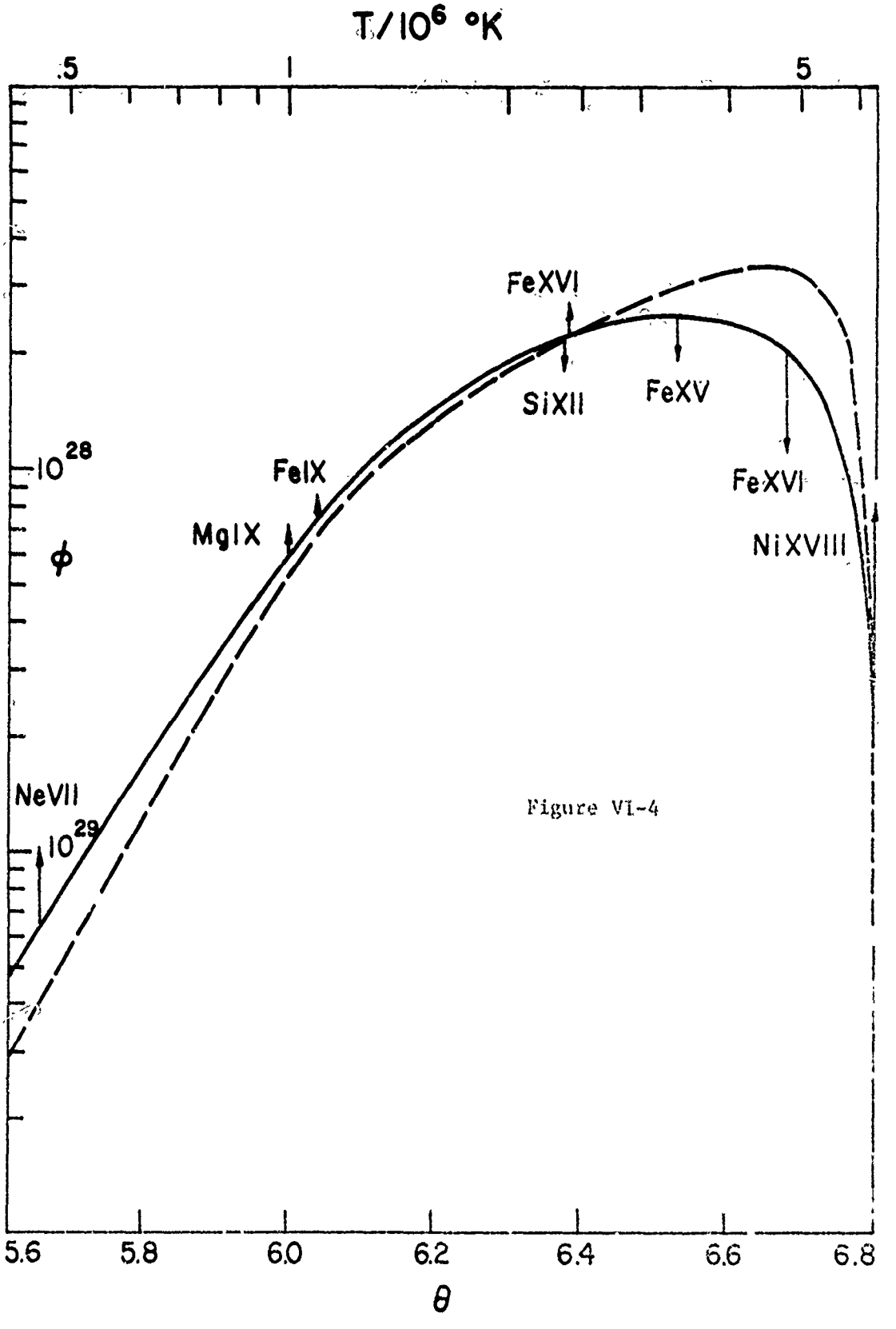
T/10^6 °K
.5
1
5
FeXVI
SiXII
FeXV
FeXVI
NiXVIII
FeIX
MgIX
10^28
φ
NeVII
10^29
5.6
5.8
6.0
6.2
6.4
6.6
6.8
θ

Figure VI-4

CHAPTER VII

STRUCTURAL DETAILS OF THE LIMB ENHANCEMENT

A. Computation of the Emissivity from Brightness Measurements

A series of isophotal maps of Feature 4 in all the lines intense enough to yield reasonably good photometric data is shown in Figures VII-1 to VII-7. From these maps I obtained distributions of brightness of the feature in the various lines along the limb at several different heights. In an optically thin emitting gas, such a brightness distribution gives the total emissivity of the gas along each line of sight. In order to obtain the emissivity at any given point within the feature, it is necessary to either have some additional information of the three-dimensional shape of the feature, which we cannot directly observe, or to fall back on some plausible, but still arbitrary symmetry assumption. Most active features seem to possess an approximate axial symmetry with either a roughly circular or elliptical cross section. The extension from circular to elliptical geometry is easily made by multiplying all dimensions along the line of sight by a constant scale factor, b. The emissivities calculated will then be proportional to b^{-1} and the corresponding electron densities will vary, less sensitively as $b^{-\frac{1}{2}}$. Since an extension from circular to elliptical cross section is trivial, I shall assume for the present that circular-cylindrical symmetry exists in the following development.

Consider a cylinder of radius r_o of an emitting gas which is optically thin. Let r be the distance from the axis of the cylinder. Assume that the emissivity of the gas E is a function of r only. Then, if we view the cylinder perpendicularly to its axis, the brightness I as a function of the distance x of the line of sight from the axis is given by

$$I(x) = 2\int_x^{r_o} \frac{E(r)\, r\,dr}{(r^2 - x^2)^{\frac{1}{2}}} \tag{1}$$

We may invert eq. (1) and obtain

$$E(r) = -\frac{1}{\pi}\int_r^{r_o} \frac{I'(x)\, dx}{(x^2 - r^2)^{\frac{1}{2}}} \tag{2}$$

In principle, eq. (2) affords a possibility of numerically computing the emissivity by direct substitution of measured values of dI/dx into a numerical integration formula. In practice, one would wish to obtain a series representation of eq. (2) that would allow direct substitution of measured values of $I(x)$ rather than $I'(x)$. Such a series of the form

$$E_j = r_o^{-1} \sum_k a_{jk}\, I_k \tag{3}$$

has been derived by Bockasten (1961), with the a_{jk} tabulated for ten and twenty points between $x = 0$ and $x = r_o$. Bockasten also calculates the coefficients for the points numbered from 30 to 40 in the edge of the distribution for improved accuracy at the edge

of the cylinder. The accuracy of the numerical approximation is to within a few percent at worst, provided the quantity $I'(x)$ does not appreciably change within a given pair of points.

Figures VII-8 to VII-14 show the emissivity curves, obtained by an inversion of the brightness curves using Bockasten's method. The accuracy of these curves decreases outward from the axis from an increasingly unfavorable signal-to-noise ratio in the photometry in the fainter regions. In the case of the Si XII lines, the northern edge of Feature 4 was subject to severe contamination by emission from the southern edge of Feature 3; thus the values obtained from these lines may be quite uncertain.

The computation of the emissivity of Feature 4 in the different lines affords a means of partially checking the relative abundances of ions whose variations in emissivity with temperature are similar. Such a pair of ions belonging to different elements is Mg IX and Fe IX. Computations show that the ratio of the normalized emissivity curves of the two ions varies somewhat irregularly between 0.4 and 1.6 between temperatures of 4.5×10^5 °K and 2×10^6 °K. Thus we may consider this range of temperatures as characteristic of both lines, and assume an average temperature of about 10^6 °K for Feature 4 as observed in the two lines. From eq. V-(6), we then obtain $A_{Fe}/A_{Mg} = .20(E_{171A}/E_{368A})$. A casual comparison of Figure VII-8 with Figure VII-12 shows that although the emissivity of Mg IX appears subject to more sensitive variations throughout the feature, the emissivities of the two lines are about equal in magnitude. This would indicate a ratio of $A_{Fe}/A_{Mg} \approx 0.20$. By

comparison, the same ratio is 1.67 from Pottasch's (1967) data, and 0.15 from Goldberg, Müller, and Aller (1960).

Table VII-1 shows the calculated values of the abundance ratio A_{Fe}/A_{Mg} at various points within the enhancement. The figures in parentheses denote the weighting factors assigned to each point for a statistical analysis, and are proportional to the averages of the brightnesses of the two lines at each point. We find a weighted mean value of .25, with a dispersion of .17 from the data of Table VII-1, for the ratio of the iron-to-magnesium abundance. Thus the amount of scatter is not sufficient to admit to an error large enough to allow the Pottasch abundance on the basis of random photometric error alone. The calibration of the photometry is particularly uncertain in the wavelength region of 170Å, however, due to strong variations with wavelength in the transmission coefficient of the aluminum filter (Figure II-2). More important is fact that the random errors in the relative emissivity measurements within a feature are small enough that we may use these measurements for other ions, whose emissions differ greatly among one another, to determine a set of temperature and density profiles of the enhancement as a function of distance from the axis of symmetry.

B. Temperature and Density Structure

1. Method of Analysis

In principle, we can write down eq. V-(6) for any two lines and compare the theoretical emissivity ratio with that calculated at each point by the methods described in the preceding section. We then

have two equations in the two unknowns, temperature and electron density, and can solve for both of them simultaneously. If there is no unresolved coronal structure, then at each point in space the emissivity ratio of all possible pairs of lines should give a unique set of values for the temperature, to within the limitations of our ionization and excitation theories, observational accuracy, and symmetry assumptions. Conversely, any unresolved inhomogeneity in a coronal feature should show two effects, namely:

(a) The temperatures and densities computed will not reflect the structure of the region as a whole, but will tend to map the relative degree of occurrence of temperatures and densities intermediate between those characteristics of the two lines under consideration. Since a point in space can now no longer be associated with a single temperature, radiation from ions of widely different ionization potentials may be seen together.

(b) The radiation of all lines will be enhanced over what it would be in an homogeneous gas. This is due to the N_e^2 dependence of the emissivity of the gas. The electron density we measure from line emission excited by collisions is thus the root-mean-square density at an unresolved volume within the feature. For an homogeneous gas, $\overline{N_e} = (\overline{N_e^2})^{1/2}$, whereas for an inhomogeneous gas, $\overline{N_e} < (\overline{N_e^2})^{1/2}$.

We are now in a position to obtain the temperature and density at each point in space from emissivity ratio measurements and the emissivity curves in Figures VII-8 to VII-14. In order to minimize the uncertainties resulting from rather poorly known [illegible] abundances, I restricted the comparison to [illegible]

of lines were compared for their emissivity ratios throughout the enhancement, namely, Fe IX at 171A with Fe XIV at 211A, and Fe XIV at 211A with Fe XVI at 361A. These lines give good coverage throughout the usually-encountered range of coronal temperatures.

2. Temperature Structure

Figures VII-15 and VII-16 show the temperatures at various heights above the solar surface plotted as a function of distance from a line extending outward from the limb from the point of maximum brightness of the feature. The dissimilarity of both the shape of the curves and the temperatures themselves indicates that we indeed are not viewing an homogeneous structure. Several characteristics of the temperature plots, however, suggest some large-scale structures that might help to explain the discrepancy.

Along the limb, both the Fe IX/Fe XIV and the Fe XIV/Fe XVI emissivity ratios indicate a marked rise in temperature toward the axis of the feature. This temperature increase is particularly marked in the hotter ions, both in the magnitude and in the degree of centralization of the higher temperatures. In the cooler ions, the inferred temperature appears to decrease slowly outward from the axis to a minimum at a distance of about 40,000 km. From this value outward, the temperature begins to rise again. The hotter ions show somewhat similar behavior qualitatively, but with a greater asymmetry in favor of higher temperatures to the north.

As we move outward from the surface, the temperature increase towards the axis of the feature continues in the measurements from the cooler ions, but is reversed in the hotter ions. All the curves

continue to show an increase toward the edge of the feature which moves in toward the center as the height increases. The preceding description of the behavior of the measured temperatures from the line emissivity ratios suggests a picture of the enhancement that includes the following:

(a) A hot "core" is present that contains considerable material favorable for emission in all three lines. This core is probably roughly hemispherical and cuts off rather abruptly somewhere around 20,000 km above the surface.

(b) The core decreases rather strongly in temperature out to about 30,000 km from the center. At that point an "envelope" begins which starts increasing in temperature outward. From about 1 - 2 x 10^6 °K, the distribution of temperatures in the material in this envelope appears symmetrical about the axis, to a good approximation. Toward the north, however, there is a disproportionate amount of material above 3 x 10^6 °K compared with that toward the south.

(c) As we move upward from the core, the envelope closes over it. Towards the center, the temperature range appears to be rather narrow, but as one goes outward, both Fe IX and Fe XVI emissions increase relative to Fe XIV. This shows that the envelope becomes less homogeneous as one moves outward from the axis.

An investigation similar to the present one conducted earlier by Nishi and Nakagomi (1963), arrives at conclusions concerning a two-component enhancement that are very similar to mine. The earlier investigation used measurements of forbidden line emission from the red, green, and yellow lines of Fe X, Fe XIV, and Ca XV, respectively.

3. Density Structure

Figures VII-17 and VII-18 show the root-mean-square density structure of Feature 4 as inferred from the line emissivity ratios. The results are much more nearly consistent with each other than was the case with the temperature measurements, although the increase in the amount of hotter material toward the center is evident in the sharper maximum of the Fe XIV/Fe XVI curve at the limb. A sharp decrease of these curves toward the south at 20,000 km and at 40,000 km also reflects the cooler envelope that exists particularly toward the south.

The inhomogeneity of the feature is suggested strongly by the fact that the densities recorded approach higher values than those generally associated with white light measurements of coronal enhancements (Newkirk 1961) and approach values normally reached only by sporadic condensations (Waldmeier and Müller 1950, Saito and Billings 1964). In the hotter ions, the inferred densities drop off more rapidly with height than in the cooler ions. This phenomenon is also easily seen in the measured brightness scale heights which are available from the isophotal contour maps (Figures VII-1 to VII-7).

Figure VII-19 shows a comparison of the brightness gradients of Feature 4 in several lines of various temperatures. For reference, the Newkirk (1961) density model along the axis of the feature,

$$N_e \propto 10^{4.32/r} \qquad (4)$$

is shown, squared, to represent the brightness gradient that would

result from a cylindrical feature whose density out from the limb varies as Newkirk's model, and whose temperature structure is isothermal. Lines of temperatures of between one and two million degrees agree most closely in their brightness profiles. The confining of hotter material to regions closer to the surface is, of course, contrary to the predictions one would make by assuming a purely hydrostatically supported atmosphere.

C. Comparison with Radio Observations

Observations of the sun at radio frequencies of 9.1 cm at Stanford provide a good means of comparison of the brightness temperatures inferred from the temperature-density structure of the enhancements, and the brightness temperatures actually observed. A contour map of the northeast quadrant of the sun with the contours denoting constant brightness temperatures is given in Figure VII-20 for April 28, 1966, based on the Stanford radio data.

Let us consider at first emission from the corona only. The differential optical depth at radio wavelengths as given by Shklovskii (1951) is

$$d\tau = 1.65 \times 10^{-7} \left(\frac{10000}{T}\right)^{3/2} \frac{1}{\nu^2} N_e^2 \, dx \qquad (5)$$

If we allow the temperature to vary along the line of sight, and consider only radio emission at 9.1 cm, the wavelength at which the Stanford interferometer operates, (5) becomes

$$d\tau = 1.52 \times 10^{-20} N_e^2 T^{-3/2} \, dx \qquad (6)$$

From (6), we can obtain an expression for the radio brightness temperature of the feature by the relation

$$T_{br} = \int_0^{\tau} T \exp\left\{ - \int^{t} d\tau' \right\} dt$$

$$= 1.52 \times 10^{-20} \int_{-\infty}^{\infty} \exp\left\{ 1.52 \times 10^{-20} \int_{-\infty}^{x} N_e^2 \, T^{-3/2} \, dx' \right\} \times N_e^2 \, T^{-1/2} \, dx \qquad (7)$$

where the path of integration is taken along the line of sight.

Although we do not have a really self-consistent model of the coronal enhancement that specifies uniquely a temperature and electron density at each point within Feature 4, the temperatures and densities obtained from the Fe XIV/Fe XVI line emissivity ratios should reflect fairly well most of the material that contributes appreciably to the radio emission in the enhancement. The Fe IX/Fe XIV emissivity ratios reflect some additional, cooler material, but the two temperature regimes overlap considerably in the samples of material they contain. Therefore, by simply adding the two densities at each point and taking an average temperature one almost certainly would overestimate the amount of material actually contained in the enhancement. I therefore consider that the hotter material, from about 2×10^6 °K upwards, will provide a lower limit to the predicted radio brightness temperatures that is fairly close to the actual values.

The results of a numerical integration of the model of the enhancement implied by the temperature of Figures VII-15 and VII-16,

and the densities of Figures VII-17 and VII-18, according to eq. (7), are shown in Figure VII-21. The values of N_e^2 from which the integration was made were those inferred from the Goldberg abundances of iron as given in Table VI-1. The abundance of Fe according to Pottasch is larger by a factor of 8.3, and therefore the inferred values of N_e^2 are smaller by the same amount. In a feature that is optically thin in the 9.1 cm radio region, the predicted brightness temperatures would be reduced uniformly by a factor of 8.3 as a result of the increase in abundance of Fe. Since the feature is not necessarily optically thin, however, the reduction may be smaller, particularly along the line of sight that passes through the greatest amount of material, as a result of more self-absorption occurring in the denser regions. The brightest point differs in the two models by a factor of 6.0, and the ratio of course, approaches 8.3 for the fainter regions. This indicates that, although self absorption is significant, it does not greatly change the brightness profile of the enhancement over the range of densities we are considering. We may therefore assume for the purpose of the discussion that follows that the Pottasch abundance of Fe predicts brightness temperatures in the 9.1 cm emission that are lower by a factor of seven compared with the Goldberg abundances, and that the surface brightness distribution of the feature is essentially unchanged.

We are now in a position to estimate the brightness temperature that would be measured by the Stanford radio interferometer with its main lobe centered on the enhancement. Although the antenna pat-

along one of the two axes of the cross is that a modulated sine curve, we may approximate the main lobe by a Gaussian curve provided the scale of the feature is somewhat less than the beamwidth of the antenna. The width of the beam of the interferometer is 3'.1 at the half-power points; this corresponds to about 1.5×10^5 km at the solar surface. The corresponding Gaussian width is 9.2×10^4 km which we denote as y_1 and z_1, along the y and z axes respectively. We can represent the radio brightness of Feature 4 quite well by a doubly infinite Gaussian curve along the z-axis with characteristic width $z_o = 2.6 \times 10^4$ km, and a half-Gaussian curve infinite in the positive y-direction with width $y_o = 10^4$ km. The observed brightness temperature of such a feature against a zero background will then be

$$\tilde{T} = T_{max} \frac{\int_{-\infty}^{\infty} \int_{0}^{\infty} \exp\left\{-y^2(y_o^{-2} + y_1^{-2})\right\} \exp\left\{-z^2(z_o^{-2} + z_1^{-2})\right\} dy\, dz}{\int_{-\infty}^{\infty} \int_{0}^{\infty} \exp(-y^2/y_1^2) \exp(-z^2/z_1^2)\, dy\, dz} \qquad (8)$$

For $T_{max} = 1.98 \times 10^6$ °K this becomes

$$\tilde{T} = \begin{cases} 5.8 \times 10^4 \text{ °K} & \text{(Goldberg abundances)} \\ 8.3 \times 10^3 \text{ °K} & \text{(Pottasch abundances)} \end{cases} \qquad (9)$$

A comparison of these values of the predicted brightness temperature with those shown on the Stanford radio maps is interesting. On April 28, 1966, a radio enhancement with a maximum recorded brightness temperature of 125,000 °K is evident at the position of Feature

3. The position of Feature 4 is marked by a dotted circle on Figure VII-20, and is shown to be at a position of brightness temperature around 6×10^4 °K. Comparison of the positions of the two features with the theoretical response pattern of the antenna to a point source (Swarup 1961) shows that when the beam is centered on one of the two features, the other is close to a null point and therefore should not greatly affect the measured values of the maximum radio brightness temperatures. On the other hand, Features 2 and 3 are so situated with respect to the antenna pattern that when the beam is centered on one, the other is within a positive side lobe. The response pattern at this point is down by a factor of about ten; this indicates an error of about 10% in the brightness temperature would result from considering the response of the main lobe only.

In comparing the observed brightnesses of Features 3 and 4, we must also consider the variation in the amount of observed background from the quiet solar disk when the antenna is trained on the two features, and the possibility of a chromospheric contribution to the radio emission from Feature 3. Observations of the radio limb well away from active regions show that a difference of about 10^4 °K could result from the disk of the quiet radio sun not entirely filling the main lobe where the interferometer is trained on Feature 4. If we subtract the two spurious effects of sidelobe emission from Feature 2, and the increase of background emission from the solar disk, we get a radio brightness of about 10^5 °K for Feature 3 as compared with about 6×10^4 °K for Feature 4. The ratio of

these figures should be approximately the same as the brightness ratios we would obtain from the photometric brightnesses in the extreme ultraviolet listed in Table VI-2. The agreement is quite satisfactory.

Although most of the emission in the 9.1 cm region from the quiet sun comes from the chromospheric layers, it is doubtful that chromospheric variations in temperature and density can account for a significant amount of the radio enhancement in an active region. A number of plages appear on the solar disk on April 28, 1966 from the Fraunhofer maps; these plages do not in general correlate well with the radio enhancements unless there is obvious EUV enhancement in the lines of the hotter ions as well. To some extent this is a result of the fact that the chromospheric layers are optically thick at 9.1 cm and the temperatures associated with the chromosphere, by the usual definitions, do not go above a few 10^4 °K. Such variations in temperature of features the size of the enhancements we are considering would be scarcely noticeable above background variations in the observed brightness temperatures.

Although the presence of a strong coronal EUV enhancement may be a necessary condition for one to observe a strong radio brightening, it is doubtful that it represents a sufficient condition. Observations of the radio enhancement associated with Feature 4 show a progressive increase in intensity for several days after its initial appearance at the limb. This indicates that much of the additional radiation comes from low in the corona from a relatively shallow layer, and is therefore subject to foreshortening at the limb.

Billings and Hatt (1968), after a study of the correlation of radio noise in the 10 cm region with the quantity $N_e^2 T^{-\frac{1}{2}}$ as inferred from coronal line observations, conclude that the low level of correlation (about 0.25) suggests that most of the radio emission occurs from levels lower down in the corona than those accessible to the coronagraph.

D. Comparison with K-Coronameter Observations

In addition to checking our temperature and density model of Feature 4 against radio observations, data obtained by the K-coronameter of the High Altitude Observatory at Mauna Loa, Hawaii give us the possibility of independently checking the electron densities. An interesting possibility exists, in theory at least, of obtaining a measure of the degree of inhomogeneity of the corona by comparing the densities, N_e, measured by the K-coronameter with the root-mean-square densities, $(\overline{N_e^2})^{\frac{1}{2}}$ inferred from radio and emission line observations. Because of uncertainties in the background from the quiet K-corona, however, the actual contribution to the total reading from Feature 4 is quite uncertain, and the limited resolution of about one minute of arc (Hansen 1967) also contributes to making the data insufficiently accurate for a definite comparison. Nevertheless, the K-coronameter observations provide another check on the electron density that is essentially independent of the relative abundances of the heavy elements.

The theory of the polarization of the radiation from the K-corona has been developed in detail by van de Hulst (1950). This

the assumption of spherical symmetry, he derives an expression for the polarization times the brightness which, in Newkirk's (1961) notation reads

$$pB = \frac{3.44 \times 10^{-6}}{c} \int N_e[A(R) - B(R)] \frac{\rho^2 dR}{R(R^2 - \rho^2)^{\frac{1}{2}}} \qquad (10)$$

where p is the polarization, or the ratio of the intensity of the radiation component transverse to the solar limb minus the radial component, to the total intensity. The quantity pB is directly proportional to the K-coronameter reading. Here, B is given in units of 10^{-8} times the solar disk brightness.

The constant, c, normalizes the expression to the mean brightness of the solar disk at 5200A, and is equal to 1.32 (Newkirk 1961). The functions A(R) and B(R) contain both the allowance for the finite size of the apparent solar disk at a distance R in determining the polarization, and also the effect of limb darkening. The coordinates ρ and R refer to the projected distance of a point in space upon the sky from the center of the solar disk, and the distance of the point from the sun's center, respectively. Both are given in solar radii.

If we wish to drop the assumption of spherical symmetry and write a general expression for pB along a line of sight, Eq. (10) becomes

$$pB = \frac{1.72 \times 10^{-6}}{c} \int N_e[A,R) - B(R)] \frac{\rho^2}{R^3} dx \qquad (11)$$

where x, as before, it taken as the variable of integration along the line of sight, in solar radii.

The ratio, ρ/R may be assumed nearly equal to unity along the axis of Feature 4. Since the enhancement is relatively small, both R and the ratio ρ/R will change but little along a line of sight through the thickness of the enhancement. Values of A-B are tabulated in van de Hulst's paper (1950). At the two distances from the solar limb for which tracings are available, $1.125R_\odot$ and $1.25R_\odot$, eq (11) reduces to the following:

$$\int N_e \, dx = \left\{ \begin{array}{ll} 3.0 \times 10^{17} \text{ pB} & (\rho = 1.125) \\ 3.3 \times 10^{17} \text{ pB} & (\rho = 1.25) \end{array} \right\} \qquad (12)$$

with x now expressed in centimeters.

The justification for taking A-B and ρ^2/R^2 outside the integral is that these quantities vary little over a line of sight through the feature.

A major difficulty in applying (12) to a single feature lies in the fact that it is difficult to justify a background level for the quiet corona and parts of any other streamers that may happen to lie along the line of sight. We can tentatively assign a lower bound to this background, in view of the fact that there was very little activity in the southern hemisphere on April 28, 1960, and therefore the emission in the southern hemisphere at the same latitude as Feature 4 should provide a lower limit to the quiet component in the northern hemisphere. The values of $\int N_e dx$ thus computed will therefore represent an upper limit of the quantity $\int \ldots_e dx$ through Feature 4 only.

Table VII-2 shows the K-coron[illegible] readings of pB [illegible] 10^{-8} times the solar di[illegible] brightness at position angles [illegible]

70° at $1.125R_\odot$ and $1.25R_\odot$, where the signal maximizes. Values of 25 and 15 were chosen to represent the background values of pb at these two distances, respectively. The corresponding values of $\int N_e dx$ are plotted in Figure VII-22, along with the values of $\int \overline{(N_e^2)}^{\frac{1}{2}} dx$ obtained from the photometric analysis of the EUV line emission. The scatter in the points results in a band of values that spans a factor of about 3 in uncertainty. I shall now discuss the significance of the quantities plotted and their effect on the degree of uncertainty and the tentative conclusions that may be drawn regarding coronal fine structure.

The points represented by dotted circles and dotted squares represent the quantities $\int \overline{(N_e^2)}^{\frac{1}{2}} dx$ along the axis of Feature 4 computed from the density models inferred from the Fe IX 171A and Fe XIV 211A; and Fe XIV 211A and Fe XVI 361A line ratios respectively. Each of these provides a lower limit to the true value, since the observations on which they are based only reflect a portion of the material in the enhancement. Their sum, which more or less completely spans the range of temperatures in the feature, is represented by a circled cross, and serves an an upper limit to the quantity $\int \overline{(N_e^2)}^{\frac{1}{2}} dx$.

The K-coronameter measurements represent an upper limit to the quantity $\int N_e dx$ as described above. Since Feature 3 may well have emission in the continuum extending outward from it that is unresolved from that associated with Feature 4, I have divided the values of $\int N_e dx$ by two and included them on the graph as a lower limit. The uncorrected and corrected K-coronameter values are represented by

dotted and crossed triangles, respectively. Within this band of uncertainty of about a factor of three, the K-coronameter values join quite nicely with the EUV values.

From the above considerations we can set an upper limit to the degree of inhomogeneity in the coronal feature. Consider a sample of gas that is compressed to a value $1/k$ of its original volume. The maximum density will then be increased k-fold and the maximum square density by a factor of k^2. If we then compare the root-mean-square density and the mean density, both averaged over the original volume of the gas, we find that

$$(\overline{N_e^2})^{\frac{1}{2}}/\overline{N_e} = k^{\frac{1}{2}} \qquad (13)$$

If $k^{\frac{1}{2}}$ were much larger than about 3, we should see a definite discontinuity in the points of Figure VII-22, in spite of the aforementioned uncertainties. We therefore conclude that at a distance of about 80,000 km from the solar surface, the density inhomogeneity factor, k, cannot be greater than about ten.

E. Structure of the Magnetic Fields

The observations of the distribution of matter in Feature 4 at various temperatures, as described in Chapter VI, furnish conclusive evidence that the material is not in hydrostatic equilibrium. The observations of the EUV lines show an unmistakable decrease in the scale height of the emission with increasing temperature, and in lines with temperatures greater than about 10^6 °K, the emission scale height is smaller than that predicted from hydrostatic equilibrium of a gas at the temperature appropriate to the existence of

the ion producing the line. There is evidently a sharp decrease in temperature with height, with most of the hot material being confined rather low in the feature in a hot, dense, "core", as we have already seen. Such a temperature structure cannot exist in the corona due to the high conductivity of the coronal material unless the material is held down by transverse magnetic fields, which also reduce the conductivity of the material across the field lines.

For the moment, let us assume that the magnetic fields are static and imbedded in the enhancement. The magneto-hydrostatic force equation that must be satisfied at every point within the enhancement is

$$\frac{1}{4\pi} \vec{B} \times (\nabla \times \vec{B}) = \rho \vec{g} - \nabla p \qquad (14)$$

if we assume that the gravity force, acting in the negative y-direction, is the only external force acting on the enhancement.

We may expand eq. (14) in cylindrical coordinates, and thus make use of the assumed symmetry properties of the enhancement. The symmetry assumptions we shall make are (1) the magnetic field has no azimuthal component, i.e., $B_\phi = 0$, and (2) the feature has complete axial symmetry about the y-axis, i.e., all derivatives with respect to ϕ are zero. With these assumptions, eq. (14) reduces to the two following scalar equations:

$$\frac{\partial p}{\partial r} = \frac{B_y}{4\pi}\left(\frac{\partial B_r}{\partial y} - \frac{\partial B_y}{\partial r}\right) \qquad (15)$$

$$\frac{\partial p}{\partial y} = \frac{B_r}{4\pi}\left(\frac{\partial B_y}{\partial r} - \frac{\partial B_r}{\partial y}\right) - \rho g \qquad (16)$$

A similar pair of equations relating the pressure gradients along the vertical and tangential to the solar limb were derived by Billings (1966). Under our symmetry assumptions, the radial coordinate plays the same role mathematically in (15) and (16) as does the tangential coordinate in Billings' equations. We may eliminate the magnetic field derivatives from (15) and (16) and obtain the following relation

$$\frac{B_y}{B_r} = \frac{-\partial p/\partial r}{\rho g + \partial p/\partial y} \qquad (17)$$

At this point, for the sake of simplicity, we assume a constant temperature for the emitting material of any given ion. In view of the detailed consideration of the shapes of the ionization curves made in an earlier chapter, this assumption is certainly questionable, but it is adequate for a determination [illegible] of the field structure over a wide temperature range. [illegible] is then proportional to the square root of [illegible] we then have

$$\frac{B_r}{B_y}\frac{\partial \ln \epsilon}{\partial r} = -\frac{\partial \ln \epsilon}{\partial y} \qquad (18)$$

This equation gives the slope of the [illegible] of the values of ϵ throughout the chromosphere, [illegible] been computed. A similar expression [illegible]

may be used if one assumes translational symmetry along the line of sight. Such an analysis was made of an enhancement by Saito and Billings (1964) using white light observations of the 1962 New Guinea solar eclipse.

Note that one ambiguity exists in the applicability of eq. (18) in mapping the magnetic field, and that arises when $\partial \ln L / r = 0$, at which point B_r/b_y would, taken literally, become infinite. The field would then have no vertical component. Such a situation could also arise, however, by a nearly radial field whose slope is changing sign as it passes through the point at which L reaches a local maximum. The lines of force will then outline a cusp shape which bears a strong resemblance to the shapes of some coronal streamers.

Figures VII-23 through VII-26 show diagrams of the slopes of the magnetic fields inferred through eq. (18) from the line emission of feature 4 in Mg IX, Fe IX, Fe XIV, and Fe XVI, in order of increasing temperature. The first of these exhibits a field that is nearly vertical, indicating that the distribution of ions of temperatures near 10^6 °K is close to that predicted by static fairly equilibrium. The Fe IX emission is quite similar to that of Mg IX, but the inferred field shows the beginnings of a loop structure and a small tangential component to the field. The Fe XIV emission shows even more loop structure and a stronger horizontal component to the magnetic field, and also a [illegible] about the axis of the feature. The intensity of the [illegible] at 40,000 km to the south of the axis d[illegible]

greater heights, indicating a great deal of confinement of the material below heights of about 30,000 km. The fields governing the Fe XVI emission show a still stronger loop structure and appear to resume the approximate symmetry about the axis of the feature.

An interesting feature common to all the field profiles is the loop structure close to the limb centered at the axis of the enhancement, or very nearly so. There apparently exists a core of material which contains a wide variety of temperatures but favors the hotter material more than the cooler. This conclusion, not surprisingly, is very similar to that inferred from the temperature structure within the enhancements based on line emissivity ratios.

Table VII-1

Position along the limb from I_{max}

height (km)	S 40,000	20,000	0	20,000	40,000 N
limb	.33 (.45)	.21 (.80)	.10 (1.1)	.15 (.82)	.14 (.40)
20,000	.30 (.17)	.20 (.50)	.60 (.60)	.35 (.50)	.06 (.15)
40,000	.32 (.11)	.14 (.25)	.69 (.24)	.23 (.23)	.11 (.012)
60,000	.16 (.029)	.10 (.10)	.23 (.015)	.24 (.090)	

Pettasch - 1.67

Goldberg - 0.15

Table VII-2

K-coronameter brightness readings, and corresponding values of $\int N_e dx$

pos.∠	$pB_{bkg} = 25$, $\rho = 1.125$			$pB_{Bkg} = 15$, $\rho = 1.25$		
	pB	pB-25	$\int N_e dx$	pB	pB-15	$\int N_e dx$
30°	43	18	5.4×10^{18}	22	7	2.3×10^{18}
	44	19	5.7×10^{18}	22	7	2.3×10^{18}
40°	45	20	6.0×10^{18}	27	12	4.0×10^{18}
	46	21	6.3×10^{18}	27	12	4.0×10^{18}
50°	49	24	7.2×10^{18}	26	11	3.6×10^{18}
	51	26	7.8×10^{18}	24	9	3.0×10^{18}
60°	52	27	8.1×10^{18}	27	12	4.0×10^{18}
	55	30	9.0×10^{18}	26	11	3.6×10^{18}
70°	61	36	1.1×10^{19}	28	13	4.3×10^{18}
	55	30	9.0×10^{18}	27	12	4.0×10^{18}
80°	47	22	6.6×10^{18}	23	8	2.6×10^{18}
	39	14	4.2×10^{18}	20	5	1.7×10^{18}
90°	33	8	2.4×10^{18}	20	5	1.7×10^{18}
	30	5	1.5×10^{18}	19	4	1.3×10^{18}
100°	28	3	9.0×10^{17}	17	2	6.6×10^{17}
	27	2	6.0×10^{17}	15	0	0
110°	26	1	3.0×10^{17}			

Figures VII-1 to VII-7

Isophotal contours of Feature 4 in several EUV emission lines. The brightest point is indicated by the tick at the limb. Each contour interval represents a brightness ratio of 1/e.

Figure [illegible]

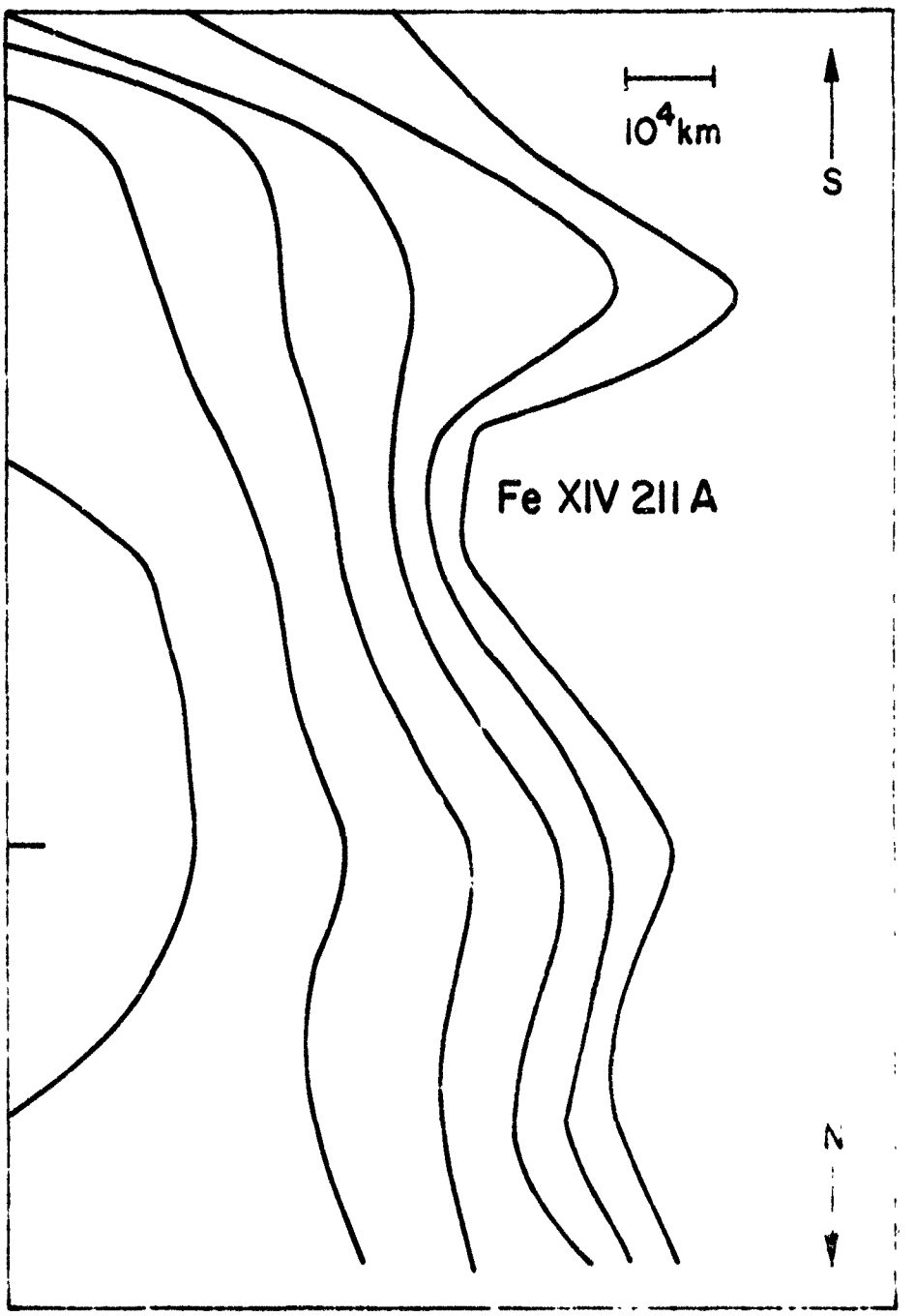
10^4km
S
Fe XIV 211 A
N

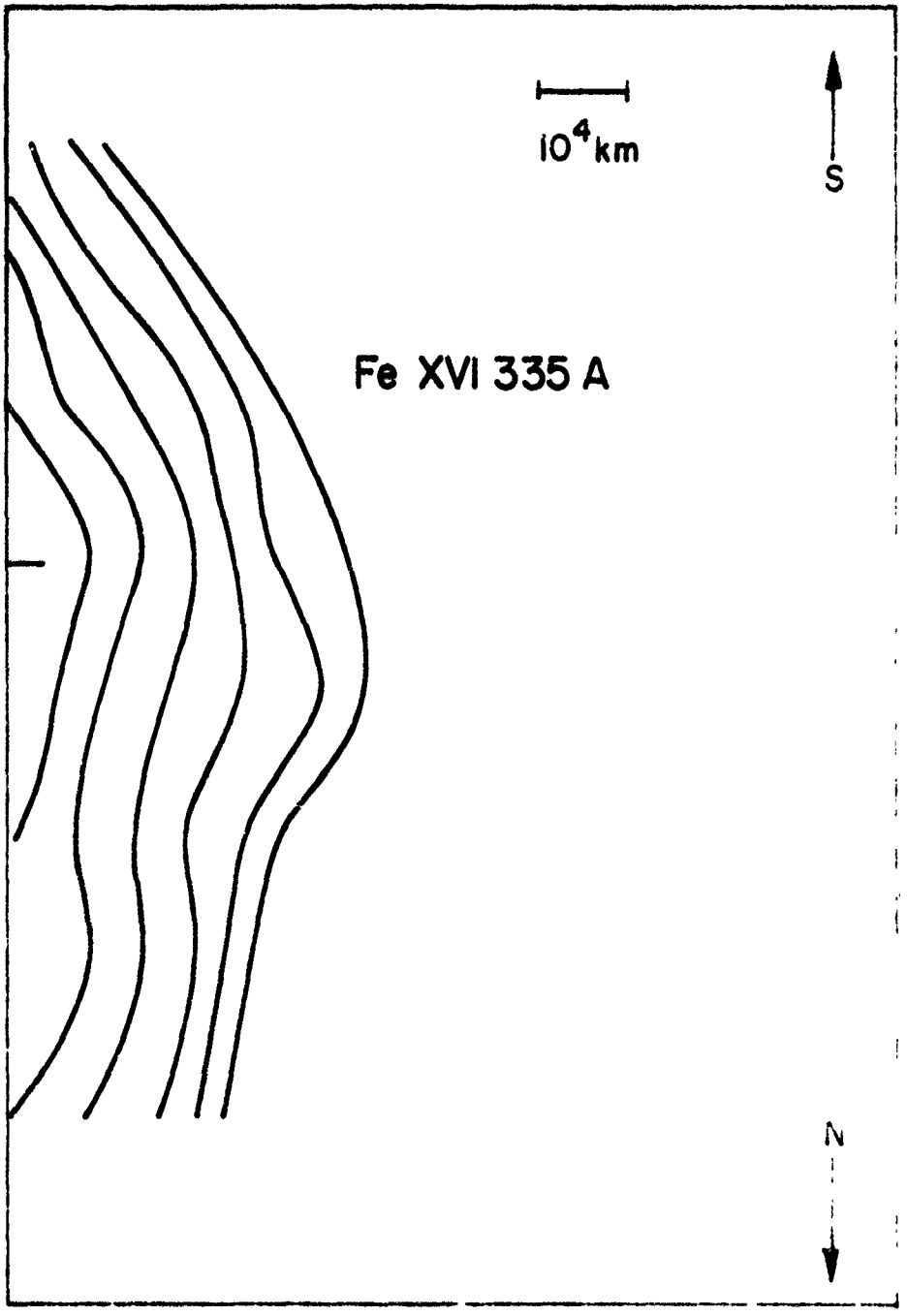
10^4km
S
Fe XVI 335 A
N

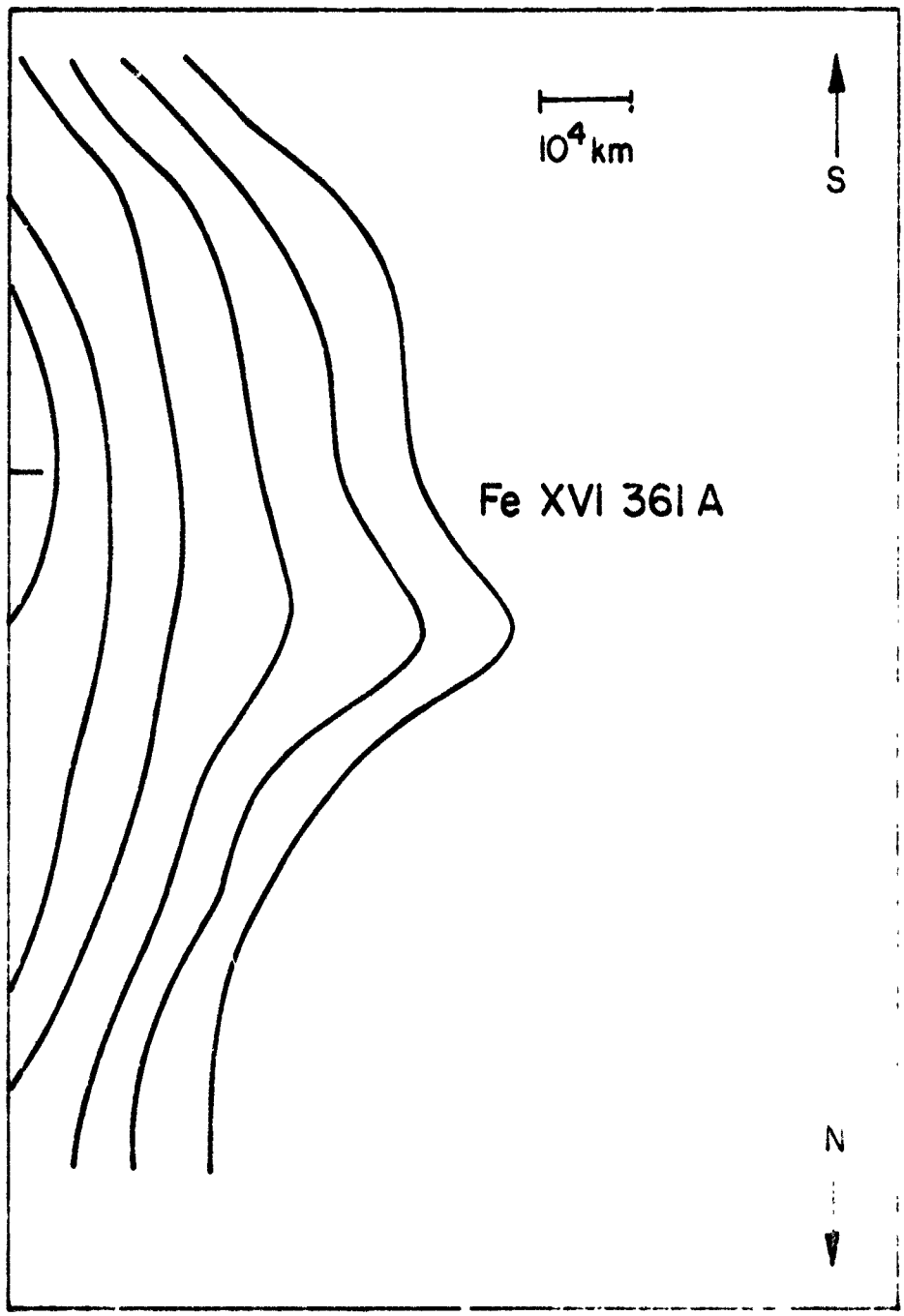

Figure VI

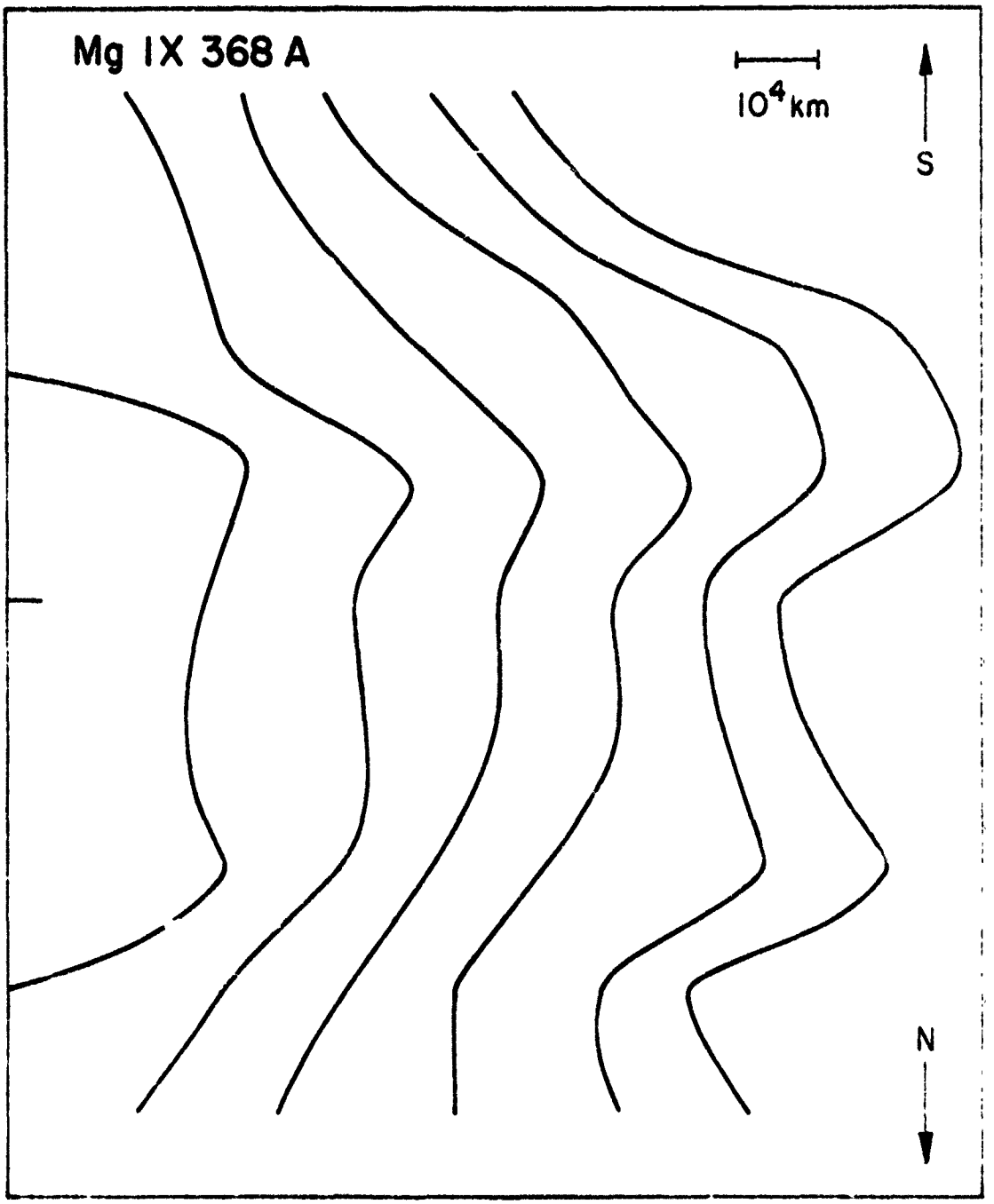

Figure VII-5

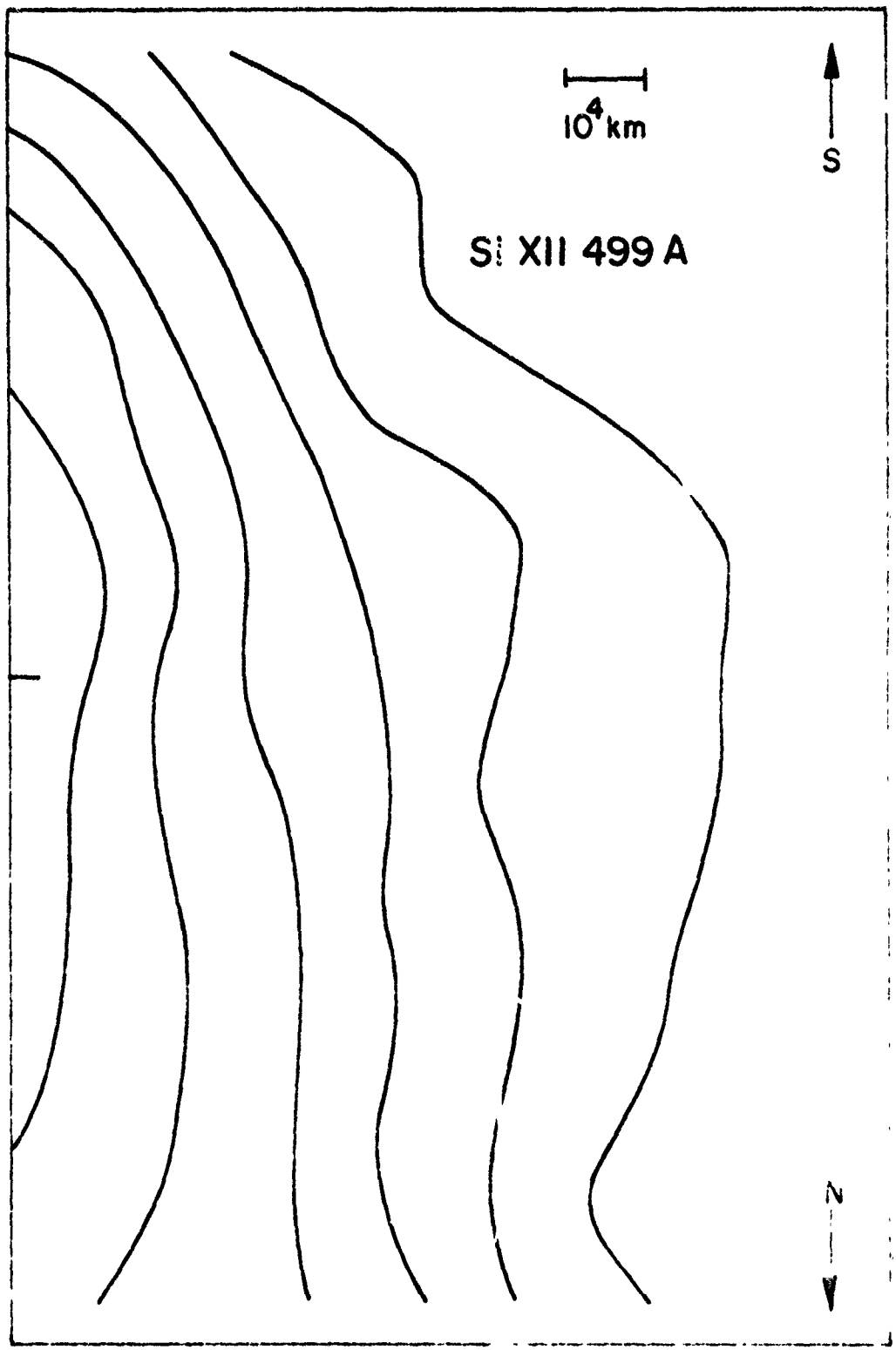
10^4 km
S
Si XII 499 A
N

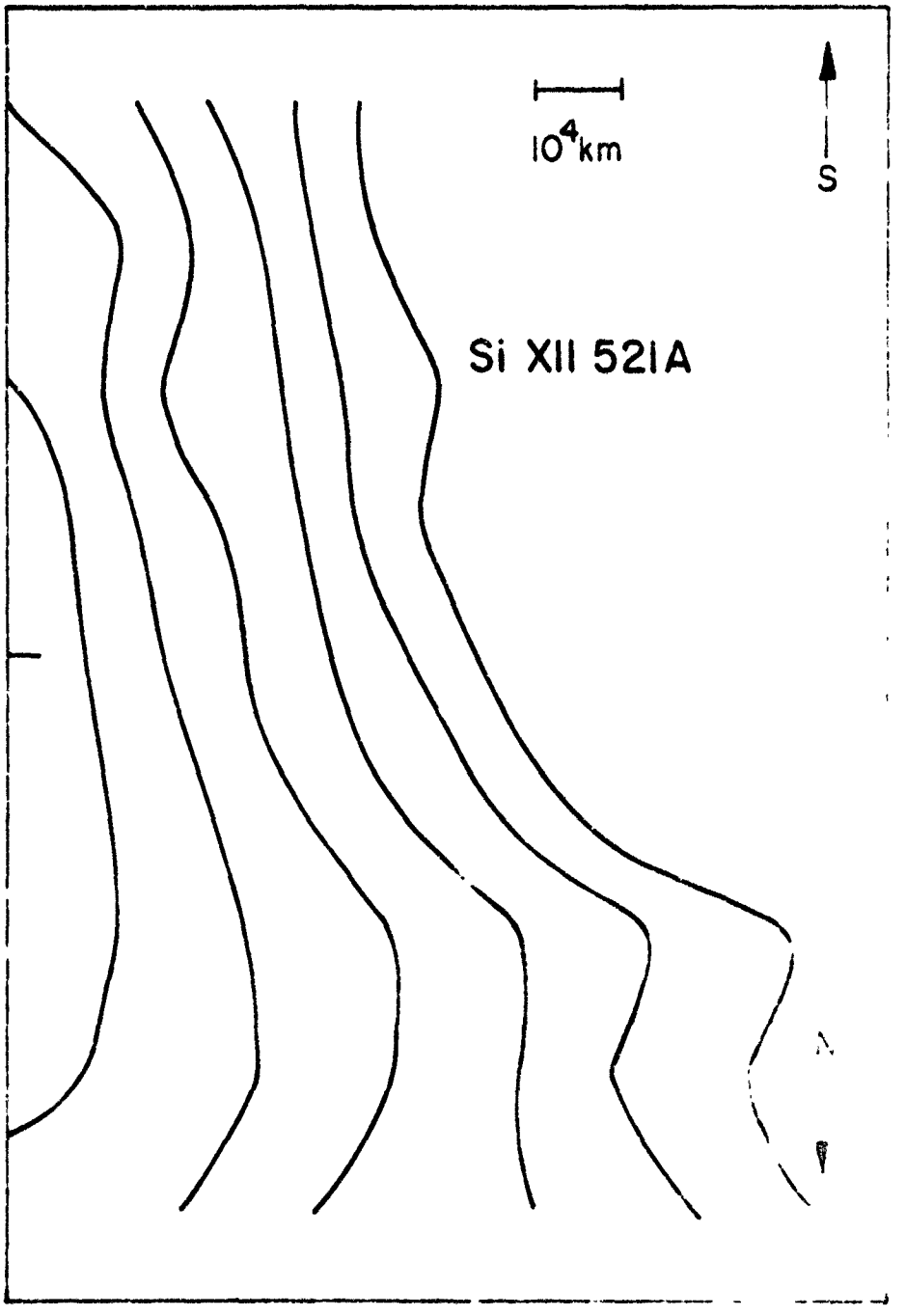
10^4km
S
Si XII 521A

Figures VII-8 to VII-14

The emissivity of the gas within Feature 4 in the same emission lines as in Figures VII-1 to VII-7.

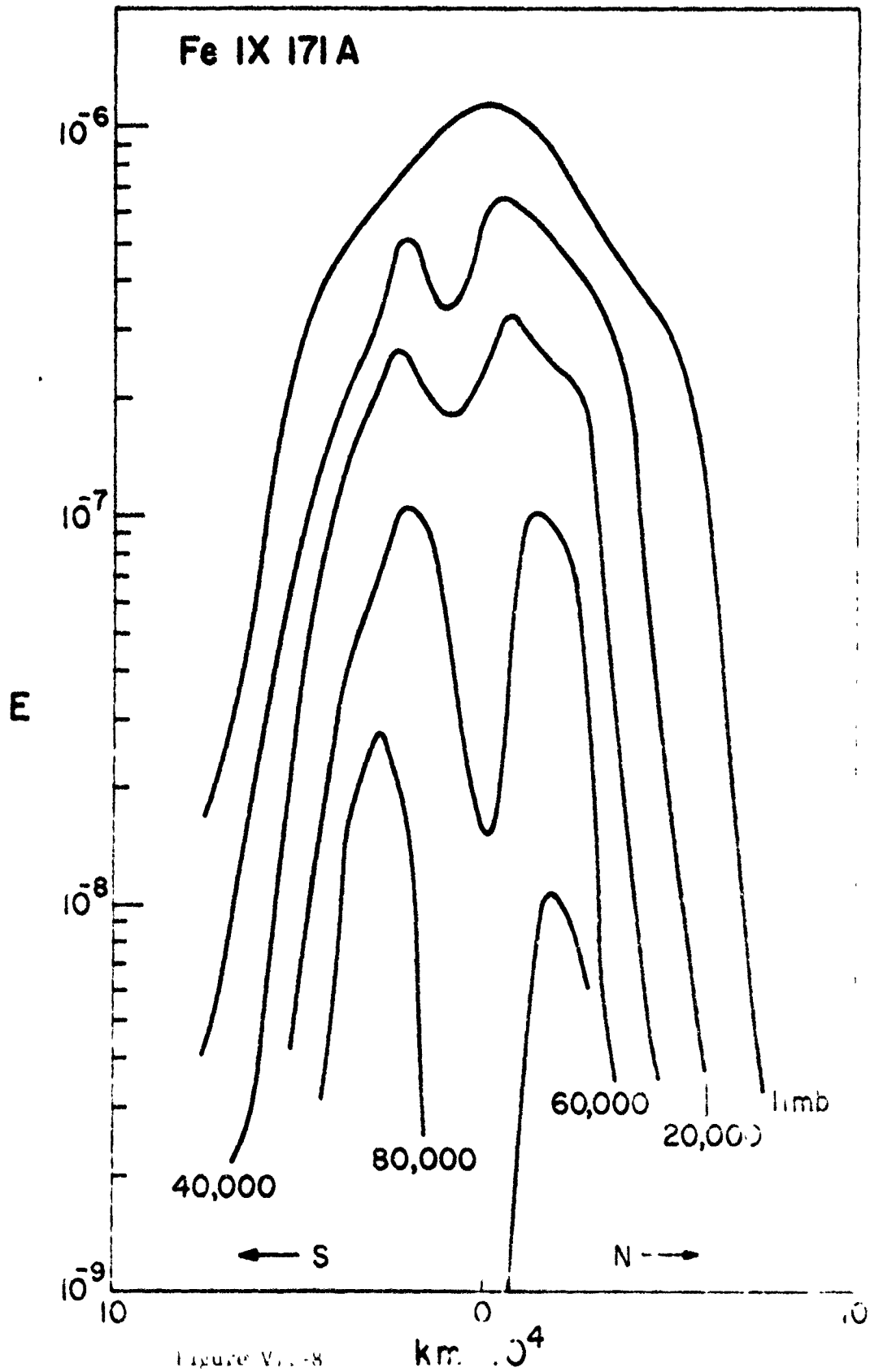
Fe IX 171 A
10^{-6}
10^{-7}
10^{-8}
10^{-9}
E
40,000
80,000
60,000
20,000
limb
S
N
10
0
km. $\cdot 10^4$

Figure V...8

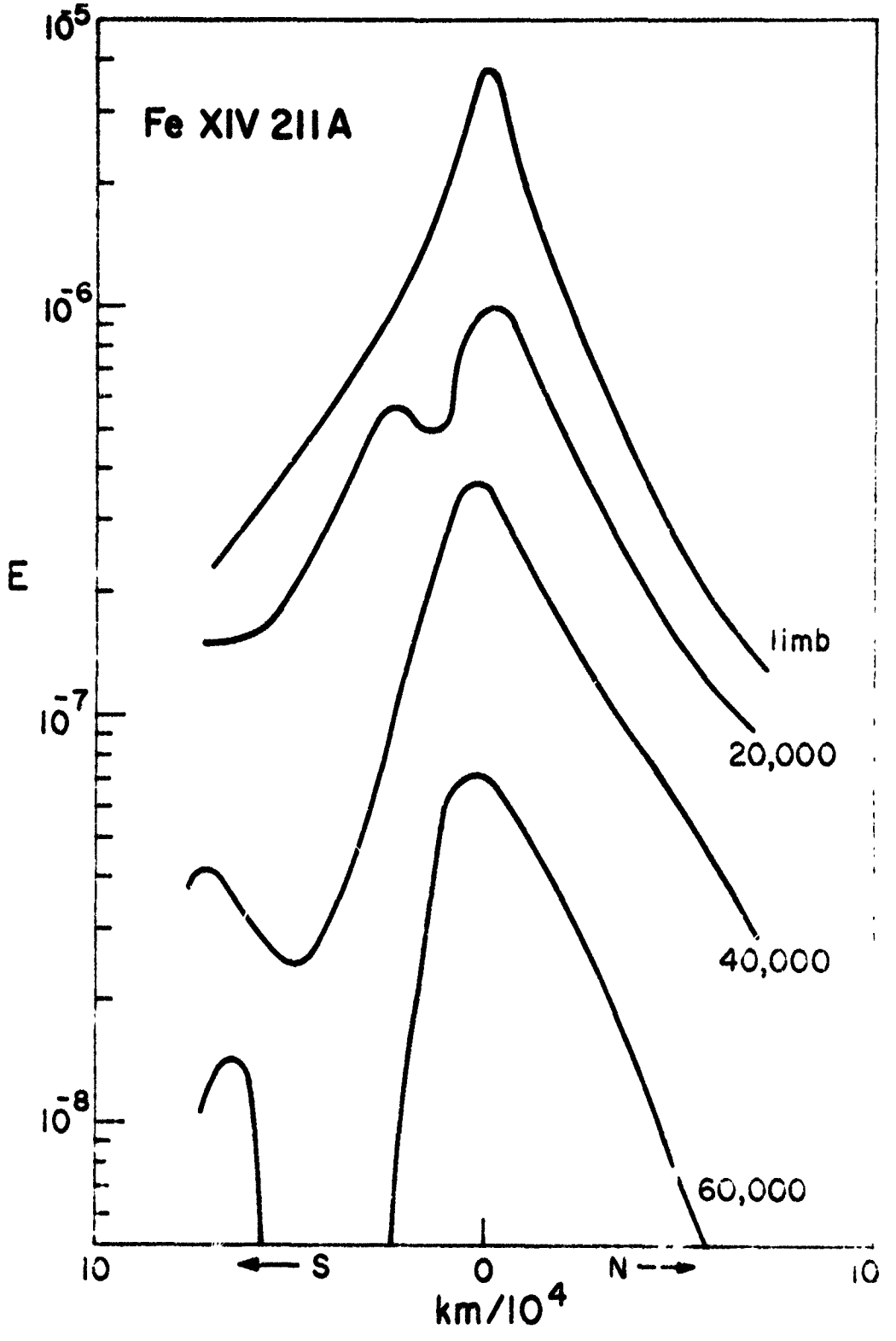
Fe XIV 211A
10^{5}
10^{-6}
10^{-7}
10^{-8}
E
limb
20,000
40,000
60,000
10
S
0
N
10
km/10^{4}

Figure VII-

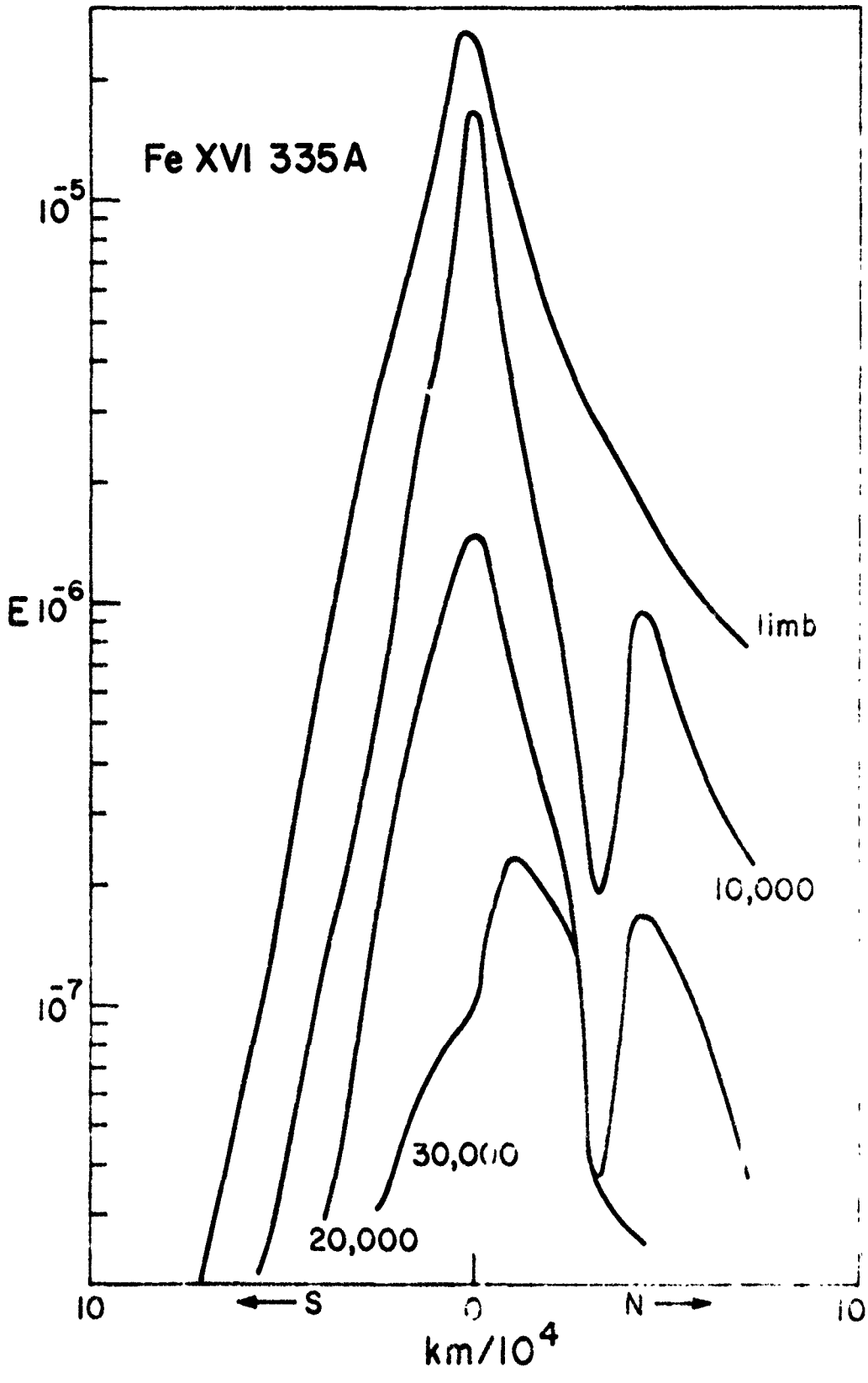
Fe XVI 335A
10^{-5}
E 10^{-6}
10^{-7}
limb
10,000
30,000
20,000
10
S
0
N
10
km/10^4

Figure VII-1

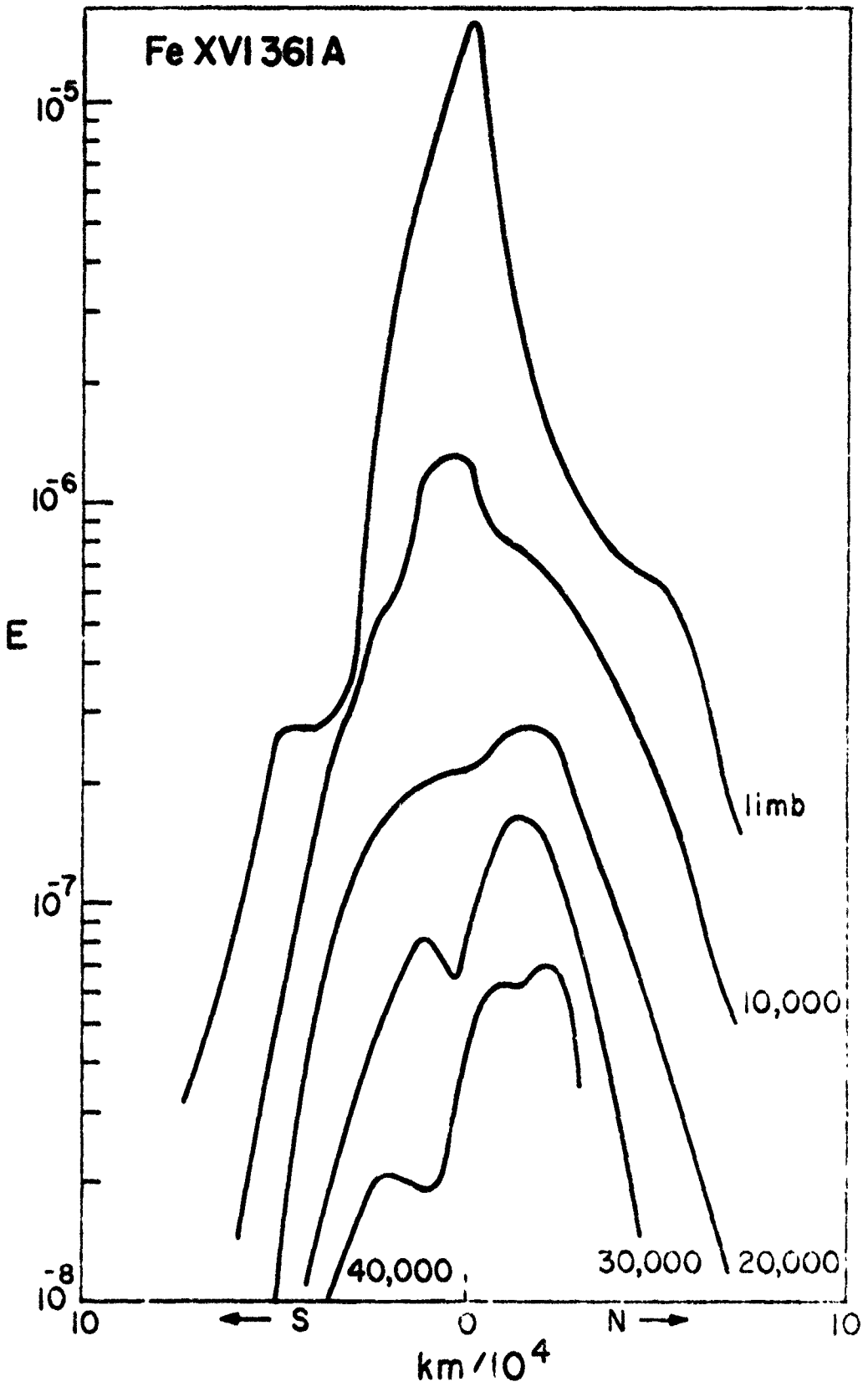

Figure VII-11

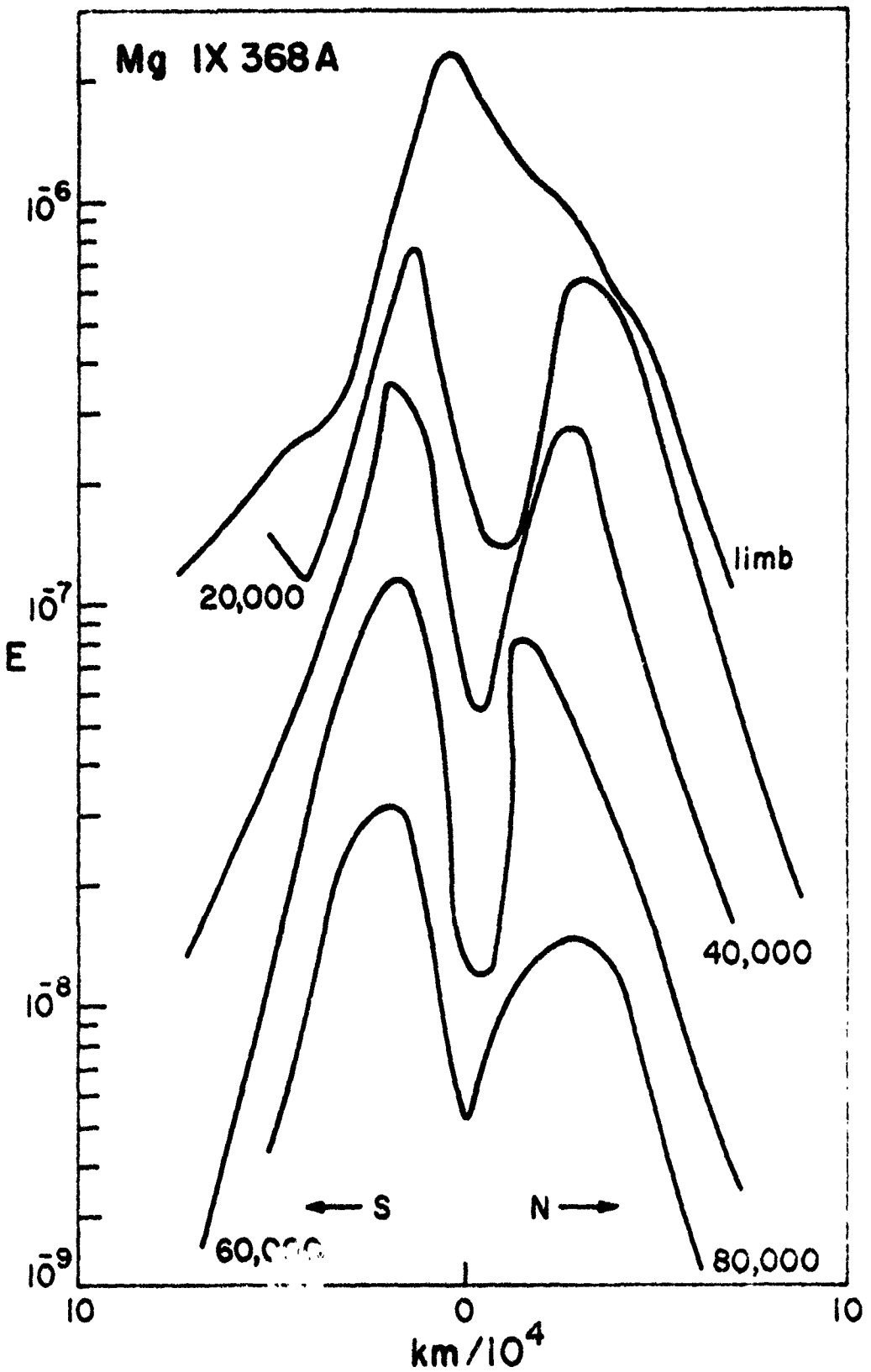
Mg IX 368A
10^{-6}
10^{-7}
10^{-8}
10^{-9}
E
20,000
limb
40,000
60,000
80,000
S
N
10
0
10
km/10^4

Figure [illegible]

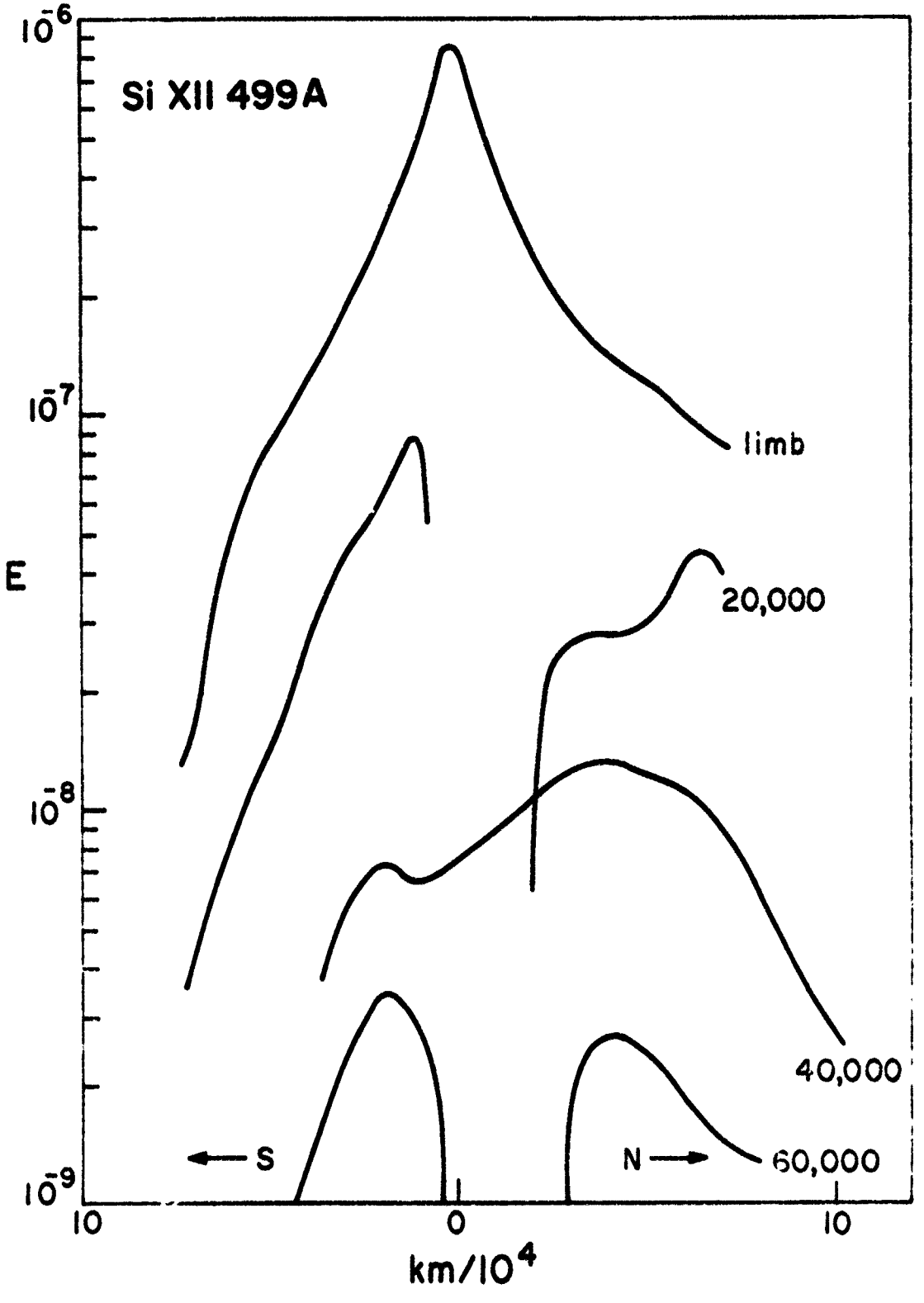

Figure VII-13

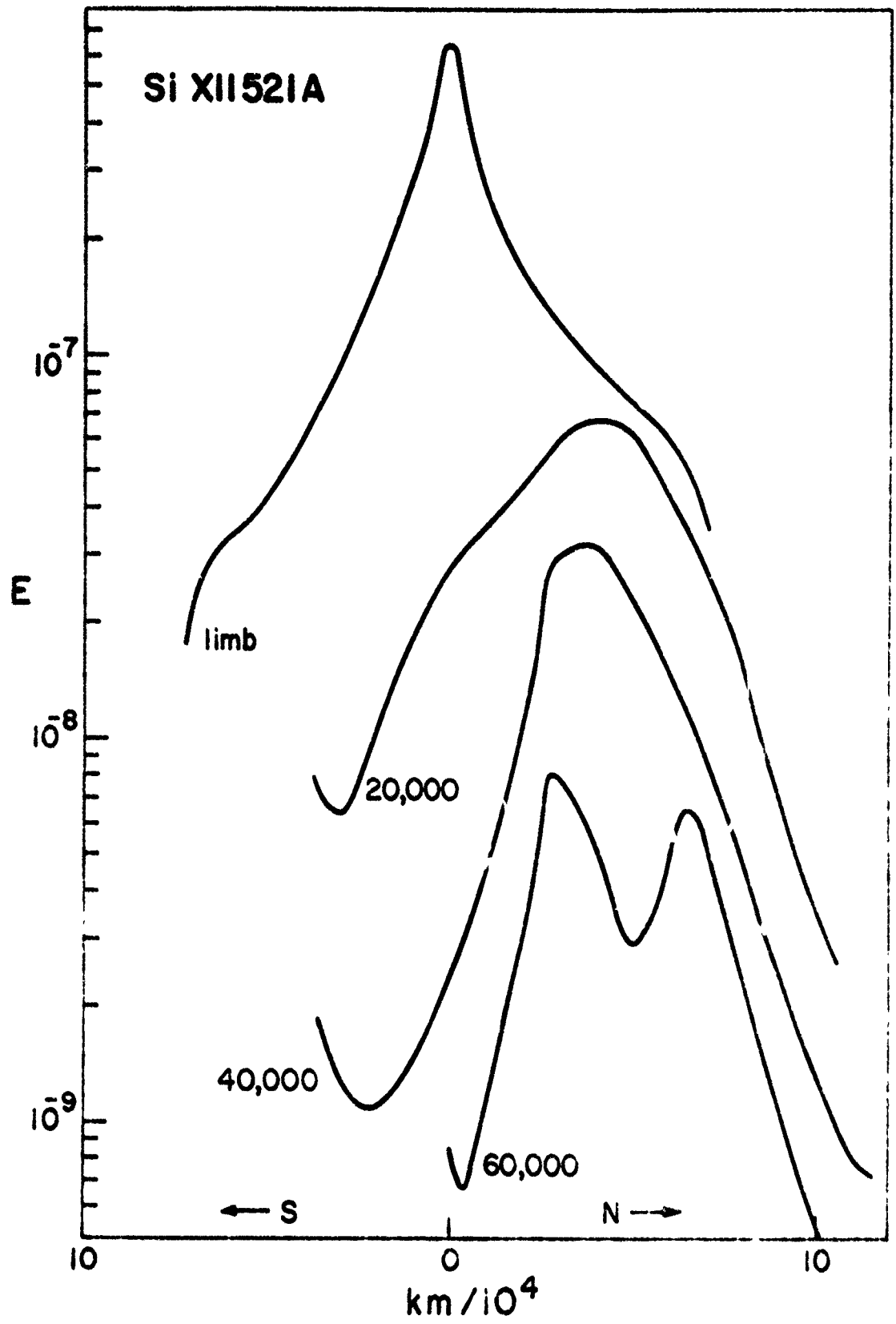
Si XII 521A
E
10^{-7}
10^{-8}
10^{-9}
limb
20,000
40,000
60,000
← S
N →
10
0
10
km / 10^4

Figure [illegible]

Figure VII-15. The temperature of Feature 4 as a function of position along the limb at several heights above the solar surface. The data are based upon Fe IX/ Fe XIV line emissivity ratios.

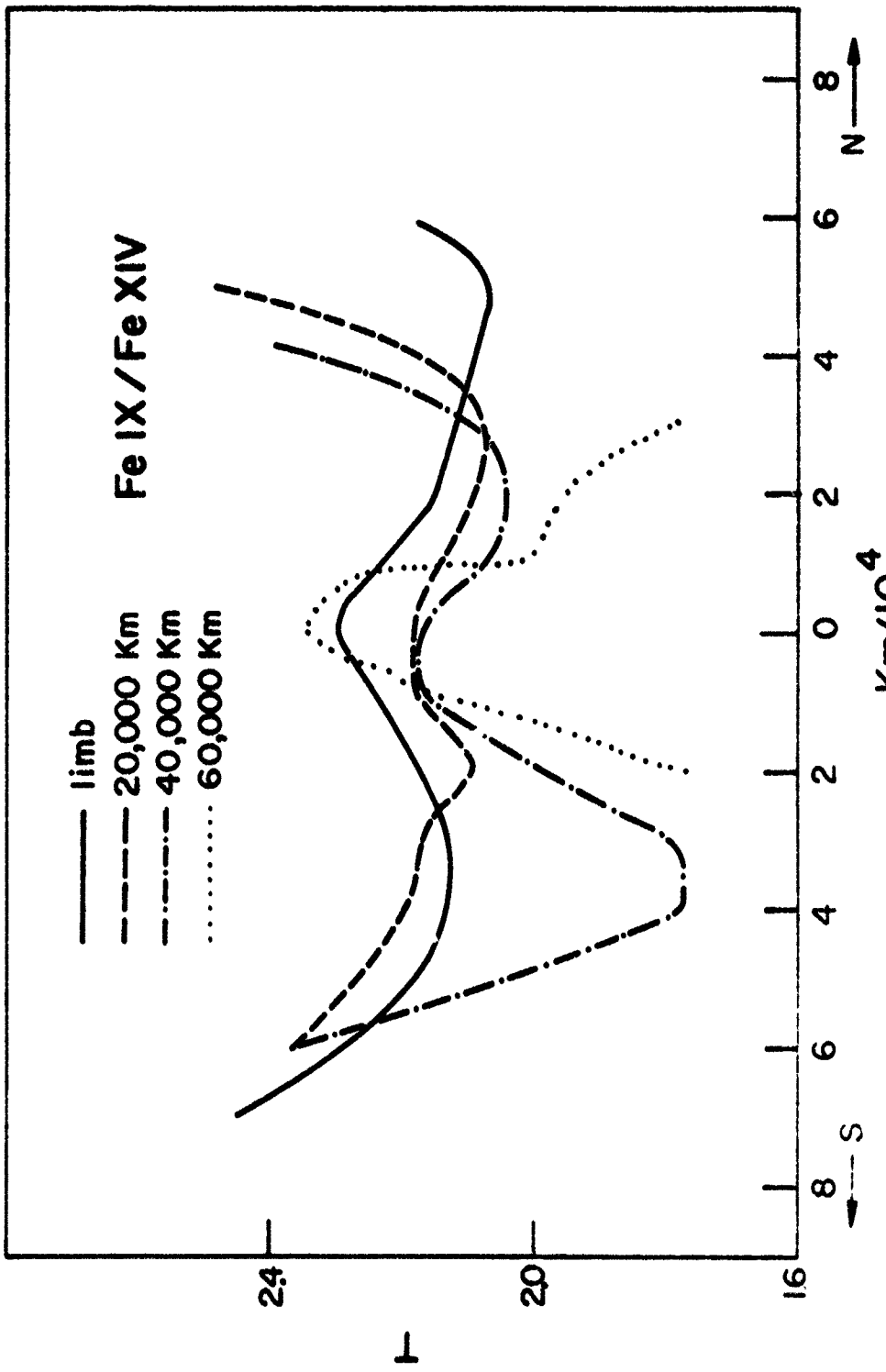

Figure VII-15

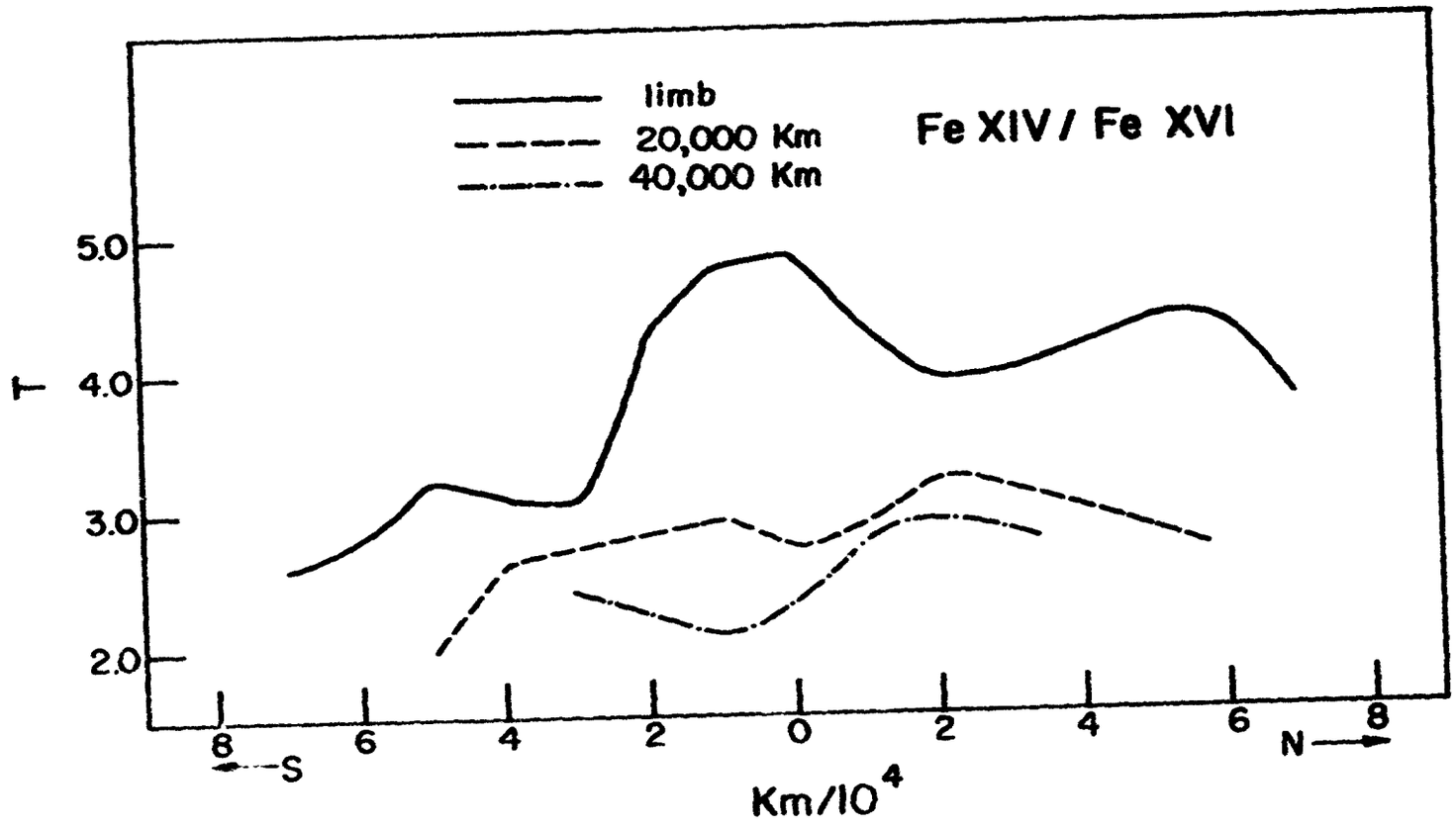

Figure VII-16. The same as VII-15, from Fe XIV/Fe XVI emissivity ratios.

Figure VII-17. The densities within Feature 4, based on the absolute emissivities and temperatures of the lines of Fe IX and Fe XIV.

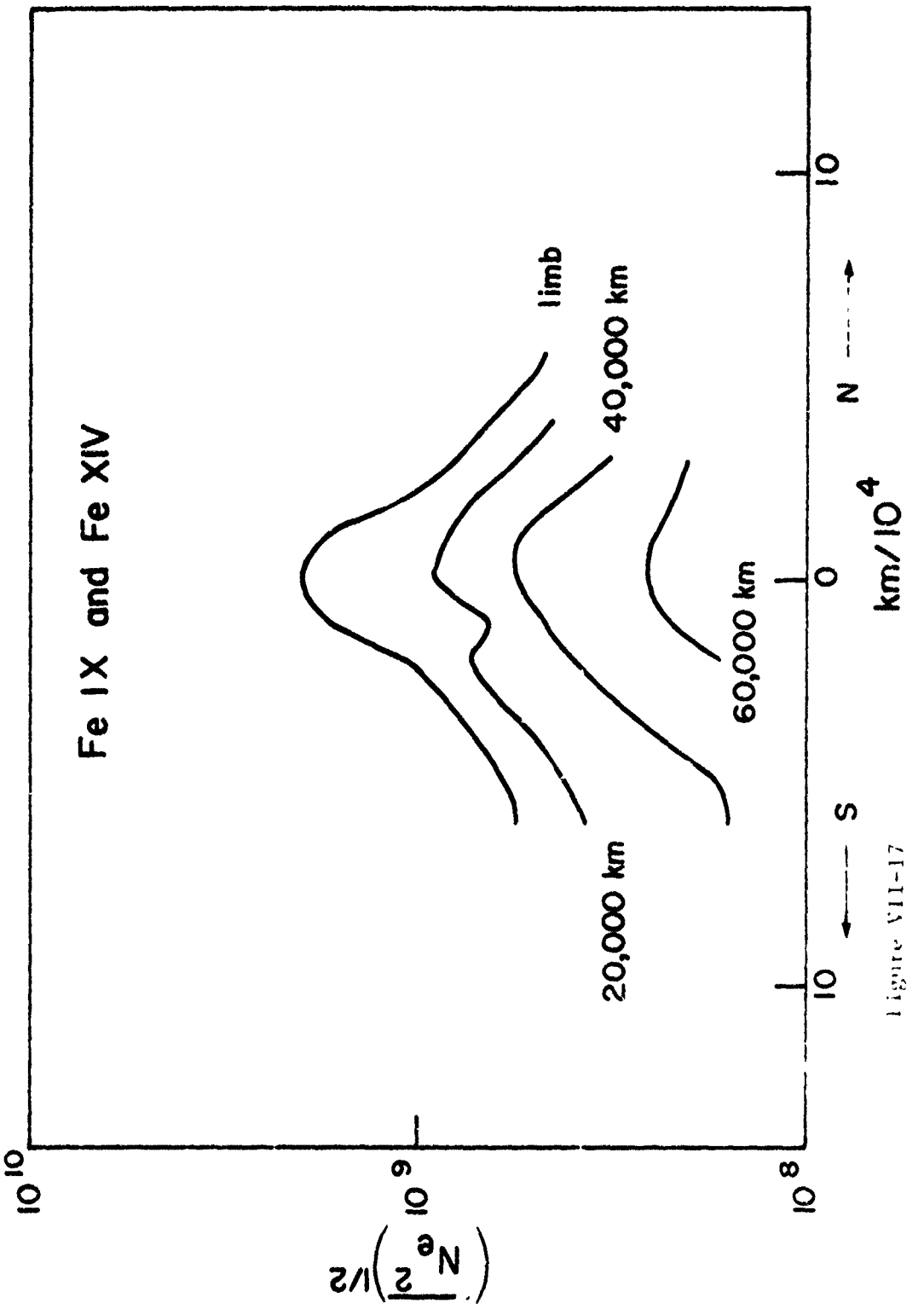

Figure VII-17

Figure VII-18. The same as VII-17, but with the lines of Fe XIV and Fe XVI.

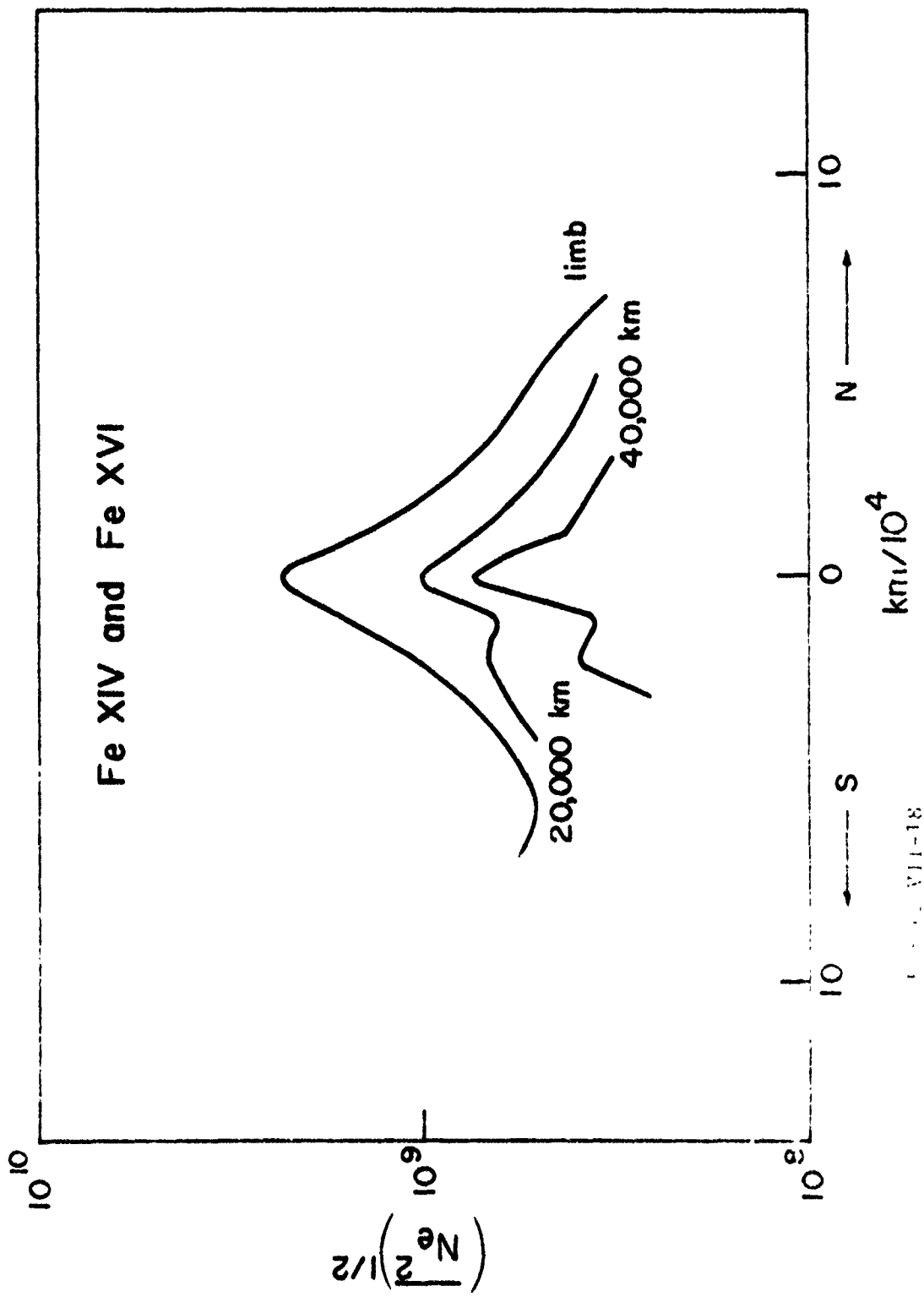
Fe XIV and Fe XVI
limb
40,000 km
20,000 km
10^{10}
10^{9}
10^{8}
$(\overline{N_e^2})^{1/2}$
10
S
0
N
10
km/10^4

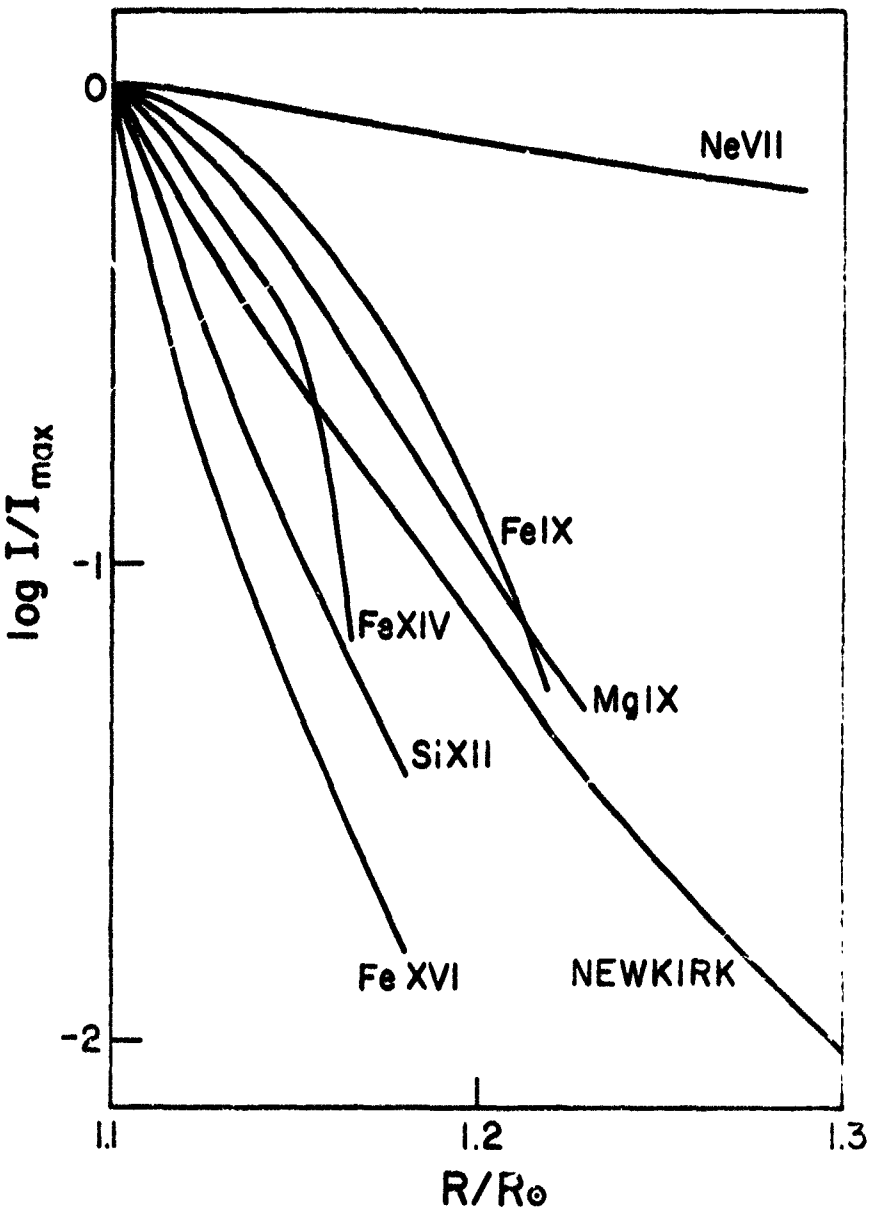

Figure VII-[illegible]. Brightness variations of feature 4 with [illegible] distance from the limb in solar radii. The curve labeled Newkirk's (1961) density model is given for comparison. All curves are normalized to equal Newkirk's at the limb.

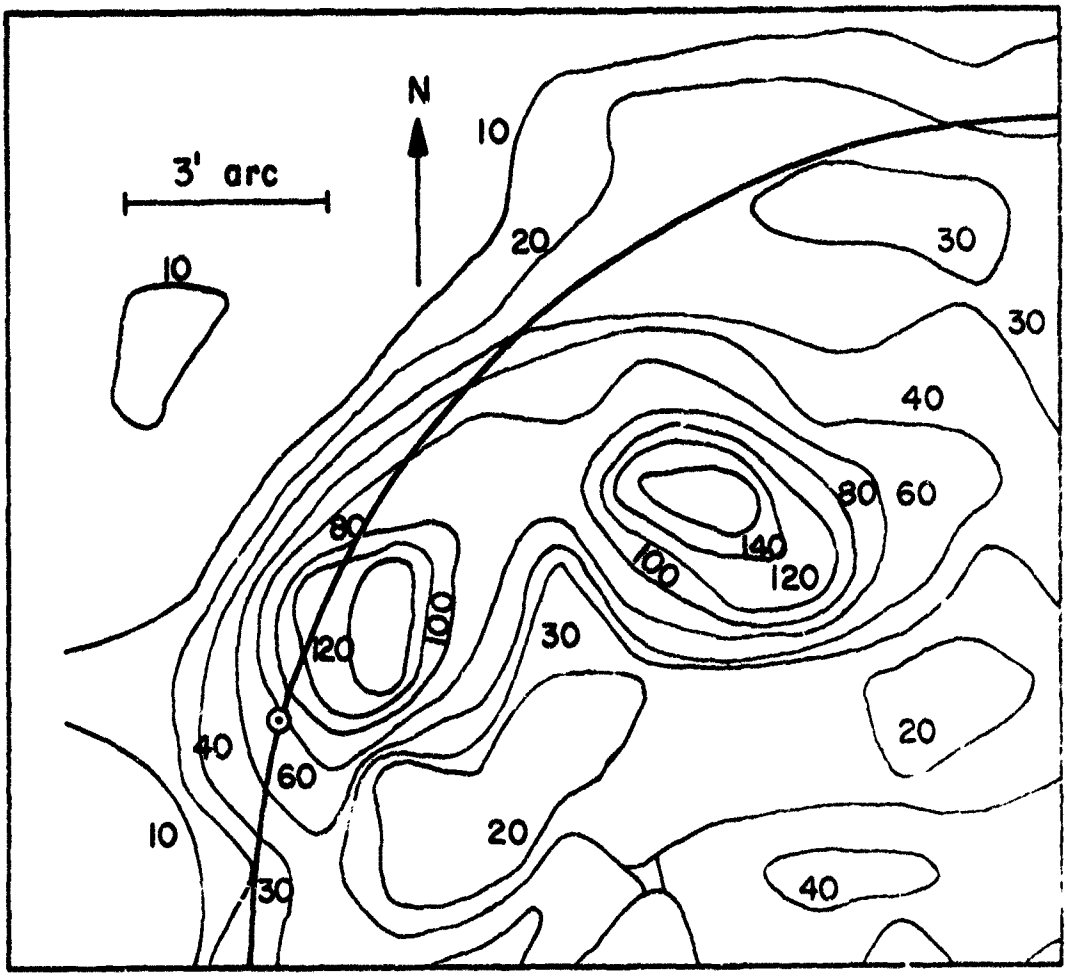

Figure VII-20. A radio brightness temperature map of a portion of the east limb of the sun on April 28, 1966. The map is drawn from Stanford 1.1 cm data. The position of Feature 4 is marked by a dotted circle.

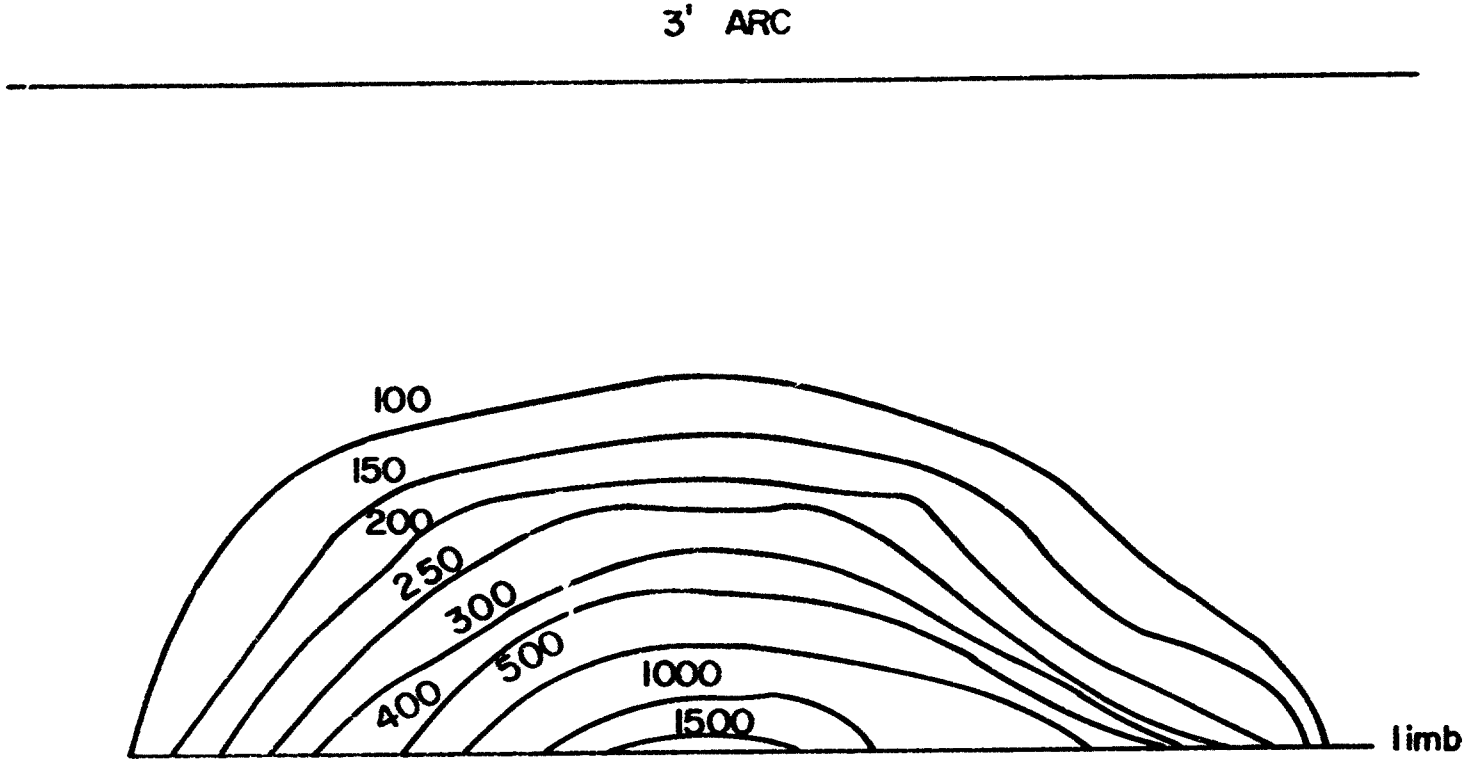

Figure VII-21. Isophotal contours of the predicted radio brightness temperatures in units of 1000 °K, of Feature 4. Predictions are based on the model obtained by photometric brightness measurements of the EUV lines.

Figure VII-22. The values of the integrated electron density, $\int N_e^2 dx$, and root-mean-square electron density, $\int (\overline{N_e^2})^{\frac{1}{2}} dx$, along the line of sight.

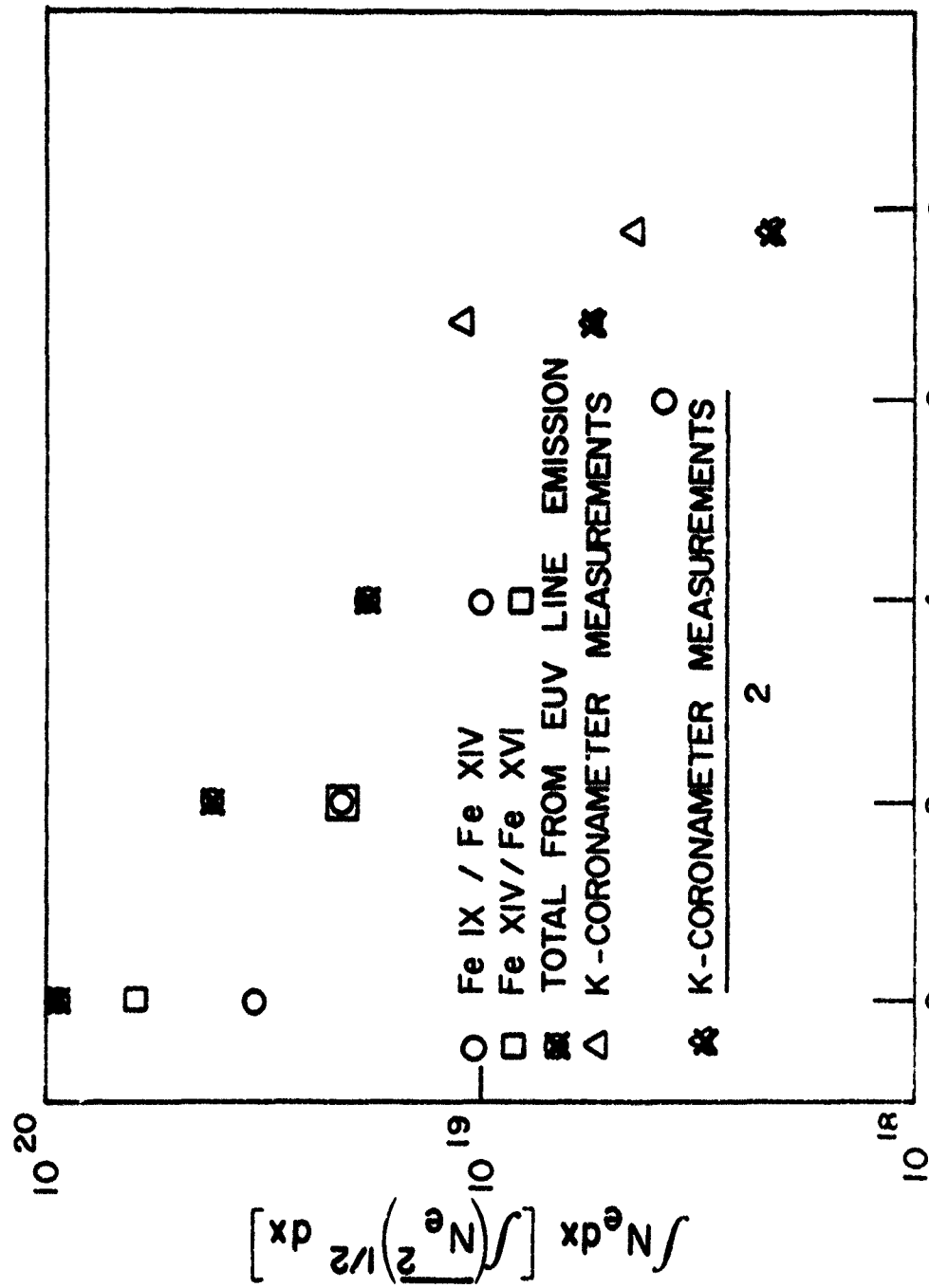

Figure VII-22

Figures VII-23 to VII-26.

Representation of the slope of the magnetic field within Feature 4, as inferred from the emissivity distributions of Mg IX, Fe IX, Fe XIV, and Fe XVI.

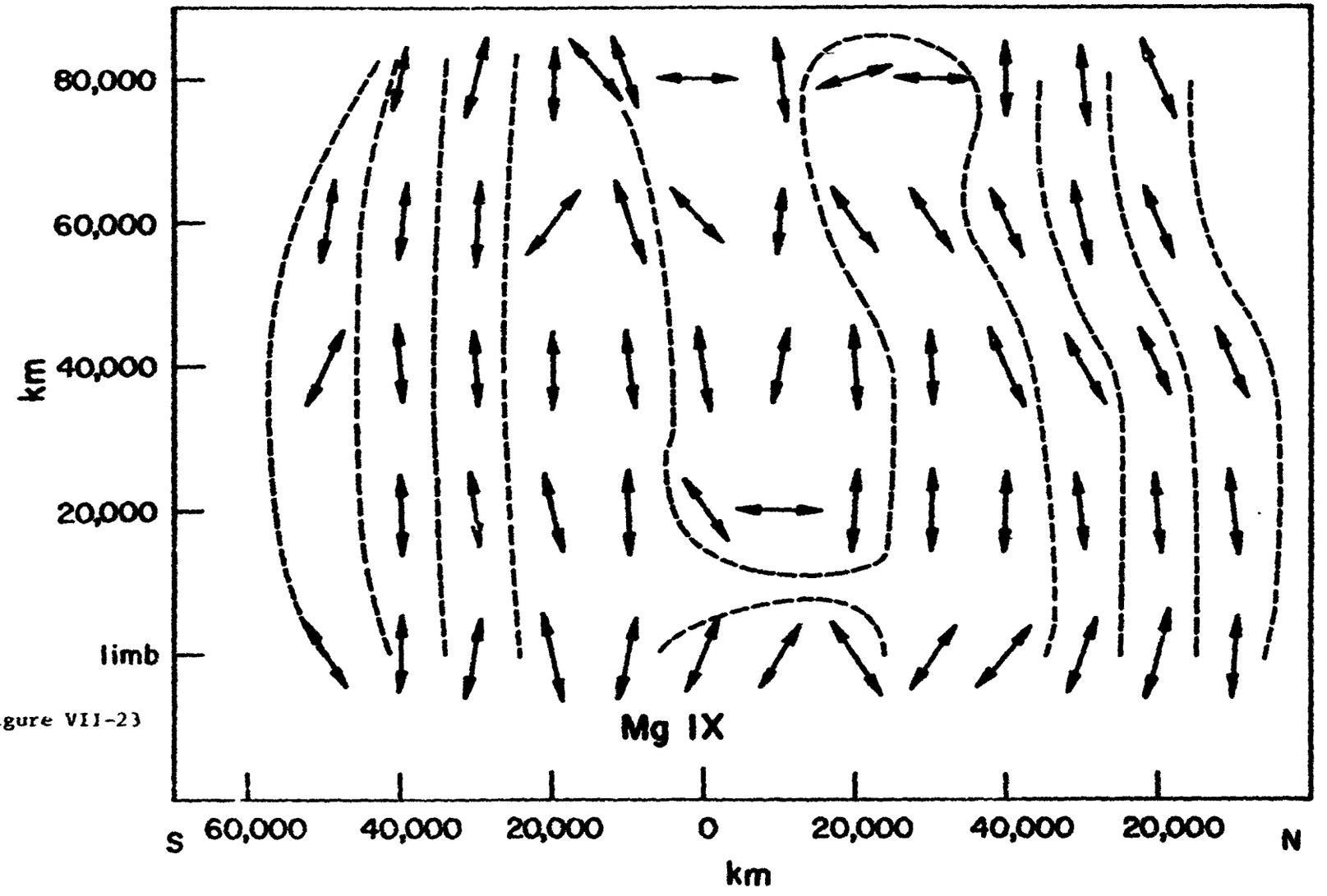

Figure VII-23

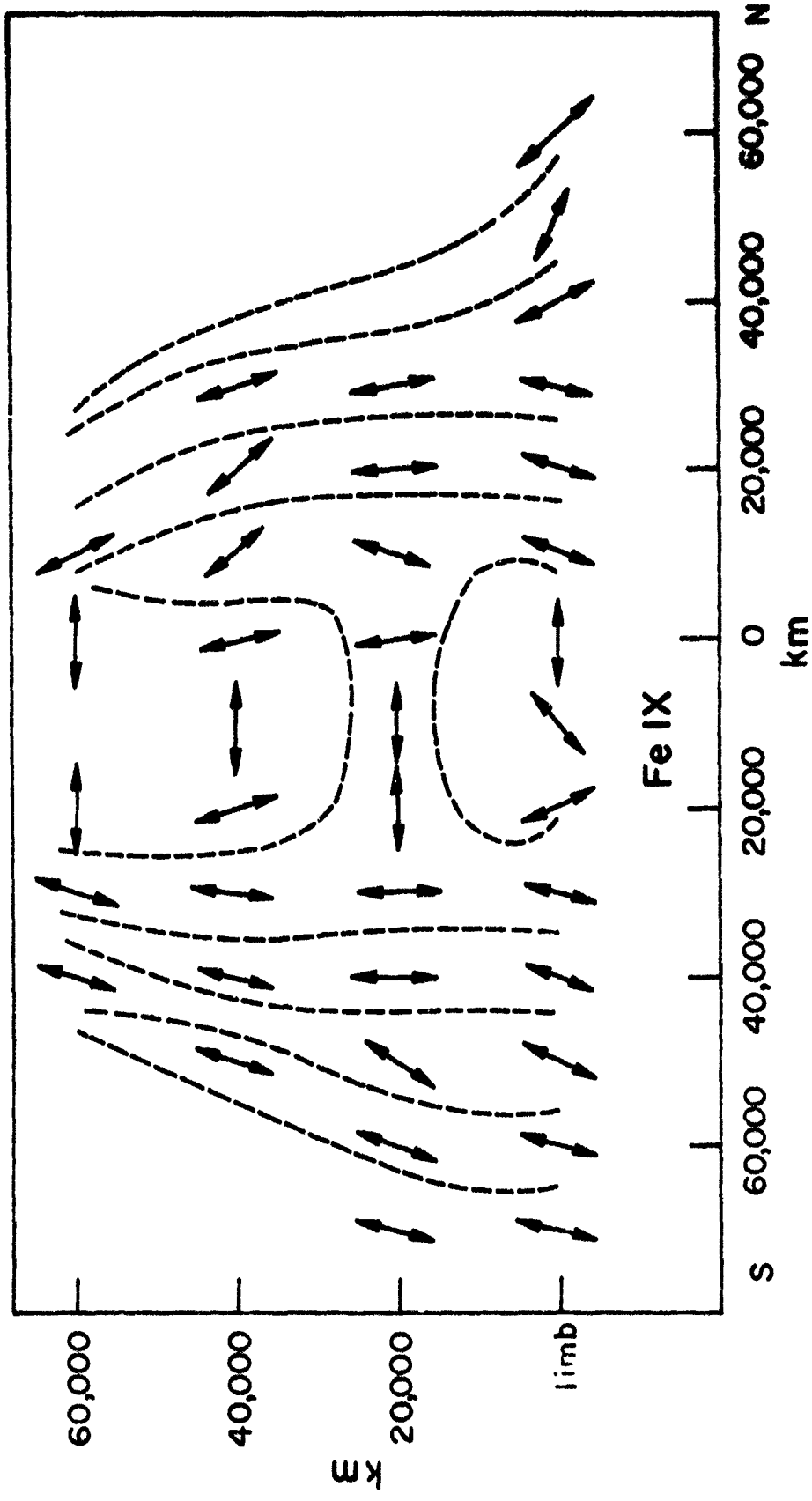

Figure VII-24

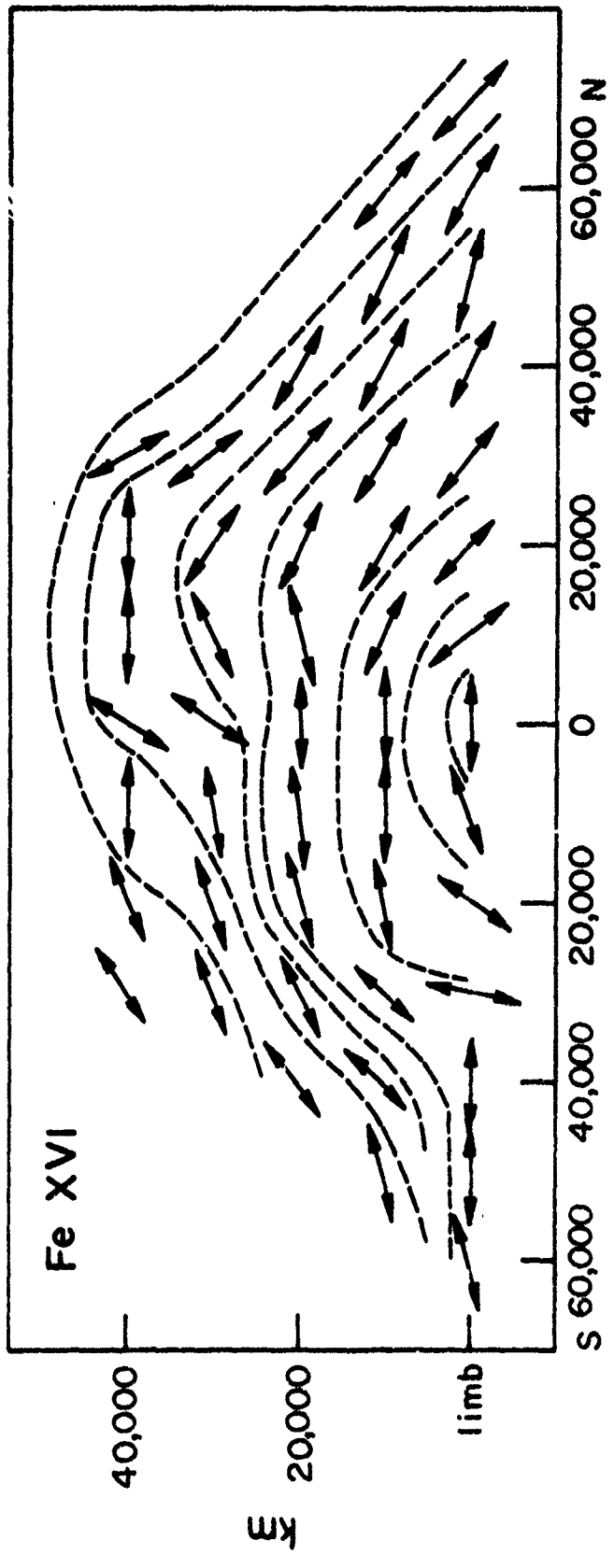

Figure VII-26

CHAPTER VIII

DISCUSSION

A. Summary of Results

In an effort to enhance the readability of this thesis, perhaps at the expense of compromising the objectivity of the presentation, I have both anticipated, and stated or implied various conclusions throughout the text. Most of the remarks in this section will therefore serve mainly to summarize the more important conclusions, and may be found also in earlier chapters.

Perhaps the most gratifying result of this investigation is that no glaring discrepancies between observations of the solar corona in the EUV and by other methods were found. The association of enhancements of the hard radiation of the sun with increased activity has long been known, so the association of EUV enhancements with plage regions is not at all surprising. The same association is predictable on theoretical grounds from the fact that coronal forbidden-line emission shows enhancement when active regions are on the limb.

In going beyond the obviously good superficial agreement of the coronal enhancements with chromospheric plages, we note that the lines of lower excitation such as O V tend to show plage-type structure similar to that of Ca-K. The oxygen line correspon-

to temperatures of between 1 and 2 x 10^5 °K, and therefore may be thought of as belonging to the lower part of the transition region between the chromosphere and the corona. The morphology of an active region in this temperature range is thus expected to be strongly influenced by the chromosphere, and indeed the chromospheric network appears to be still faintly visible. Ne VII represents an ion whose temperature (5 x 10^5 °K) lies pretty much in the middle of the transition region. The highly structured plages are now giving way to larger, less structured enhancements, although a sharp limb indicates that the radiation is still fairly low in the solar atmosphere. At temperatures of between 1 and 2 x 10^6 °K the emission is becoming more diffuse in the active regions, and at the same time less obvious on the solar disk as a whole. At the highest temperatures ($\gtrsim$ 2 x 10^6 °K), background emission becomes totally absent and we see essentially only the active regions of the corona.

The increasing concentration of coronal material in the active regions at higher temperatures shows up quantitatively in the analysis as a sharp increase in the amount of emitting material within the enhancement as one goes up in temperature, up to an abrupt drop at a temperature of about 5 million degrees (Chapter VII).

The more detailed analysis carried out in Chapter VII indicates a tendency for the hot material to confine itself to a dense core, fairly low in the enhancement. The existence of such localized high-temperature regions in a highly conducting medium can only be explained by the confining action of magnetic forces. The abrupt temperature rise is noticeable in the relative increase in brightness

of emission of the ion Fe XVI relative to Fe XIV, but is less apparent when one compares the ratio of emission of Fe IX and Fe XIV. The temperature and density structures of the enhancement at the limb predict radio and K-coronameter enhancements consistent in magnitude with those observed on the same day as the spectroheliograms were taken (April 28, 1966).

The fact that the observational inaccuracies were just great enough to frustrate any attempt to resolve the question of coronal abundances is disappointing. Fortunately, however, the major conclusions concerning the temperature and density structure are not sensitive to this uncertainty.

B. Future Work

The future course of solar EUV and X-ray astronomy is likely to be a very interesting one. Perhaps the most accurate estimate of the nature of the future development of this field would result from a consideration of the questions the present data did not answer.

A first look at the spectroheliograms suggests a significant difficulty in disentangling overlapping images, and in distinguishing a continuum from the line emission from the disk. As a result, only a few of the strongest lines were intense enough to yield meaningful photometric intensities. An increase in the dispersion relative to the image size would have the effect of reducing the continuum relative to the line intensities recorded on the film, as well as reducing the overlapping of the images themselves. An effect that

would partially negate the advantage gained would be a decrease in the resolution from the increasingly evident thermal Doppler broadening. The present spectroheliograms show resolution down to about 10" of arc which equals on the film the distance corresponding to 0.22A. This is nearly equal to the half-width of a 700A line arising from an ion of mass number 16 at a temperature of 4 million degrees. Since these conditions outlined represent a rather extreme set of circumstances, it would appear that the dispersion of the present setup could be increased by a factor of five or more without a noticeable increase in Doppler blurring.

All the above refinements will undoubtedly be realized in the near future. An NRL experiment in the Apollo Telescope Mount (ATM) project should provide spectroheliograms of better purity and resolution. Although the chromospheric network is evident in the images of He I, He II, and to a lesser extent O IV, no fine structure of the coronal features similar to that observed at eclipse in white light is as yet visible in the EUV.

An ubiquitous problem in astrophysics is the need for more accurate atomic transition rate coefficients of all types. In particular our knowledge of the rate coefficients for excitation of forbidden levels by electron impact can only be described as unsatisfactory at present. In addition many of the hotter ions depart appreciably from L-S coupling, and a thorough recomputation of f-values taking into account intermediate coupling and configuration interaction will be necessary before solar extreme ultraviolet

spectroscopy can advance beyond a semi-quantitative stage. Our knowledge is slowly but steadily increasing in this area both from experimental and theoretical studies currently being undertaken at the Joint Institute for Laboratory Astrophysics (JILA) in Boulder, Colorado.

Finally, the exciting possibility exists that future observations of the high energy radiation from the corona may in turn contribute to our knowledge of the atomic transition parameters as our knowledge of the detailed structure of the corona improves. There is no a priori reason why astronomical observations cannot aid in the development of physics just as physics has aided astronomy. The reason that they have not to such a large extent as might be hoped is simply that a controlled experiment has only recently been possible in astronomy. Continued exploration of the corona by satellites and space probes or by a permanent observing station will certainly not only increase our knowledge of the active sun, but also use the outer sun as a valuable laboratory to study detailed properties of highly stripped ions.

REFERENCES

Allen, C. W. Astrophysical Quantities. London: Athlone Press, 1963.

Allen, J. W. and Dupree, A. K. "Calculation of Ionization Equilibria for Oxygen, Neon, Silicon, and Iron" Scientific Report 24 Harvard College Observatory, Cambridge, Massachusetts Nov. 19 7

Astoin, N., and Vodar, B. "Thin Transparent Films in the Far Ultraviolet," J. Phys. Radium, 14, 424, 1953 (NRL translation #719).

Athay, R. G. "Theoretical Line Intensities V. Solar UV Emission Lines of Heavy Elements," Ap. J. 145, 784, 1966.

Athay, R. G., and Hyder, C. L. "Coronal Ionization by Two-Step Collision Processes," Ap. J. 137, 21, 1963.

Austin, W. E., Purcell, J. D., Tousey, R., and Widing, K. G. "Coronal Emission-Line Intensities in the Extreme Ultraviolet," Ap. J. 145, 373, 1966.

Bates, D. R., and Dalgarno, A. Atomic and Molecular Processes, ed. D. R. Bates. London: Academic Press, 1962.

Baum, W. A., Johnson, F. S., Oberly, J. J., Rockwood, C. C., Strain, C. V., and Tousey, R. "Solar Ultraviolet Spectrum to 88 Kilometers," Phys. Rev. 70, 781, 1946.

Bely, O. "Calcul des Sections de Choc dans les Ions de la Serie Isoelectronique du Lithium," Ann. d'Ap. 29, 131, 1966a.

Bely, O. "Excitation of Lithium-Like Ions by Electron Impacts II. Transitions 2s → ns and 2s → nd," Ann. d'Ap. 29, 683, 1966b.

Biermann, L. "Ueber den Mechanismus der Ionisation in der Sonnenkorona," Naturwissenschaften 34, 87, 1947.

Billings, D. E. A Guide to the Solar Corona. New York: Academic Press, 1966.

Billings, D. E. and Hatt, W. A. "Temperature of the Inner Corona with the Sunspot Cycle", Ap. J. 151, 743, 1968.

Blake, R. L., Chubb, T. A., Friedman, H., and Unzicker, A. E. "Measurement of Solar X-Ray Spectrum between 13 and 26A," Ann. d'Ap. 28, 583, 1965.

Bockasten, K. "Transformation of Observed Radiances into Radial Distribution of the Emission of a Plasma," J. Opt. Soc. Am. 57, 943, 1961.

Burgess, A. "Note on the Calculation of Coronal Ionization Cross-Sections," Ap. J. 132, 503, 1960.

Burgess, A. "Dielectronic Recombination and the Temperature of the Solar Corona," Ap. J. 139, 776, 1964.

Burgess, A. "Dielectronic Recombination in the Corona," Ann. d'Ap. 4, 774, 1965a.

Burgess, A. "A General Formula for the Estimation of Dielectronic Recombination Coefficients in Low-Density Plasmas," Ap. J. 141, 1588, 1965b.

Burgess, A. "Dielectronic Recombination," Smithsonian Ap. Obs. Special Report 174, 47, 1965c.

Burgess, A., and Seaton, M. J. "The Ionization Equilibrium for Iron in the Solar Corona," M. N. 127, 355, 1964.

Dupree, A. K., and Goldberg, L. "Solar Abundance Determinations from UV Emission Lines," Solar Phys. 1, 229, 1967.

Elton, R. C., Kolb, A. C., Austin, W. E., Tousey, R., and Widing, K. G. "Origin of Certain Solar Emission Lines between 170 and 220A," Ap. J. 140, 390, 1964.

Elwert, G. "Ueber die Ionisations- und Rekombinationsprozesse in einem Plasma und die Ionisationsformel der Sonnenkorona," Zs. f. Naturforsch. 7a, 432, 1952.

Fawcett, B. C., and Gabriel, A. H. "New Spectra of the Iron Transition Elements of Astrophysical Interest," Ap. J. 141, 345, 1965.

Fawcett, B. C., and Gabriel, A. H. "Spectra from $3p^n \rightarrow 3p^{n-1}3d$ Transitions of the Iron Period Elements in the Chlorine I and Sulfur I Iso-Electronic Sequences," Proc. Phys. Soc. 88, 262, 1966.

Fawcett, B. C., Gabriel, A. H., Griffin, W. G., Jones, B. B., and Wilson, R. "Observations of the Zeta Spectrum in the Wave-Length Range 16A-400A," Nature 200, 1303, 1963.

Fawcett, B. C., Gabriel, A. H., and Saunders, P. A. H. "New Spectra of Iron XII to Iron XVIII and their Isoelectronic Sequences," Proc. Phys. Soc., 90 863, 1967.

Gabriel, A. H., Fawcett, B. C., and Jordan, C. "Classification of Iron Lines in the Spectrum of the Sun and Zeta in the Range 167A to 220A." Nature 206, 390, 1965.

Gabriel, A. H., Fawcett, B. C., and Jordan, C. "Fe VIII to XII and XIV Lines in Solar Extreme Ultra-Violet Spectrum and Their Isoelectronic Sequences from Argon to Nickel," Proc. Phys. Soc. 87, 825, 1966.

Goldberg, L. "Ultraviolet and X-Rays from the Sun," Annual Review of Astronomy and Astrophysics ed. L. Goldberg, D. Layzer, and J. G. Phillips 5, 279, 1967.

Goldberg, L., Dupree, A. K., and Allen, J. W. "Collisional Excitation of Autoionizing Levels," Ann. d'Ap. 28, 589, 1965.

Goldberg, L., Müller, E. A., and Aller, L. H. "The Abundances of the Elements in the Solar Atmosphere," Ap. J. Suppl. 1, #45, 1960.

Hall, L. A., Damon, K. R. and Hinteregger, H. E. "Solar EUV Photon Flux Measurements in the Upper Atmosphere of August, 1961," Space Research 3, 745, 1963.

Hall, L. A., Schweizer, W., Heroux, L., and Hinteregger, H. E. "Solar XUV Spectrum of March, 1964," Ap. J. 142, 13, 1965.

Hall, L. A., Schweizer, W., and Hinteregger, H. E. "Long Term Variations of Solar EUV Fluxes," J. G. R. 70, 2241, 1965.

Hansen, Richard T. Private Communication, 1967.

Hinteregger, H. E. "Preliminary Data on Solar EUV Radiation in the Upper Atmosphere," J. G. R. 66, 2367, 1961.

Hinteregger, H. E., Hall, L. A. and Schweizer, W. "Solar XUV Spectrum from 310A to 55A," Ap. J. 140, 319, 1964.

House, L. L. "Ionization Equilibrium of the Elements from H to Fe," Ap. J. Suppl. 8, #81, 1964.

House, L. L. "Some Intermediate Coupling Transition Probabilities in Ca XV and Fe XIII," Ap. J. 149, 211, 1967.

House, L. L., Deutschman, W. A., and Sawyer, G. A. "Comparison of Solar and Laboratory Iron Spectra in the Vacuum Ultraviolet," Ap. J. 140, 814, 1964.

Ivanov-Kholodnyi, G. S., and Nikolskii, G. M. "Ultraviolet Solar Radiation and the Transition Layer between the Chromosphere and the Corona," Soviet Astron. A. J. 5, 31, 1961.

Ivanov-Kholodnyi, G. S., and Nikolskii, G. M. "A Prediction of Solar Line Emission in the EUV," Soviet Astron. A. J. 5, 632, 1962.

Jordan, C. "The Abundance of Iron in the Solar Corona," M. N. 132, 515, 1966.

Jordan, C. Communication to D. E. Billings, 1967.

Kononov, E. Ya. "Spectra of Multiply Ionized Sulfur Atoms S IX and S X in the Region 175-265A," Fizicheskii Institut im. P. N. Lebedeva, Akademiya Nauk USSR; Laboratoriya Spektroskopii (A-140). Moscow: 1965.

Kozlovsky, B.-Z. and Zirin, H. "The O VI Emission from the Sun," Submitted to Solar Physics, 1968.

Massey, H. S. W., and Bates, D. R. "The Properties of Neutral and Ionized Atomic Oxygen and their Influence on the Upper Atmosphere," Rep. Prog. Phys. 9, 62, 1942.

Menzel, D. H., and Peckeris, C. L. "Absorption Coefficients and Hydrogen Line Intensities," M. N. 96, 77, 1935.

Miyamoto, S. "Ionization Theory of the Solar Corona," Publ. Astr. Soc. Japan 1, 10, 1949.

Moore, C. E. Atomic Energy Levels. Washington: U. S. Government Printing Office, 1949.

Neupert, W. M "Emission of EUV Radiation from Solar Centers of Activity," Space Research 4, 730, 1964.

Neupert, W. M. "Time Variations in the Solar EUV Spectrum Observed by OSO-1," NASA report SP-50, 1964.

Neupert, W. M. "Intensity Variations in the Extreme UV Spectrum Observed by OSO-1," Ann. d'Ap. 28, 446, 1965.

Neupert, W. M. "The Solar Corona above Active Regions: A Comparison of Extreme Ultraviolet Line Emission with Radio Emission," Solar Physics 2, 294, 1967.

Neupert, W. M., Behring, W. E., and Lindsay, J. C. "The Solar Spectrum from 50A to 400A," Space Research 4, 719, 1964.

Newkirk, G. "The Solar Corona in Active Regions and the Thermal Origin of the Slowly Varying Component of Solar Radio Radiation," Ap. J. 133, 983, 1961.

Nishi, K. and Nakagomi, Y. "A Model of the Coronal Condensation," Pub. Astr. Soc. Japan 15, 56, 1963.

Pecker, C. "Ions of the Li I Sequence in the Solar UV Spectrum," Space Research 3, 809, 1963.

Pottasch, S. R. "The Lower Solar Corona: Interpretation of the UV Spectrum," Ap. J. 137, 945, 1963a.

Pottasch, S. R. "The Lower Solar Corona: The Abundance of Iron," M. N. 125, 543, 1963b.

Pottasch, S. R. "On the Interpretation of the Solar UV Emission Line Spectrum," Space Science Reviews 3, 816, 1964a.

Pottasch, S. R. "On the Chemical Composition of the Solar Corona," M. N. 128, 73, 1964b.

Pottasch, S. R. "On the Iron Lines Observed in the Solar Ultraviolet Spectrum," Bull. A. Inst. Neth. 18, 237, 1966a.

Pottasch, S. R. "On the Oxygen-to-Iron Ratio in the Solar Corona," Bull. A. Inst. Neth. 18, 443, 1966b.

Pottasch, S. R. "The Inclusion of Dielectronic Recombination Processes in the Interpretation of the Solar Ultraviolet Spectrum," Bull. A. Inst. Neth. 19, 113, 1967.

Purcell, J. D. Private Communication, 1967.

Purcell, J. D., Garrett, D. L., and Tousey, R. "Spectroheliograms in the Extreme Ultraviolet," A. J. 69, 147, 1964.

Purcell, J. D., Packer, D. M., and Tousey, R. "The UV Spectrum of the Sun," Space Research 1, 581, 1960.

Saito, K., and Billings, D. E. "Polarimetric Observations of a Coronal Condensation," Ap. J. 140, 760, 1964.

Schwartz, S. B. and Zirin, H. "Collisional Ionization Cross Sections for Fe XIV in the Solar Corona and the Coronal Electron Temperature," Ap. J. 130, 384, 1959.

Schwarzschild, K. "On the Deviations from the Law of Reciprocity for Bromide of Silver Gelatine," Ap. J. 11, 89, 1900.